Airborne Vector Gravimetry Using GPS/INS

by

Jay Hyoun Kwon

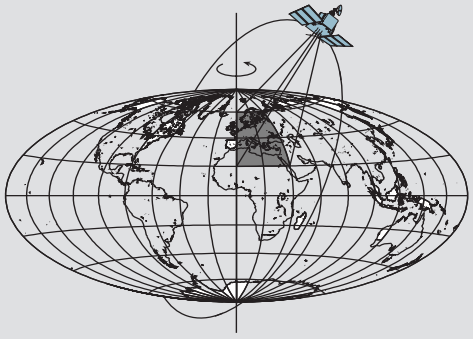

Report No. 453

Geodetic Science and Surveying
Department of Civil and Environmental Engineering and Geodetic Science
The Ohio State University
Columbus, Ohio 43210-1275

April 2000

AIRBORNE VECTOR GRAVIMETRY USING GPS/INS

by

Jay Hyoun Kwon

Geodetic Science and Surveying
Department of Civil and Environmental Engineering and Geodetic Science
The Ohio State University
Columbus, Ohio 43210-1275

April. 2000

Dedicated to my parents, wife and son

PREFACE

This report was prepared by Jay Hyoun Kwon, a graduate student, Department of Civil and Environmental Engineering and Geodetic Science, under the supervision of Professor Christopher Jekeli. This research was supported by the National Imagery and Mapping Agency (NIMA); Contract No. NMA202-98-1-1110.

It was submitted to the Graduate School of The Ohio State University in the Winter of 2000 in partial fulfillment of the requirements of the Doctor of Philosophy degree.

ABSTRACT

Compared to the conventional ground measurement of gravity, airborne gravimetry is relatively efficient and cost-effective. Especially, the combination of GPS and INS is known to show very good performances in the range of medium frequencies (1-100 km) for recovering the gravity signal.

Conventionally, gravity estimation using GPS/INS was analyzed through the estimation of INS system errors using GPS position and velocity updates. In this case, the complex navigation equations must be integrated to obtain the INS position, and the gravity field must be stochastically modeled as a part of the state vector. The vertical component of the gravity vector is not estimable in this case because of the instability of the vertical channel in the solution of the inertial navigation equations.

In this study, a new algorithm using acceleration updates instead of position/velocity updates has been developed. Because we are seeking the gravitational field, that is, accelerations, the new approach is conceptually simpler and more straightforward. In addition, it is computationally less expensive since the navigation equations do not have to be integrated. It is more objective, since the gravity disturbance field does not have to be explicitly modeled as state parameters.

An application to real test flight data as well as an intensive simulation study has been performed to test the validity of the new algorithm. The results from the real flight data show very good accuracy in determining the down component, with accuracy better than ±5 mGal. Also, a comparable result was obtained for the horizontal components with accuracy of ±6 to ±8 mGal. The resolution of the final result is about 10 km due to the attenuation with altitude.

The inclusion of a parametric gravity model into the new algorithm is also investigated for theoretical reasons. The gravity estimates from this filter showed strong dependencies on the model and required extensive computation with no improvement over the approach without parametric gravity model.

ACKNOWLEDGMENTS

Studying at the Department of Geodetic Science would not have been possible for me without invaluable support and help from many persons whom I would like to gratefully acknowledge.

First and foremost, I would like to express my sincere gratitude to my adviser, Dr. Christopher Jekeli for his invaluable guidance, encouragement, patience and insight throughout this research for many years. Working as a research associate under his guidance has been the most valuable experience in my years of education. I would like to extend my sincere thanks to other members of my advisory committee, Dr. C. K. Shum and Dr. Burkhard Schaffrin for their thoughtful comments and suggestions.

A special appreciation goes to Dr. Ivan Muller and Dr. Clyde Goad who have guided me to have concrete concepts in various fields of geodesy.

I would like to thank all faculty members, staff and students for their support and help. To share our knowledge and thoughts with my colleagues was always constructive. In this regard I would like to mention Dr. Yu-Chan Yi, Dr. Dong-Cheon Lee, Keehwan Hong, and Dr. Hong-Gyoo Sohn. Finally, and most important, I would like to express my deepest gratitude to my family. Love, encouragement, support, and patience from my wonderful parents, beloved wife Eun Ah and son Patrick have truly made my fulfillment of study possible. I always thank God for allowing me such a great family and guiding me all along.

TABLE OF CONTENTS

PAGE

LIST OF TABLES

LIST OF FIGURES

CHAPTER 1

INTRODUCTION

1.1 Background

The determination of the Earth's gravity field is one of the most important areas in geodesy for the determination of an Earth model (geoid) and for the prediction of dynamical parameters of low Earth-orbiting satellites. In addition, gravity information is important for many scientific and engineering areas such as geophysical exploration and navigation, and in studying geophysical phenomena of the Earth. Conventionally, the gravity signal is determined by measuring its magnitude with a gravimeter and determining the deflections of the vertical, defined by the difference of the directions between the natural gravity and normal gravity vector, by astronomical observations. Although this produces highly accurate gravity vector information, it is extremely expensive and time consuming.

Due to the recent satellite technology, it is possible to determine the gravity field using satellite observations mostly in the form of satellite altimetry, and a more refined global gravity model based on terrestrial gravity and satellite data is available, *e.g.*, EGM 96 (Lemoine *et al*., 1998). Hence the long wavelength gravity signal can be obtained by using a global model (Rapp and Pavlis, 1990; Jekeli, 1995). According to the recent study by Jekeli (1999), however, the shorter-wavelength signatures of the global model are either poorly modeled or only moderately well known in the global model resulting in under-powered at wavelengths shorter than 200 km. Therefore, the purpose of the airborne gravimetry is to recover the Earth's gravity field on the medium-frequency gravity signal, which then fills the gap between the terrestrial gravity field measurements and global gravity models in the wavelengths between 1 and 100-200 kilometer (Hein, 1995).

By the middle of this decade, measurements from GRACE (Tapley et al., 1997), CHAMP (Reigber et al., 1997) and GOCE (Rummel, 1999) gravity mapping missions are expected to provide revolutionary improvement in our knowledge of the Earth's static gravity field and its temporal component. Especially, the accuracy of the mean geoid will be about 1 cm at a wavelength of 100 km or longer (primarily by GOCE). The accuracy and resolution from these missions, however, are not still good enough for the geophysical exploration in which 1 mGal over less than 10 km is required (Salychev et al., 1994). In addition, there will be polar gaps with radius of 700 km due to the sun-synchronized orbits for GOCE. Therefore, even after these

missions, the airborne gravimetry will still play an important role in improving the model for the earth's gravity field.

As a matter of fact, the Inertial Navigation System (INS) was introduced as a surveying instrument in the late 1960's, and immediately it was noticed that the potential of INS for precise positioning was limited by the unknown anomalous gravity field (Nash, 1968; Huddle, 1977). Conversely, this means that the anomalous 3-D gravity field could be recovered from the INS if accurate kinematic positions and/or velocities were known and the system errors were kept small. Among early studies in vector gravimetry, Rose and Nash (1972) showed the ability of an INS to measure the deflection of vertical directly.

The important issue in gravity recovery using INS is the separation of the gravitational acceleration from kinematic acceleration as well as system errors. The kinematic acceleration can be separated from the sensed acceleration of INS by using a different sensor such as GPS. The separation between the gravitational acceleration and system errors from INS can be achieved by introducing external information *e.g.*, ZUPT (Zero Velocity Update, Torge, 1989). That is, bring the vehicle to a stop periodically, thus controlling the unknown systematic errors by feeding the zero velocity information back to the system. Although this semi-kinematic method had been successfully used in many cases (Huddle, 1988; Salychev *et al*., 1994; Wang and Gao, 1996), it is still inefficient and expensive for the exploration of large areas. In addition, it cannot be used in areas essentially inaccessible to land vehicles or helicopters such as seas, deserts, or mountains.

Obviously, an alternative way of determining the kinematic position and velocity was necessary to perform the mobile, especially airborne, gravity survey. In 1967, Moritz proposed the combination of INS and a gravity gradiometer, and simulation studies on such a combination showed promising results (Heller and Jordan, 1976). Because of the high cost of the gradiometers, however, other combinations such as the combination of INS with a radio navigation system, Loran-C (Lacoste *et al*., 1982), were investigated. The accuracy of the gravity field from the system was poor because of the low data rate and accuracy of the radar altimeter.

Clearly, the advent of the Global Positioning System (GPS), providing high accuracy position and velocity, created revolutionary progress in the area of the airborne gravimetry. Schwarz (1987) compared different kinematic methods for airborne gravimetry with combinations of GPS, INS, and gradiometer. He concluded that the GPS/INS combination showed good medium-wavelength performance, while the GPS/gradiometer combination was better for high-frequency components. Compared to the other positioning instruments, GPS is inexpensive and the accuracy of the vehicle acceleration from GPS is sufficient for airborne gravimetry.

There have been many studies on the feasibility of GPS/INS gravimetry in both time and spectral domains (Jekeli, 1995; Knickmeyer, 1990; Schwarz *et al*. 1994). This research has shown that the gravity disturbance can be recovered with errors in the order of (RMS) ±1-2 mGal using a high-accuracy INS (Jekeli, 1995) within a spectral window of 10-200 km (Schwarz *et al*., 1994).

The main obstacle in GPS/INS gravimetry is the low signal to noise ratio of the system. Typically, gravity disturbance vector does not exceed 100 mGal in each component over distance of about 100 km while the noise level of the system is much higher (Hammada, 1995). Analyses and simulations were conducted by many investigators mainly applying a low pass filter on the signal to reduce the system noises and extract the optimal gravity signatures in GPS/INS airborne gravimetry (Hehl, 1994; Wei and Schwarz, 1995). In addition, the development as well as the analysis of the INS error model has been investigated theoretically, and tested throughout simulations (Arshal, 1987; Goshen-Meskin and Bar-Itzhack, 1992; Wei and Schwarz, 1994). Recently, some test flights also have been carried out to determine the feasibility and to assess the accuracy in airborne gravimetry. It has been shown that 1 mGal accuracy in GPS acceleration and 2-3 mGal of accuracy in the vertical gravity component can be achieved (Wei and Schwarz, 1998).

1.2 Statement of the Problem

There are two main categories in airborne gravimetry based on measurements of accelerometer, namely scalar gravimetry and vector gravimetry. Gravity gradiometry may be considered as the third type (Hein, 1995), where observations are the gradient of gravity. Scalar gravimetry determines either the vertical component or the magnitude of the gravity anomaly vector while vector gravimetry aims to recover the full gravity anomaly vector in all three dimensions. Obviously, the advantage of the vector gravimetry compared to the scalar gravimetry is that the (relative) geoid can be determined directly by along-track integration of the horizontal gravity components. Thus, the numerical integration of the vertical gravity component over large region (Vening-Meinesz integrals; Heiskanen and Moritz, 1987) can be avoided.

Currently, airborne gravimetry is conducted using either sea/air gravimeters on a Schuler-tuned stabilized platform for scalar gravimetry, or with an Inertial Navigation System mainly strapdown INS for scalar or vector gravimetry. In both cases, the separation of the gravitational and kinematic accelerations from the system errors is very crucial in estimating the gravity field. Results of scalar airborne gravity survey using gravimeters, modified for high dynamics of the aircraft, in Greenland, Antarctica, and Switzerland show that an accuracy of 3 to 5 mGal and a resolution of 10 km wavelength is achievable with current technology (Brozena and Peters, 1994, 1995; Forsberg and Kenyon, 1994). The main error source in this case was insufficient platform stabilization. Another test using ITC-2 inertial platform system showed that an accuracy of 1 mGal with resolution of 2-3 km is achievable (Salychev et al., 1994).

Unlike to the stabilized systems, there is no physical stabilizing platform in strapdown system. Instead, the inertial sensors are physically bolted down to the vehicle so that the measured data in the body frame are transformed to the local level frame computationally. The advantage of the strapdown INS is its smaller size, lower cost and more operational flexibility (Jekeli, 1995a). It has been shown that the performance of the SINS is comparable to the airborne gravimeter (Glennie *et al.*,

1999).

The traditional way of analyzing the determination of gravity using the GPS/INS signal is to integrate the error dynamics equations of the INS system, and model the INS errors and gravity disturbance as stochastic processes (Grejner-Brzezinska and Wang, 1998; Jekeli, 1995, 1995b; Knickmeyer, 1990; Wang, 1997; Forsberg, 1987; Eissfeller and Spietz, 1989). The apriori stochastic information of the INS errors such as biases and scale factors are obtained from the manufacturer's specification.

There are good arguments for modeling the gravity disturbance field as a stochastic process – it is one of the basic tenets of least-squares collocation in geodesy (Moritz, 1980). In a sense, a stochastic model is introduced to regularize an otherwise ill-posed problem. However, in this case we must treat the gravity state as a variable of a finite-dimensional state-space (Jekeli, 1995), and furthermore, one that satisfies a linear differential equation (Jordan, 1972). Practically, however, it is one of the main proposed approaches in airborne gravimetry (Wang, 1997). In this method, GPS position or velocity is used as an update in a Kalman filter estimation and the calculation is done in the navigation frame.

Although there are some investigations about vector gravimetry using covariance analyses (Knickmeyer, 1990; Jekeli, 1995) and error analysis through simulation (Wei and Schwarz, 1994), actual implementations have not been widely achieved for the horizontal gravity components. Because the horizontal components are more sensitive to the orientation and dynamics of the vehicle, more accurate orientation information is necessary to achieve the same accuracy as for the vertical. A horizontal accuracy of 1 mGal corresponds to about 0.2 arcsec in orientation accuracy, and it has been claimed that an accuracy of about 1 arcsec can be achieved using current technology.

The objective of this research is to develop a new efficient algorithm for GPS/INS vector gravimetry. The main idea of this research is that the gravity disturbance can be obtained directly by differencing the GPS and INS sensed accelerations (Jekeli, 1992). This is analogous to conventional airborne scalar gravimetry using gravimeters (Brozena, 1991). One of the conceptual differences between the traditional and this approach concerns the different methods used to integrate INS and GPS data. While the traditional method uses complex error dynamics associated with the solution to the navigation equations, the new method has a very simple set of equations based on accelerations. In addition, the calculations in the new method are carried out in the inertial frame, not in the navigation frame, so many computations related to the integration of the error dynamics equations in the traditional method can be saved. Through intensive simulations as well as application to real test flight data, the validity and efficiency of the new algorithm are presented.

The gravity field is not specifically modeled as a stochastic process in this new approach. Instead, it will be treated as an observation model error that can be seen in the residuals after estimating the INS system error parameters. In other words, it is assumed that no information is available on the gravity disturbance, even its existence,

so that it cannot be modeled. If a mathematical model is incorrect in an adjustment problem, the effect should be seen in the residual after the adjustment. Although this intentional mismodeling has its theoretical drawbacks, it has turned out to be very useful for the airborne gravimetry. However, proper interpretations and limitations must be considered and will be discussed.

1.3 Chapter Descriptions

The mathematical background including the descriptions of various coordinate systems, transformations among the systems, and the definitions of the related quantities are presented in Chapter 2.

In Chapter 3, an overview of both GPS and INS systems is described. The system description, observables, related errors, and principles of kinematic positioning are addressed for GPS. System mechanizations, measurement methods, error models for both accelerometers and gyros, and navigation equation are reviewed for INS.

The traditional approach for estimating the gravity components using position or velocity update routine is presented in Chapter 4. The details on the error dynamics, stochastic modeling for systematic errors, gravity modeling and Kalman filtering are discussed in this chapter. The results and analysis of the application to real data using the traditional methods are also presented for comparison.

The full development from the mathematical model to the data processing procedure for the new algorithm is presented in Chapter 5. Details on error parameters and some aspects on the smoothing are also discussed. The validity test and the investigations on the error behaviors are described through simulation. The results, analysis and the full descriptions of comparison between the traditional and new approach are given in terms of the mathematical model, the error parameters, their estimability and the efficiency of the algorithm.

In Chapter 6, cooperation of a gravity model in the mathematical model to the new algorithm is discussed. Using a Gauss-Markov model and an expansion of trigonometric functions, the feasibility as well as the validity of the approach is presented. Advantages and disadvantages of the gravity modeling are also addressed.

A brief discussion of all results, future studies, conclusions and suggestions are presented in Chapter 7.

CHAPTER 2

COORDINATE FRAMES AND TRANSFORMATION

2.1 Introduction

To describe locations of points on or near Earth's surface, a coordinate system should be defined. Although one could describe the whereabouts of objects and places using a relational or synthetic database, it is necessary to assign an algebraic coordinate system if one wants to know more than the location information such as the measure of distance, area, volume and direction (Jekeli, 1995a). In navigation, it is also necessary to measure the progress and determine the course and destination of a vehicle based on the selected coordinate system.

It should be noted that the term coordinate system and coordinate frame do not have the same meaning. The coordinate system includes the description of the physical theories and their approximations that are used to define the coordinate axes, while frame denotes the accessible realization of the system through a set of points whose coordinates are monumented or otherwise observable (Jekeli, 1995a; Moritz and Mueller, 1988).

The most common system in use is the Cartesian coordinate system whose axes are mutually orthogonal. To define a Cartesian coordinate system, three elements such as origin, orientation and scale factors should be determined. Figure 2.1 shows a right-handed Cartesian coordinate system.

It is constructed in such a way that right angle rotation about the 1 axis, viewed toward the origin, rotates the 2 axis into the 3 axis. Similarly, rotation about the 2 axis rotates the 3 axis into the 1 axis and that about the 3 axis rotates the 1 axis into the 2 axis. An arbitrary vector in the Cartesian coordinate system can be decomposed into its component on each axis. Denoting the components with a subscribed letter, a vector $\mathbf{x}$ can be represented as an ordered triplet of coordinates:

$$\mathbf{x} = \begin{pmatrix} x_1 \\ x_2 \\ x_3 \end{pmatrix}. \tag{2.1}$$

It can be also written using unit vectors as:

$$\mathbf{x} = x_1\mathbf{e}_1 + x_2\mathbf{e}_2 + x_3\mathbf{e}_3 \tag{2.2}$$

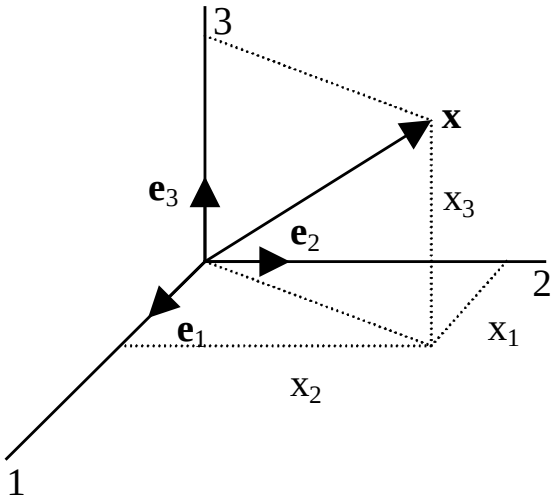

Figure 2.1 Cartesian coordinates of vector **x**, and unit vectors $\mathbf{e}_j$.

There are several coordinate frames in use in the field of geodesy. Those frames can be divided into global and local frames. While the global Cartesian coordinates are fixed either to the Earth or the celestial sphere, the local Cartesian coordinates are defined by local directions; for example north, east and down. The curvilinear frame, defined by the geodetic latitude, longitude and height, is also used for its appropriateness of representing the motion and position on the sphere or ellipsoid. For the inertial navigation system, one has to deal with a couple of more coordinate frames related to the navigation instruments, the platform on which those are installed and the vehicle carrying the platform.

The obvious problem when dealing with several different coordinate frames is to establish the mutual relationship of a frame to all other frames so that the measurements in a frame can be transferred to the other frames. This is called coordinate transformations. Before describing the transformations, each coordinate system will be defined in detail in the next section. It should be noted that most of the derivation and equations are from the lecture notes of Inertial Geodesy (Jekeli, 1995a), to which one can directly refer for details.

2.2 Coordinate Frames

The first coordinate system to be discussed is the fundamental coordinate system called the inertial system, in which Newton's Laws of motion hold. The famous Newton's Laws of motion state that:

- First Law - Any object in a state of rest or having uniform linear motion will

remain in such a state unless acted upon by an unbalanced external force.

- Second Law - Unbalanced force acting on an object produces acceleration in the direction of the force, directly proportional to the force, and inversely proportional to the mass of the object.
- Third Law - For every action (or force) there is a reaction (or opposing force) of equal strength but opposite direction.

As one can notice already, the inertial system is just an abstraction in our world because of the existence of the gravitational field. Therefore, instead of pure inertial frame, the designation quasi-inertial frame is treated as a practical alternative to the inertial frame. The quasi-inertial frame is defined as Earth-centered, and accelerating, without rotating, around the sun.

To account for the acceleration due to the gravitational field, Newton's second law of motion needs to be modified. Newton's second law of motion is formulated as equation (2.3) in the pure inertial frame:

$$\mathbf{F} = \frac{\mathrm{d}}{\mathrm{dt}}\left(\mathrm{m_i}\dot{\mathbf{x}}\right), \tag{2.3}$$

where $\mathrm{m_i}\dot{\mathbf{x}}$ is the linear momentum of the particle with inertial mass $\mathrm{m_i}$ and velocity $\dot{\mathbf{x}}$. Assuming constant mass, the above equation will be simplified as:

$$\mathbf{F} = \mathrm{m_i}\ddot{\mathbf{x}}. \tag{2.4}$$

Under the existence of the gravitational field, the above equation should be modified to include the gravitational effect.

$$\mathrm{m_i}\ddot{\mathbf{x}} = \mathbf{F} + \mathrm{m_g}\mathbf{g} \tag{2.5}$$

The gravitational vector **g** is the proportional factor between the gravitational mass $\mathrm{m_g}$ and the gravitational force. Using the Principle of the Equivalence stating that $\mathrm{m_i}=\mathrm{m_g}=\mathrm{m}$, one can derive the fundamental equation in GPS/INS gravimetry.

$$\ddot{\mathbf{x}} = \mathbf{a} + \mathbf{g}, \tag{2.6}$$

where **a** = **F**/m is the acceleration caused by the applied (specific) force.

Now, we are ready to define the first fundamental frame called i-frame. The i-frame is attached to the Earth's center, is in free-fall, and is not rotating. The orientation of the i-frame is determined by the directions of quasars and fixed to the celestial sphere. It is freely falling because of the ambient gravitational field of the solar system. The International Earth Rotation Service (IERS) maintains, uses and makes available the inertial frame, being the realization of the International Celestial Reference System (ICRS). Specifically, the system is realized through the estimates of the coordinates of a set of quasars, the International Celestial Reference Frame (ICRF). The coordinates of a point in the i-frame are components of the position vector designated $\mathbf{x}^{\mathrm{i}}$. Note that the superscript denotes the frame in which the coordinates are represented.

The next frame to discuss is the Earth-centered-Earth-fixed (ECEF) frame, or e-frame with the origin also at the Earth's center of the mass (Figure 2.2). The orientation of the e-frame is defined by convention parallel to a mean polar axis and a mean equator on which the zero longitude is defined. The IERS establishes the

International Terrestrial Reference Frames (ITRF) is based on geodetic observations of satellites and quasars, as well as plate tectonic models (McCarthy, 1996). The example of an ECEF frame is the one realized by GPS. The coordinates of a point in ECEF frame are represented as $\mathbf{x}^e$ in the same way.

Another set of ECEF coordinates being used in geodesy is the conventional geodetic reference system. It consists of curvilinear coordinates (ϕ, λ) and the normal height (h) of an adopted ellipsoid of revolution (Figure 2.2).

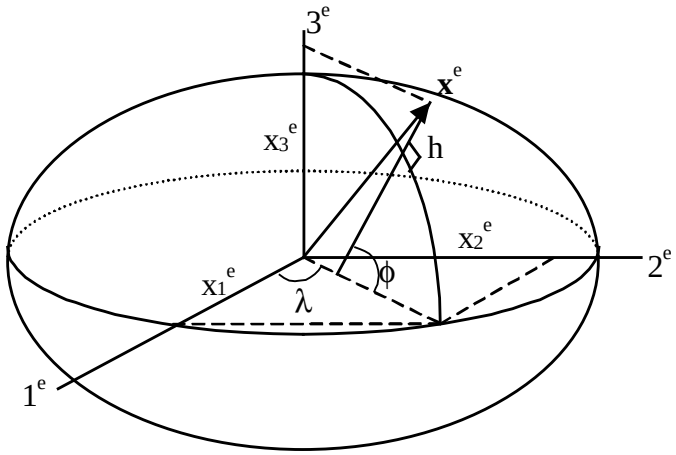

Figure 2.2 Earth-fixed-Earth-centered coordinates and geodetic coordinates with respect to an Earth ellipsoid.

The angles ϕ and λ, known as geodetic latitude and longitude, determine the horizontal positions and the ellipsoidal height does the vertical position. With a geocentric ellipsoid, the geodetic reference system could be used in place of the Cartesian ECEF coordinate system.

One of the most popular coordinate frames in the field of inertial navigation is the north-east-down frame, known as n-frame; the first axis points north, the second axis points east, and the third axis points down along the ellipsoid normal. The origin of the n-frame is either on the ellipsoid or at the location of the measurement system (Figure 2.3). The third axis does not pass through the Earth's center of mass because of the eccentricity of the ellipsoid.

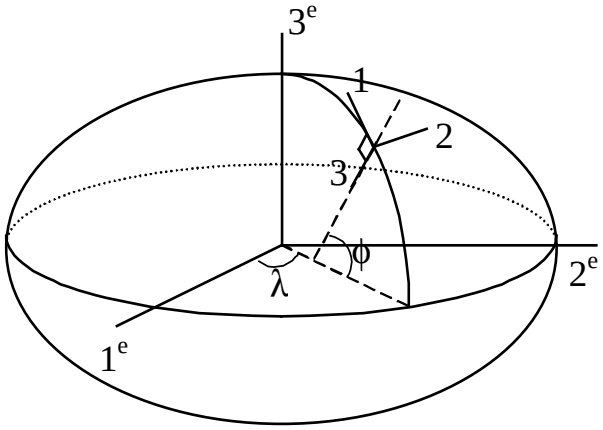

Figure 2.3 Local north-east-down coordinate frame.

It should be emphasized that this n-frame is not used to represent a vehicle's position because the n-frame itself moves with the vehicle carrying the navigation system. Therefore, only the third component of the coordinate $\mathbf{x}^n$ could be non-zero by definition. The advantage of the n-frame is that it provides the local direction of the vehicle motion through north, east and down velocities. Because the inertial sensors are always aligned with the local horizontal and vertical either mechanically or computationally, this frame is the one to which the platform or the sensor frame is directly related.

There are a couple more Cartesian coordinate frames related to the measurement systems and the vehicle itself. The body frame, or b-frame, refers to the vehicle itself. Conventionally, the axes are defined along the forward, right, and through-the-floor directions. The sensor frame, or s-frame, refers to the sensors physical or mechanical properties. It is used to model and identify instrument errors for data processing. The platform frame, or p-frame, refers to a physical set of fiducial axes for the platform. In addition, the accelerometer and the gyroscope have their own frame. Accelerometer frame may be defined as one of the accelerometer's sensitive axis (input axis) being aligned with a frame axis. The non-orthogonality of the other accelerometer is determined through a special calibration procedure. The origin of the accelerometer frame is the point of specific acceleration computation. Similarly, the gyro frame is orthogonal with only one of the input axes aligned along a frame axis. Its origin is the same as the accelerometer frame.

2.3 Coordinate Transformations

There are several ways to define the coordinate transformation from one to

another frame and three types of elements need to be considered: relative orientation, scale, and translation. Since the translation is the simple vector addition and scale is universally defined in general, the relative orientation would be the primary concern. Three angles are enough to describe the coordinate orientation transformation between orthogonal coordinate frames in three-dimensional space. The transformation between two Cartesian coordinate frames can be achieved with direction cosines, Euler angles, or quaternions.

2.3.1 Direction Cosines

Consider two concentric frames, s-frame and t-frame, and an arbitrary point in those frames, $\mathbf{x}^s$and $\mathbf{x}^t$ (Figure 2.4). With unit vectors in each frame, the coordinates of the point can be expressed as:

$$\mathbf{x}^s = x_1^s\mathbf{e}_1^s + x_2^s\mathbf{e}_2^s + x_3^s\mathbf{e}_3^s \tag{2.7}$$

$$\mathbf{x}^t = x_1^t\mathbf{e}_1^t + x_2^t\mathbf{e}_2^t + x_3^t\mathbf{e}_3^t \tag{2.8}$$

Each component in a position vector can be obtained by taking the inner product of the vector with the unit vector for the axis, e.g., $x_j^s = \mathbf{e}_j^s \cdot \mathbf{x}^s$, j=1,2,3. Analogously, the coordinates of the t-frame unit vector $\mathbf{e}_k^t$ in the s-frame are

$$c_{j,k} = \mathbf{e}_j^s \cdot \mathbf{e}_k^t, \tag{2.9}$$

$$\mathbf{e}_k^t = c_{1,k}\mathbf{e}_1^s + c_{2,k}\mathbf{e}_2^s + c_{3,k}\mathbf{e}_3^s. \tag{2.10}$$

Note that $c_{j,k}$ is the cosine of the angle between the j^{th} s-frame axis and k^{th} t-frame axis.

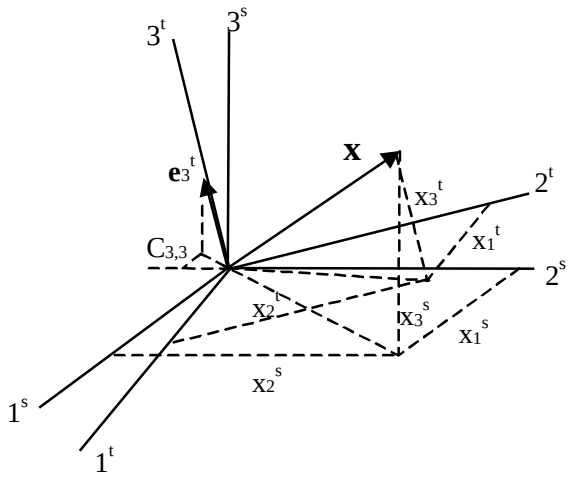

Figure 2.4 Vector **x** in Coordinate frames s and t.

By substituting (2.10) to (2.8) and comparing the result with (2.7), one can obtain the

transformation between the coordinates:

$$\mathbf{x}^s = C_t^s \mathbf{x}^t , \tag{2.11}$$

with the transformation matrix C_t^s given by

$$C_t^s = \begin{pmatrix} c_{1,1} & c_{1,2} & c_{1,3} \\ c_{2,1} & c_{2,2} & c_{2,3} \\ c_{3,1} & c_{3,2} & c_{3,3} \end{pmatrix}. \tag{2.12}$$

It should be noted that the matrix C_t^s, or the direction cosine matrix, is an orthogonal matrix:

$$C_t^s C_s^t = I = C_t^s (C_t^s)^T . \tag{2.13}$$

Understanding the transformation matrix, the transformation of any 3-by-3 matrix can be derived as follows. Consider a linear mapping in the t-frame, $\mathbf{y}^t = A^t \mathbf{x}^t$.
Then, using (2.11) and (2.13)

$$C_s^t \mathbf{y}^s = A^t C_s^t \mathbf{x}^s , \tag{2.14}$$

$$\mathbf{y}^s = C_t^s A^t C_s^t \mathbf{x}^s = A^s \mathbf{x}^s . \tag{2.15}$$

So, we reach the fact that

$$A^s = C_t^s A^t C_s^t . \tag{2.16}$$

2.3.2 Euler Angles

The relative orientation of the s- and t-frames could be described by a sequence of rotations about specific axes by Euler angles (Arfken, 1985, p. 199). The rotation about the 1, 2 and 3 axis with the angle of θ is given by

$$R_1(\theta) = \begin{pmatrix} 1 & 0 & 0 \\ 0 & \cos\theta & \sin\theta \\ 0 & -\sin\theta & \cos\theta \end{pmatrix}; R_2(\theta) = \begin{pmatrix} \cos\theta & 0 & -\sin\theta \\ 0 & 1 & 0 \\ \sin\theta & 0 & \cos\theta \end{pmatrix}; R_3(\theta) = \begin{pmatrix} \cos\theta & \sin\theta & 0 \\ -\sin\theta & \cos\theta & 0 \\ 0 & 0 & 1 \end{pmatrix} \tag{2.17}$$

Note that each $R_j(\theta)$ is also a direction cosine matrix; it is orthogonal $R_j^{-1}(\theta) = R_j^T(\theta)$; and the inverse is the reverse rotation $R_j^{-1}(\theta) = R_j(-\theta)$.

Let's suppose that the s-frame is the result of rotating the t-frame, first about 1-axis by α, then about 2-axis by β, and about 3-axis by γ. Then, the total transformation from t- to s-frame is $R_3(\gamma)R_2(\beta)R_1(\alpha)$ and it is the transformation matrix C_t^s. With the definition of rotation matrix in (2.17):

$$\begin{aligned} C_t^s &= R_3(\gamma)R_2(\beta)R_1(\alpha) \\ &= \begin{pmatrix} \cos\gamma\cos\beta & \cos\gamma\sin\beta\sin\alpha + \sin\gamma\cos\alpha & -\cos\gamma\sin\beta\cos\alpha + \sin\gamma\sin\alpha \\ -\sin\gamma\cos\beta & -\sin\gamma\sin\beta\sin\alpha + \cos\gamma\cos\alpha & \sin\gamma\sin\beta\cos\alpha + \cos\gamma\sin\alpha \\ \sin\beta & -\cos\beta\sin\alpha & \cos\beta\cos\alpha \end{pmatrix} \end{aligned} \tag{2.18}$$

It should be emphasized that the transformation is dependent on the order of the rotation. That is, $R_1(\alpha)R_2(\beta) \neq R_2(\beta)R_1(\alpha)$.

By comparing (2.18) with (2.12), the relation between Euler angle and the direction cosine can be found.

$$\alpha = \arctan\left(\frac{-c_{3,2}}{c_{3,3}}\right); \qquad \beta = \arcsin\left(c_{3,1}\right); \qquad \gamma = \arctan\left(\frac{-c_{2,1}}{c_{1,1}}\right) \tag{2.19}$$

If the rotation angles are small, we may use the first order approximation for cosine and sine terms. Then, (2.18) becomes

$$R_3(\gamma)R_2(\beta)R_1(\alpha) \approx \begin{pmatrix} 1 & \gamma & -\beta \\ -\gamma & 1 & \alpha \\ \beta & -\alpha & 1 \end{pmatrix} = \begin{pmatrix} 1 & 0 & 0 \\ 0 & 1 & 0 \\ 0 & 0 & 1 \end{pmatrix} - \begin{pmatrix} 0 & -\gamma & \beta \\ \gamma & 0 & -\alpha \\ -\beta & \alpha & 0 \end{pmatrix} = I - \Psi. \tag{2.20}$$

Ψ is a skew symmetric matrix of the small rotation angles. With (2.18), we also have

$$C_t^s \approx I - \Psi;\ C_s^t \approx (I - \Psi)^T = I - \Psi^T. \tag{2.21}$$

Note that the order of rotations about the axes does not affect the result in this approximation.

2.3.3 Quaternions

A quaternion is a number that represents a vector in a specific four-dimensional algebra. It is a kind of generalized complex variable so that the properties and manipulations of the quaternion are very similar to those of the complex variable.

The definition of the quaternion is given by

$$q = a + ib + jc + kd, \tag{2.22}$$

where q is the quaternion; a, b, c, d are real numbers; and i, j, k are the imaginary units having properties as follows:

$$i^2 = -1;\ j^2 = -1;\ k^2 = -1 \tag{2.23}$$

$$ij = -ji = k; \qquad jk = -kj = i; \qquad ki = -ik = j. \tag{2.24}$$

The conjugate of the quaternion and the square of the magnitude of q are

$$q^* = a - ib - jc - kd \tag{2.25}$$

$$qq^* = q^*q = a^2 + b^2 + c^2 + d^2. \tag{2.26}$$

When a complex number $e^{i\theta}$ multiplies an arbitrary complex number, $z = \rho e^{i\phi}$, the vector represented by z is rotated by the angle θ

$$e^{i\theta}z = e^{i\theta}\rho e^{i\phi} = \rho e^{i(\theta+\phi)}. \tag{2.27}$$

Analogously, a particular type of quaternion, rotation quaternion, can describe the rotation of the three dimensional vectors in Euclidean space. Consider the quaternion

$$q_\zeta = \cos\frac{\zeta}{2} + \sin\frac{\zeta}{2}(ib + jc + kd) = a_\zeta + ib_\zeta + jc_\zeta + kd_\zeta, \tag{2.28}$$

where the numbers b, c and d satisfy the condition

$$b^2 + c^2 + d^2 = 1. \tag{2.29}$$

Consider the representation of this quaternion analogously to Euler's equation, $e^{i\theta} = \cos\theta + i\sin\theta$,

$$q_\zeta = e^{\frac{\zeta}{2}(ib+jc+kd)} \tag{2.30}$$

The magnitude of the above quaternion is one and the exponent term represents the three dimensional vector with magnitude $\zeta/2$ and the direction cosines b, c, and d. When a three-dimensional vector, $\mathbf{x} = ix_1 + jx_2 + kx_3$, is pre multiplied by this quaternion and post multiplied by its complex conjugate, the vector is rotated about the vector $ib + jc + kd$ by the angle ζ to the vector $\mathbf{x}'$:

$$\mathbf{x}' = q_\zeta \mathbf{x} q_\zeta^* \tag{2.31}$$

The vector $ib + jc + kd$ is called rotation vector whose direction specifies the single axis about which one rotation transforms one frame to another. It should be noted that there is always a rotation vector for an arbitrary transformation.

Now, let's relate the rotation quaternion with the usual orthogonal transformation C_t^s. Consider a unit rotation vector $\mathbf{e}_\zeta^t$, whose direction cosines in the t-frame are b, c and d (Figure 2.5).

$$\mathbf{e}_\zeta^t = \begin{pmatrix} b \\ c \\ d \end{pmatrix} = \begin{pmatrix} \sin\theta\cos\lambda \\ \sin\theta\sin\lambda \\ \cos\theta \end{pmatrix} \tag{2.32}$$

Note that the representation of the spherical polar coordinates is used. To describe the rotation about this axis, a new frame called ζ-frame needs to be defined, whose 3-axis lies along the direction of $\mathbf{e}_\zeta^t$, and 1-axis is in the plane formed by $\mathbf{e}_\zeta^t$ and the 3-axis of the t-frame. Then, the transformation from t- to ζ-frame is given by

$$C_t^\zeta = R_2(-\theta) R_3(-\pi + \lambda) \tag{2.33}$$

By definition, the matrix for the ζ rotation in the ζ-frame is $R_3(\zeta)$. According to (2.16), the same rotation in the t-frame is given by

$$C_t^s = C_\zeta^t R_3(\zeta) C_t^\zeta \tag{2.34}$$

With (2.33) and (2.32), the transformation C_t^ζ can be represented in terms of quaternion elements.

$$C_t^\zeta = \begin{pmatrix} \dfrac{-db}{\sqrt{1-d^2}} & \dfrac{-dc}{\sqrt{1-d^2}} & \sqrt{1-d^2} \\ \dfrac{c}{\sqrt{1-d^2}} & \dfrac{-b}{\sqrt{1-d^2}} & 0 \\ b & c & d \end{pmatrix} \tag{2.35}$$

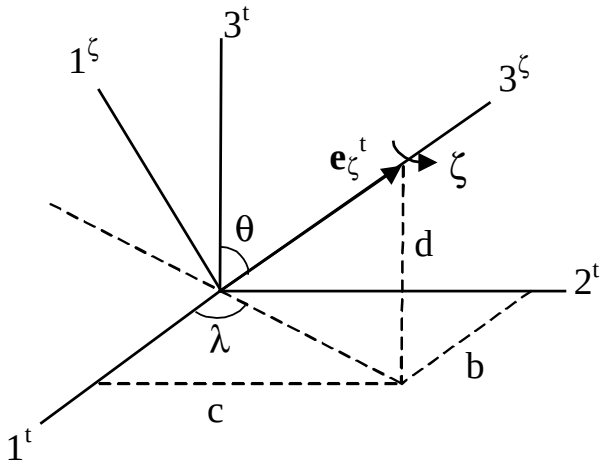

Figure 2.5 The unit rotation vector $\mathbf{e}_\zeta^t$; and the ζ- and t-frames.

Finally, the transformation C_t^s is obtained with (2.28) and (2.34).

$$C_t^s = \begin{pmatrix} a_\zeta^2 + b_\zeta^2 - c_\zeta^2 - d_\zeta^2 & 2(b_\zeta c_\zeta + d_\zeta a_\zeta) & 2(b_\zeta d_\zeta - c_\zeta a_\zeta) \\ 2(b_\zeta c_\zeta - d_\zeta a_\zeta) & a_\zeta^2 + c_\zeta^2 - b_\zeta^2 - d_\zeta^2 & 2(c_\zeta d_\zeta + a_\zeta b_\zeta) \\ 2(b_\zeta d_\zeta + c_\zeta a_\zeta) & 2(c_\zeta d_\zeta - a_\zeta b_\zeta) & a_\zeta^2 + d_\zeta^2 - b_\zeta^2 - c_\zeta^2 \end{pmatrix} \tag{2.36}$$

The above equation shows the clear relationship between the transformation matrix and quaternion. Because of their stable numerical characteristics, quaternion methods are applied in most practical strapdown navigation systems for the attitude determination (Da, 1997). Details on determining attitude using quaternion will be discussed in Chapter 5.

2.4 Some necessary definitions and derivations

2.4.1 Axial Vectors

In inertial navigation systems, the concept of axial vector is applied in the differential equations for the angular data output from the Inertial Measurement Unit (IMU). The axial vector, by definition, is the ordered triple of Eulerian angles (α, β, γ). Because of the dependency of transformations on the order of the rotation, the axial vector does not perfectly behave like vectors. For example, the commutativity property of the two vectors is not applicable for the axial vectors.

If, however, the angles are small, the axial vector behaves like a vector. Because the purpose of introducing axial vectors in this study is to represent the attitude errors in INS, we can allow the small angle constraints. Therefore, the triple of

small angles $\psi = (\alpha, \beta, \gamma)^T$ will be treated as a vector through this study.

Under the assumption of small angle rotation, the transformation from t- to s-frame can be written as

$$\mathbf{x}^s = C_t^s \mathbf{x}^t = (I - \Psi)\mathbf{x}^t = \mathbf{x}^t - \Psi \mathbf{x}^t = \mathbf{x}^t - \psi \times \mathbf{x}^t . \tag{2.37}$$

In addition, the axial vector in the t-frame can be transformed to the s-frame by applying the transformation matrix.

$$\psi^S = C_t^s \psi^t ; \qquad \Psi^S = C_t^s \Psi^t C_s^t \tag{2.38}$$

2.4.2 Angular Rates

To describe the frames that are rotating with respect to each other, it is necessary to define a systematic notation for the angular rates, $\omega = (\omega_1\, \omega_2\, \omega_3)$, between two frames. The angular velocity of the t-frame with respect to the s-frame with coordinates in the t-frame is denoted as ω_{st}^t. Considering the angular velocity as a vector, one can reach the following properties:

$$\omega_{st}^t = C_s^t \omega_{st}^s = -C_s^t \omega_{ts}^s , \tag{2.39}$$

$$\omega_{st}^t = \omega_{su}^t + \omega_{ut}^t . \tag{2.40}$$

The skew-symmetric matrix for the angular rates is defined as

$$\left[\omega_{st}^t \times\right] = \Omega_{st}^t ; \; \Omega_{st}^t = \begin{pmatrix} 0 & -\omega_3 & \omega_2 \\ \omega_3 & 0 & -\omega_1 \\ -\omega_2 & \omega_1 & 0 \end{pmatrix}. \tag{2.41}$$

It should be emphasized that the angular rate does not have to be small because by definition, it is the infinitesimal angle in the ratio to infinitesimal increments of time.

2.4.3 Differential Equation of the Transformation

When two frames are rotating with respect to each other, the relative orientation is changing with respect to time. Therefore, it is necessary to derive the differential equation of the transformation with respect to time. The differential equation of the transformation as a function of time is given by

$$\dot{C}_t^s = \lim_{dt \to 0} \frac{C_t^s(t + dt) - C_t^s(t)}{dt} \tag{2.42}$$

Assuming the small changes in the transformation for the time interval dt, the transformation at time t+dt can be expressed as:

$$C_t^s(t + dt) = \delta C^s C_t^s(t) = (I - \Psi^s) C_t^s(t) \tag{2.43}$$

Substituting (2.43) into (2.42) yields

$$\dot{C}_t^s = \lim_{dt \to 0} \frac{(I - \Psi^s) C_t^s(t) - C_t^s(t)}{dt} = -\lim_{dt \to 0} \frac{\Psi^s C_t^s(t)}{dt} = -\Omega_{ts}^s C_t^s . \tag{2.44}$$

Using (2.16),

$$\Omega^s_{ts} = -\Omega^s_{st} = -C^s_t \Omega^t_{st} C^t_s . \tag{2.45}$$

The final form of the differential equation for the transformation is given by

$$\dot{C}^s_t = C^s_t \Omega^t_{st} . \tag{2.46}$$

The well-known law of Coriolis is derived using (2.46). By taking the time derivative of (2.11),

$$\dot{\mathbf{x}}^s = C^s_t \dot{\mathbf{x}}^t + \dot{C}^s_t \mathbf{x}^t = C^s_t (\dot{\mathbf{x}}^t + \Omega^t_{st} \mathbf{x}^t); \qquad C^t_s \dot{\mathbf{x}}^s = \dot{\mathbf{x}}^t + \Omega^t_{st} \mathbf{x}^t \tag{2.47}$$

The differential equation for the quaternion elements can also be derived analogously. Using (2.36), one can solve for a^2_ζ in terms of the trace of C^s_t.

$$a^2_\zeta = \frac{1}{4}(\mathrm{tr}(C^s_t) + 1) \tag{2.48}$$

Taking time derivative of the above equation

$$2 a_\zeta \dot{a}_\zeta = \frac{1}{4}\mathrm{tr}(\dot{C}^s_t) = \frac{1}{4}\mathrm{tr}(C^s_t \Omega^t_{st}) . \tag{2.49}$$

Substituting (2.36) and (2.41) into (2.49)

$$\dot{a}_\zeta = \frac{1}{2}(b_\zeta \omega_1 + c_\zeta \omega_2 + d_\zeta \omega_3) , \tag{2.50}$$

where $\omega^t_{st} = (\omega_1, \omega_2, \omega_3)$.

Also, from (2.12) and (2.36), one can find that

$$4 a_\zeta b_\zeta = c_{23} - c_{32} . \tag{2.51}$$

With (2.46), the time derivative of the above equation is given as

$$4(\dot{a}_\zeta b_\zeta + a_\zeta \dot{b}_\zeta) = \dot{c}_{23} - \dot{c}_{32} = c_{21}\omega_2 - c_{22}\omega_1 + c_{31}\omega_3 - c_{33}\omega_1 . \tag{2.52}$$

Substituting the elements in the last equation with corresponding ones from (2.36) and solving for $\dot{b}_\zeta$,

$$\dot{b}_\zeta = \frac{1}{2}(-a_\zeta \omega_1 - d_\zeta \omega_2 + c_\zeta \omega_3) . \tag{2.53}$$

In the same way, one can derive the equations for $\dot{c}_\zeta$ and $\dot{d}_\zeta$.

$$\dot{c}_\zeta = \frac{1}{2}(d_\zeta \omega_1 - a_\zeta \omega_2 - b_\zeta \omega_3) \tag{2.54}$$

$$\dot{d}_\zeta = \frac{1}{2}(-c_\zeta \omega_1 + b_\zeta \omega_2 - a_\zeta \omega_3) \tag{2.55}$$

2.5 Specific Coordinate Transformation

2.5.1 Inertial Frame and ECEF frame

The relationship between the quasi-inertial and ECEF frame is quite trivial. Because e- and i-frames have the same origin, the center of the Earth's mass, and the same direction of the 3-axis, these frames are different by a rotation only about the 3-axis. Assuming the uniform rotation rate of the Earth, ω_e, the angular rate of the e-

frame with respect to the i-frame is given by

$$\omega_{ie}^{e} = (0\ 0\ \omega_e) \tag{2.56}$$

So, the transformation matrix from i- to e-frame is simply a rotation about the 3-axis by $\omega_e t$.

$$C_i^e = R_3(\omega_e t) = \begin{pmatrix} \cos\omega_e t & \sin\omega_e t & 0 \\ -\sin\omega_e t & \cos\omega_e t & 0 \\ 0 & 0 & 1 \end{pmatrix} \tag{2.57}$$

2.5.2 ECEF and Geodetic coordinates

As mentioned before, the ECEF coordinates can be equivalently represented with the geodetic latitude, longitude and height. The relationship between the ECEF and geodetic coordinates is given by

$$\begin{pmatrix} x_1^e \\ x_2^e \\ x_3^e \end{pmatrix} = \begin{pmatrix} (N+h)\cos\phi\cos\lambda \\ (N+h)\cos\phi\sin\lambda \\ (N(1-e^2)+h)\sin\phi \end{pmatrix}, \tag{2.58}$$

where N is the radius of curvature of the ellipsoid in the prime vertical plane,

$$N = \frac{a}{\sqrt{1-e^2\sin^2\phi}}, \tag{2.59}$$

a is the length of the semi-major axis, $e^2 = 2f - f^2$ is the square of the first eccentricity , and f is the flattening of the ellipsoid. The radius of curvature in the meridian M is also given for a future reference.

$$M = \frac{a(1-e^2)}{(1-e^2\sin^2\phi)^{3/2}}. \tag{2.60}$$

The inverse relationship of (2.58) is usually presented in iterative form. For instance:

$$\begin{pmatrix} \phi \\ \lambda \\ h \end{pmatrix} = \begin{pmatrix} \arctan\left(\dfrac{x_3^e}{\sqrt{(x_1^e)^2+(x_2^e)^2}}\left(1+\dfrac{e^2N\sin\phi}{x_3^e}\right)\right) \\ \arctan\left(\dfrac{x_2^e}{x_1^e}\right) \\ \dfrac{\sqrt{(x_1^e)^2+(x_2^e)^2}}{\cos\phi} - N \end{pmatrix} \tag{2.61}$$

For details on the above derivations, see Rapp (1994).

2.5.3 ECEF and Navigation Frame

Because the e- and n-frame are not concentric, the transformation is more or

less complicated. The orientation transformation needs two successive rotations; first rotate about the local east axis by the angle $(\pi/2+\phi)$; then rotate about the new 3-axis by the angle $-\lambda$:

$$C_n^e = R_3(-\lambda)R_2(\pi/2+\phi) = \begin{pmatrix} -\sin\phi\cos\lambda & -\sin\lambda & -\cos\phi\cos\lambda \\ -\sin\phi\sin\lambda & \cos\lambda & -\cos\phi\sin\lambda \\ \cos\phi & 0 & -\sin\phi \end{pmatrix}. \quad (2.62)$$

The angular rates can be derived using $\Omega_{en}^n = C_e^n \dot{C}_n^e$ as in (2.46):

$$\omega_{en}^n = (\dot{\lambda}\cos\phi \quad -\dot{\phi} \quad -\dot{\lambda}\sin\phi)^T. \quad (2.63)$$

By intuition, the angular rates of the n-frame with respect to the i-frame can be also given as:

$$\omega_{in}^n = ((\dot{\lambda}+\omega_e)\cos\phi \quad -\dot{\phi} \quad -(\dot{\lambda}+\omega_e)\sin\phi)^T \quad (2.64)$$

2.5.4 Body and Navigation Frame

The transformation between the body and navigation frame is also represented by the three successive rotations; about 1-axis by the negative roll angle, $-\eta$; about 2-axis by the negative pitch angle, $-\chi$; and about 3-axis by the negative yaw angle, $-\alpha$.

$$C_b^n = R_3(-\alpha)R_2(-\chi)R_1(-\eta) \quad (2.65)$$

From (2.65) and (2.46), one can derive the relationship between the angular rates and the attitude rates.

$$\begin{pmatrix} \dot{\eta} \\ \dot{\chi} \\ \dot{\alpha} \end{pmatrix} = \begin{pmatrix} 1 & \sin\eta\tan\chi & \cos\eta\tan\chi \\ 0 & \cos\eta & -\sin\eta \\ 0 & \sin\eta\sec\chi & \cos\eta\sec\chi \end{pmatrix} \omega_{nb}^b \quad (2.66)$$

The above differential equation must be integrated to obtain the attitude information of the vehicle from given body to navigation frame rates. It should be noted that the equation is singular for pitch angles of 90 degrees. The alternative differential equation is the one in terms of the quaternion (2.50), (2.53)-(2.55). In this case, no singularity exists. So, the quaternion method is preferred for high dynamic aircraft such as the military plane.

CHAPTER 3

GLOBAL POSITIONING SYSTEM AND INERTIAL NAVIGATION SYSTEM

3.1 GPS System Overview

3.1.1 Introduction

The NAVSTAR (Navigation System with Timing And Ranging) GPS was initiated in 1973 by the Joint Program Office (JPO) at the US Air Force Systems Command's Space Division. The original objectives of the GPS include point positioning, the determination of a vehicle's position and velocity, and the precise coordination of time. It is designed as an all-weather, continuous, passive and space-based navigation system. Currently, it is fully operating and at least four satellites are simultaneously observable in any place of the world at any time.

The GPS satellite continuously transmits the signal with the transmission time and ephemeris information. Once the receiver receives the signal, the signal travel time from the satellite to the receiver can be calculated. By multiplying the travel time with the velocity of the signal, one can get the pseudorange. Here, the term "pseudorange" is used instead of "true range", as the clocks of the satellite and the receiver are never perfectly synchronized. If the satellite positions are known, four simultaneous pseudoranges are necessary to solve for the receiver position as well as the clock errors.

3.1.2 Space Segment

The GPS consists of three segments: space segment, control segment and user segment. The space segment is responsible for the GPS satellites from development to launch. Currently, 27 high-altitude (22,000km) GPS satellites are on six near-circular orbital planes with 55^{o} inclination (except Block I) and 12 sidereal hour period. With this constellation, four to eight GPS satellites above 15^{o} elevation angle are simultaneously observable from anywhere on the earth at any time of the day.

So far, four main classes of GPS satellites have been developed. These are Block I, Block II, Block IIA and Block IIF. The first generation Block I satellites were launched by JPO between 1978 to 1985. The inclinations of the Block I orbits are 63^{o} and the expected life time was 4.5 year. There is, however, a Block I satellite still in

operation (PRN 12). This PRN 12 is quite useful for satellite clock studies because the Selective Availability (SA) has not been implemented in Block I satellites (Heroux and Kouba, 1995). The first Block II satellite, PRN 14, was launched in 1989 with the inclination of 55^{o}. The essential difference between the Block I and Block II satellites is that Block II signal is restricted to civilian users while Block I is fully available. The Block IIA satellites are equipped with mutual communication capability and all 15 satellites were launched since 1990. Block IIR satellites, designed to replace the Block II satellites, will have the capability to autonomously navigate (AUTONAV) themselves and generate their own 50 Hz navigation message data. The designed life is 10 years.

The GPS satellite carries a high performance rubidium or cesium frequency standard as a precise time base with a proportional accuracy of 10^{-13} to 10^{-14}. From the frequency standards, GPS satellites produce the fundamental L band frequency of 10.23 MHz. Two coherently derived carriers L_1 and L_2 are generated by multiplying the fundamental frequency by 154 and 120 (L_1 = 1575.42MHz, L_2 = 1227.60MHz). The L_1 carrier is modulated by C/A (Coarse/Acquisition code) and P code (or Y code), while L_2 is modulated by P or Y code only. In addition, the information about the satellite clock, position and velocity is also modulated onto the carriers. The C/A code is designated as the Standard Positioning Service (SPS), and it is available for civilian use. The P code is also designated as the Precise Positioning Service (PPS), and the Y code is generated by the modulo 2 sum of the P-code and an encrypting W-code. Therefore, P or Y code is only accessible to the authorized users like U.S. military. The effective wavelengths of the C/A and P code are approximately 300m and 30m, respectively.

The Selective Availability (SA) and the Anti-Spoofing (AS) are implemented to prevent the civilian from full use of the GPS system. SA degrades the user's positioning accuracy from 30-40m to approximately 100m by dithering the satellite clock (δ-process) and manipulating the ephemerides (ε-process). Since the δ-process is achieved by introducing various errors into the fundamental frequency of the satellite clock, the effect appears in the code and carrier pseudorange in the same way. By differencing the pseudoranges from two receivers, the dithering effect can be significantly reduced. In absolute positioning, however, the satellite clock should be estimated to do precise positioning (Kwon et al., 1999). The ε-process is achieved by truncating the orbital information so that the precise position of the satellite cannot be calculated. The erroneous satellite position has a direct impact on the receiver position which is degraded up to 40m in absolute single positioning. In baseline determination, however, only the relative satellite position errors produce the relative baseline errors.

As stated previously, the Block II satellites have the capability to "turn off" the P-code or generate the encrypted code (Y-code) so that unauthorized user cannot have the full access to the system. This feature is permanently implemented from January 31, 1994. It should be noted that the integer ambiguity resolution requires longer time of averaging or filtering to compensate for the AS effect (Yang, 1995).

3.1.3 Control Segment

The control segment consists of a master control station, worldwide monitor stations, and ground control stations. They are responsible for tracking the satellites for the orbit and clock determination, prediction modeling, time synchronization of the satellites, and updating the navigation message for every satellite. The master control station, located in Colorado Springs, is responsible for overall management of the remote monitoring and transmission sites. The monitor stations check altitude, position, speed, and overall health of each satellite twice a day. Any anomalous behavior of the satellite is reported to the master control station for analysis. Ground control stations are the communication links to the satellites and track the satellites from horizon to horizon. They also transmit correction information to individual satellites via S-band radio links (Hofmann-Wellenhof et al., 1997).

3.1.4 User Segment

The user segment consists of numerous types of GPS receivers and the GPS user community. This segment uses broadcast data from satellites and determines the precise position of the receiver antenna. There are literally thousands of GPS users such as navigators, surveyors, geodesists and other users who require position information.

3.2 GPS Data Modeling

3.2.1 GPS Observables and Observation Equation

There are two types of observables provided by the GPS receiver, namely code pseudorange and carrier phase. The pseudorange is derived from the signal travel time calculated from the satellite and receiver clock information and carrier phase is derived from the difference between the phase of the carrier received from a satellite and a reference phase generated by the receiver's oscillator. The observation equation for the pseudoranges and carrier phases are given as follows (Goad and Yang, 1995):

$$
\begin{aligned}
\Phi_{i,1}^{j} &= \rho_i^j - \frac{I_i^j}{f_1^2} + T_i^j + \lambda_1 N_{i,1}^j + c(dt_i - dt^j) + \lambda_1(\varphi_0^j - \varphi_{i0})_1 + \varepsilon_{i,1}^j \\
\Phi_{i,2}^{j} &= \rho_i^j - \frac{I_i^j}{f_2^2} + T_i^j + \lambda_2 N_{i,2}^j + c(dt_i - dt^j) + \lambda_2(\varphi_0^j - \varphi_{i0})_2 + b_{i,1} + \varepsilon_{i,2}^j \\
P_{i,1}^{j} &= \rho_i^j + \frac{I_i^j}{f_1^2} + T_i^j + c(dt_i - dt^j) + b_{i,2} + e_{i,1}^j \\
P_{i,2}^{j} &= \rho_i^j + \frac{I_i^j}{f_2^2} + T_i^j + c(dt_i - dt^j) + b_{i,3} + e_{i,2}^j
\end{aligned}
\quad , \qquad (3.1)
$$

where

$P_{i,1}^j, P_{i,2}^j$ - pseudorange from satellite j measured at station i on L_1 and L_2,

$\Phi_{i,1}^j, \Phi_{i,2}^j$ - phase ranges from satellite j measured at station i on L_1 and L_2,

ρ_i^j - geometric range between satellite j and receiver i,

T_i^j - tropospheric refraction term from satellite j to receiver i,

c - the vacuum speed of light

dt_i, dt^j - clock error for receiver i and satellite j, respectively,

f_1, f_2 - frequencies of L_1 and L_2 carrier,

λ_1, λ_2 - wavelengths of L_1 and L_2 carrier,

$\frac{I_i^j}{f_1^2}, \frac{I_i^j}{f_2^2}$ - ionospheric refraction terms for L_1 and L_2, respectively,

$\varphi_0^j, \varphi_{i0}$ - initial fractional phases at the transmitter j and receiver i,

$N_{i,1}^j, N_{i,2}^j$ - integer ambiguities associated with $\Phi_{i,1}^j$ and $\Phi_{i,2}^j$, respectively,

$e_{i,1}^j, e_{i,2}^j$ - measurement noise for pseudoranges on L_1 and L_2,

$\varepsilon_{i,1}^j, \varepsilon_{i,2}^j$ - measurement noise for phases on L_1 and L_2,

$b_{i,1}, b_{i,2}, b_{i,3}$ - $b_{i,1}$ is the interchannel bias between L_1 phase and L_2 phase, $b_{i,2}$ and $b_{i,3}$ are the interchannel bias between L_1 phase and $P_{i,1}^j, P_{i,2}^j$, respectively.

Note that the phase observation equations have additional terms for ambiguity and the effect of the ionosphere appears in opposite way to that of the pseudorange.

The noise level of the phase is known to be on the order of a few tenths of a millimeter while that of the pseudorange is much larger. The P-code pseudorange can be as good as ±20cm but the C/A code pseudorange could be worse than ±1m depending on the types of receiver (Yang, 1995; Grejner-Brzezinska, 1995). The interchannel biases for i-th receiver are caused by time non-synchronization of the four measurements. This non-synchronization results from the fact that the L1 and L2 signal must travel through different hardware paths inside the receiver and transmitter (Coco, 1991).

The ionospheric effect can be cancelled or reduced by forming the so-called ion-free combination, given in the next section. The tropospheric effect, however, cannot be cancelled by any combination of observables because of its nondispersive characteristics. Thus, it is modeled using the information about the temperature, humidity and the atmospheric pressure as well as the elevation of the space vehicle (SV). The well-known tropospheric model can be found in Goad and Goodman (1974), called modified Hopfield model. The effect of the troposphere can reach up to one decimeter (Seeber, 1993, p.290).

3.2.2 Differencing and Combinations of GPS Measurements

As described in the previous section, the GPS observables are affected by many nuisance parameters such as clock biases, ionospheric effect and AS effect. To eliminate or reduce the errors caused by these parameters, the differencing technique can be used. Basically, the differencing eliminates or significantly reduces the errors from a common satellite or receiver. The single differenced measurement is obtained by two simultaneous observables of satellite k, tracked by two receivers i and j:

$$\begin{aligned}
\Phi_{ij,1}^{k} &= \rho_{ij}^{k} - \frac{I_{ij}^{k}}{f_1^2} + T_{ij}^{k} + \lambda_1 N_{ij,1}^{k} + c \cdot dt_{ij} - \lambda_1 \cdot \varphi_{ij0,1} + \varepsilon_{ij,1}^{k} \\
\Phi_{ij,2}^{k} &= \rho_{ij}^{k} - \frac{I_{ij}^{k}}{f_2^2} + T_{ij}^{k} + \lambda_2 N_{ij,2}^{k} + c \cdot dt_{ij} - \lambda_2 \cdot \varphi_{ij0,2} + b_{ij,1} + \varepsilon_{ij,2}^{k} \\
P_{ij,1}^{k} &= \rho_{ij}^{k} + \frac{I_{ij}^{k}}{f_1^2} + T_{ij}^{k} + c \cdot dt_{ij} + b_{ij,2} + e_{ij,1}^{k} \\
P_{ij,2}^{k} &= \rho_{ij}^{k} + \frac{I_{ij}^{k}}{f_2^2} + T_{ij}^{k} + c \cdot dt_{ij} + b_{ij,3} + e_{ij,2}^{k}
\end{aligned} \tag{3.2}$$

From the above equations, one can notice that the satellite clock error as well as the satellite initial phase term are cancelled by the differencing. The errors related to the receivers, however, such as receiver clock errors, interchannel biases and initial phases are still present. These errors make it impossible or very difficult to estimate the integer phase ambiguities. Because the interchannel biases are nearly collinear with the ionospheric effect as well as the integer ambiguity terms, it is not possible to estimate those unknowns separately. Furthermore, the initial phase cannot be separated easily from the ambiguity as seen in equation (3.2). Therefore, a more favorable way to estimate or recover the integer phase ambiguity is to use the double differencing technique explained next.

The receiver clock error and receiver initial phase terms can be cancelled by performing one more differencing using the single differenced measurement from another satellite l (Figure 3.1).

$$\begin{aligned}
\Phi_{ij,1}^{kl} &= \rho_{ij}^{kl} - \frac{I_{ij}^{kl}}{f_1^2} + T_{ij}^{kl} + \lambda_1 N_{ij,1}^{kl} + \varepsilon_{ij,1}^{kl} \\
\Phi_{ij,2}^{kl} &= \rho_{ij}^{kl} - \frac{I_{ij}^{kl}}{f_2^2} + T_{ij}^{kl} + \lambda_2 N_{ij,2}^{kl} + \varepsilon_{ij,2}^{kl} \\
P_{ij,1}^{kl} &= \rho_{ij}^{kl} + \frac{I_{ij}^{kl}}{f_1^2} + T_{ij}^{kl} + e_{ij,1}^{kl} \\
P_{ij,2}^{kl} &= \rho_{ij}^{kl} + \frac{I_{ij}^{kl}}{f_2^2} + T_{ij}^{kl} + e_{ij,2}^{kl}
\end{aligned} \tag{3.3}$$

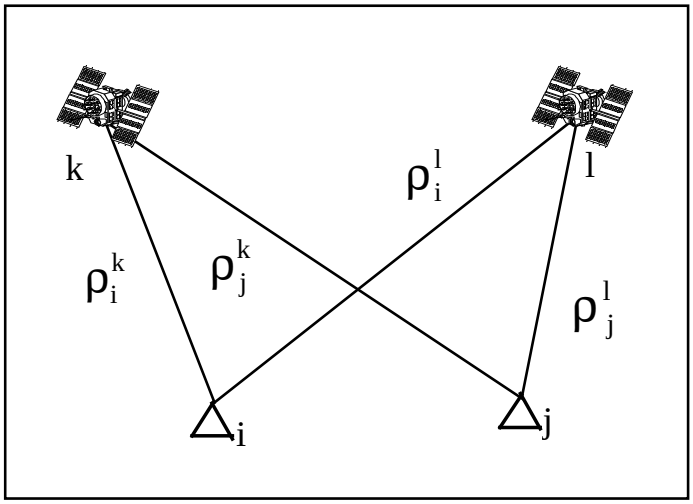

Figure 3.1 Scheme of the double differencing.

Because of the advantage to determine the integer ambiguity, the double differencing is the most popular method being used in precise Differential GPS (DGPS) positioning.

Further differencing is possible between double differenced measurements obtained at two successive epochs to eliminate the phase ambiguity N_1 and N_2. Because the ambiguities remain constant over time unless a cycle slip or loss of lock occurs, those can be cancelled out. The triple differencing over time span dt is expressed as follows:

$$\begin{aligned}
\Phi_{ij,1,dt}^{kl} &= \rho_{ij,dt}^{kl} - \frac{I_{ij,dt}^{kl}}{f_1^2} + T_{ij,dt}^{kl} + \varepsilon_{ij,1,dt}^{kl} \\
\Phi_{ij,2,dt}^{kl} &= \rho_{ij,dt}^{kl} - \frac{I_{ij,dt}^{kl}}{f_2^2} + T_{ij,dt}^{kl} + \varepsilon_{ij,2,dt}^{kl} \\
P_{ij,1,dt}^{kl} &= \rho_{ij,dt}^{kl} + \frac{I_{ij,dt}^{kl}}{f_1^2} + T_{ij,dt}^{kl} + e_{ij,1,dt}^{kl} \\
P_{ij,2,dt}^{kl} &= \rho_{ij,dt}^{kl} + \frac{I_{ij,dt}^{kl}}{f_2^2} + T_{ij,dt}^{kl} + e_{ij,2,dt}^{kl}
\end{aligned} \tag{3.4}$$

The advantage of triple differencing is that it is very easy to detect any cycle slip. As soon as the cycle slip occurs, the effect will clearly appear as an outlier. It should be emphasized that the equation (3.4) is no longer equivalent with (3.3) because, by taking triple differences, loss of information and redundancy occurs for phase and code observables, respectively. In other words, the number of observations of code (last two equations) reduced by one resulting in the loss of redundancy in the triple

differencing. In addition, the integer characteristic of the ambiguity is lost in phase observables. Therefore, when forming models in terms of the differenced observables, one has to check whether the new model is equivalent to the original ones. For conditions to check the equivalency, one can refer to Schaffrin and Grafarend (1986).

The characteristic dual frequency measurement in GPS leads to the possible elimination or at least significant reduction of the ionospheric effect. For example, using two phase measurements in L_1 and L_2, one can form ion-free phase measurements as follows:

$$\Phi_{1,2} = \alpha_1 \Phi_1 + \alpha_2 \Phi_2, \tag{3.5}$$

where $\alpha_1 = \dfrac{f_1^2}{f_1^2 - f_2^2}$, $\alpha_2 = \dfrac{f_2^2}{f_1^2 - f_2^2}$.

Note that the integer characteristics of the phase ambiguity is lost by forming this ion-free combination. There exist, however, phase combinations which form ion-free observables preserving the integer characteristics of the ambiguity, for example $\alpha_1 = 77$, $\alpha_2 = -60$. For details, refer to Han and Rizos (1996).

Another popular combination of the GPS measurements is the so-called widelane combination, obtained by subtracting the L_2 phase from L_1 phase. The frequency of the widelane is $f_w = 347.82$ MHz and the corresponding equivalent wavelength $\lambda_w = 86.2$ cm. This increased widelane wavelength provides increased ambiguity spacing so that the widelane ambiguity ($N_w = N_1 - N_2$) can be resolved more easily (Hofmann-Wellenhof, 1997, p.214).

Before ending this section, it should be mentioned that the noise level of the combined or differenced observations is larger than that of the original observation. Assuming the same noise level for both phases, one can apply simple error propagation law for the widelane observable. The noise of the widelane is larger by the factor of $\sqrt{2}$ than that of a single phase. In addition, the differencing introduces statistical correlations among the observables while the original data set of GPS is assumed to be uncorrelated. Therefore, one has to consider the proper correlations when making a new, differenced model equivalent to the original one (Schaffrin and Grafarend, 1986).

3.3 Relative GPS Kinematic Positioning in Post-Processing Mode

Since the role of GPS in this research is to provide the kinematic acceleration derived from the precise GPS position, a general concept and adjustment technique in terms of post-processing kinematic GPS positioning is addressed in this section. In general, the relative positioning, namely the baseline vector determination, shows higher accuracy than the absolute positioning because the errors in GPS measurements such as satellite orbit error, atmospheric effect, and the clock errors can be cancelled or reduced through differencing. Currently, the DGPS kinematic positioning in post process mode provides the position accuracy of ±10cm or better. The idea behind all

differential positioning is to eliminate bias portions at one location by comparing them with these seen at a known position. Therefore, it is essential to track the same set of satellites at both base and remote receivers. Furthermore, the accuracy in baseline determination is highly dependent on the baseline length.

In real-time DGPS, two correction methods are in use. The first method is to correct the position of the remote receiver using calculated and known position of the base station. The second method is based on the pseudorange corrections derived from the difference between calculated ranges and observed ranges at the base station. Thus, a fast radio link between the base and remote receiver is required in this case. In addition, the ambiguities must be resolved on-the-fly to use phase measurements for better accuracy.

In the post-processing, the relative position of the remote receiver $(\Delta x, \Delta y, \Delta z)$ is solved using the observations from both base and remote receivers instead of applying the corrections to the remote receiver. The most popular observables used in precise kinematic positioning is the double differencing (3.3) because of its compact structure and the rather simple (block diagonal) weight matrix. The constant errors caused by the common receivers and the common satellites are cancelled and the ambiguity remains as integer in this case. Because of the non-linearity between the observations and the unknowns, the equations (3.3) should be linearized to set up an adjustment model.

For simplicity, the adjustment model is derived with a simplified double differenced model neglecting the atmospheric effects. As a matter of fact, the ionospheric effect could be reduced using an ion-free combination and the tropospheric effect could be modeled and then removed prior to the adjustment. Thus, after understanding the basic simple adjustment equation, one can refine the various adjustment models depending on the purpose at hand. Neglecting the atmospheric effect, the double differenced observation equation for the phase measurements can be reduced as follows:

$$\begin{aligned} \Phi_{ij,1}^{kl} &= \rho_{ij}^{kl} + \lambda_1 N_{ij,1}^{kl} + \varepsilon_{ij,1}^{kl} \\ \Phi_{ij,2}^{kl} &= \rho_{ij}^{kl} + \lambda_2 N_{ij,2}^{kl} + \varepsilon_{ij,2}^{kl} \end{aligned}, \tag{3.6}$$

where the double differenced geometric range in above equations is expanded as:

$$\begin{aligned} \rho_{ij}^{kl} = &\sqrt{(x^k - x_i)^2 + (y^k - y_i)^2 + (z^k - z_i)^2} - \sqrt{(x^l - x_i)^2 + (y^l - y_i)^2 + (z^l - z_i)^2} \\ &- \sqrt{(x^k - x_j)^2 + (y^k - y_j)^2 + (z^k - z_j)^2} + \sqrt{(x^l - x_j)^2 + (y^k - y_i)^2 + (z^k - z_i)^2} \end{aligned} \tag{3.7}$$

Assuming the satellite positions and the base position (x_i, y_i, z_i) are known, the above equations (3.6) would be linearized in terms of the approximate remote receiver position (x_{j0}, y_{j0}, z_{j0}).

$$\begin{aligned} \Phi_{ij,1}^{kl} &= \rho_{ij0}^{kl} + d\rho_{ij0}^{kl} + \lambda_1 N_{ij,1}^{kl} + \varepsilon_{ij,1}^{kl} \\ \Phi_{ij,2}^{kl} &= \rho_{ij0}^{kl} + d\rho_{ij0}^{kl} + \lambda_2 N_{ij,2}^{kl} + \varepsilon_{ij,2}^{kl} \end{aligned}, \tag{3.8}$$

where

$$\rho_{ij0}^{kl} = \rho_i^k - \rho_i^l - \rho_{j0}^k + \rho_{j0}^l$$

$$d\rho_{ij}^{kl} = \left(\frac{x^k - x_{j0}}{\rho_{j0}^k} - \frac{x^l - x_{j0}}{\rho_{j0}^l}\right)dx_j + \left(\frac{y^k - y_{j0}}{\rho_{j0}^k} - \frac{y^l - y_{j0}}{\rho_{j0}^l}\right)dy_j + \left(\frac{z^k - z_{j0}}{\rho_{j0}^k} - \frac{z^l - z_{j0}}{\rho_{j0}^l}\right)dz_j \quad . \quad (3.9)$$

Rearranging (3.8) with (3.9), the usual adjustment model $y = A\xi + e,\ e \sim N(0, \Sigma)$ can be established. Assuming four satellites k, l, m and n are simultaneously tracked, the corresponding components in the adjustment model are:

$$y = \begin{bmatrix} \Phi_{ij,1}^{kl} - \rho_{ij0}^{kl} \\ \Phi_{ij,1}^{km} - \rho_{ij0}^{kl} \\ \Phi_{ij,1}^{kn} - \rho_{ij0}^{kl} \\ \Phi_{ij,2}^{kl} - \rho_{ij0}^{kl} \\ \Phi_{ij,2}^{km} - \rho_{ij0}^{kl} \\ \Phi_{ij,2}^{kn} - \rho_{ij0}^{kl} \end{bmatrix},\ A = \begin{bmatrix} \alpha_{xj}^{kl} & \alpha_{yj}^{kl} & \alpha_{zj}^{kl} & \lambda_1 & 0 & 0 & 0 & 0 & 0 \\ \alpha_{xj}^{km} & \alpha_{yj}^{km} & \alpha_{zj}^{km} & 0 & \lambda_1 & 0 & 0 & 0 & 0 \\ \alpha_{xj}^{kn} & \alpha_{yj}^{kn} & \alpha_{zj}^{kn} & 0 & 0 & \lambda_1 & 0 & 0 & 0 \\ \alpha_{xj}^{kl} & \alpha_{yj}^{kl} & \alpha_{zj}^{kl} & 0 & 0 & 0 & \lambda_2 & 0 & 0 \\ \alpha_{xj}^{km} & \alpha_{yj}^{km} & \alpha_{zj}^{km} & 0 & 0 & 0 & 0 & \lambda_2 & 0 \\ \alpha_{xj}^{kn} & \alpha_{yj}^{kn} & \alpha_{zj}^{kn} & 0 & 0 & 0 & 0 & 0 & \lambda_2 \end{bmatrix},\ \xi = \begin{bmatrix} dx_i \\ dy_j \\ dz_j \\ N_{ij,1}^{kl} \\ N_{ij,1}^{km} \\ N_{ij,1}^{kn} \\ N_{ij,2}^{kl} \\ N_{ij,2}^{km} \\ N_{ij,2}^{kn} \end{bmatrix}, \quad (3.10)$$

where

$$\alpha_{xj}^{kl} = \frac{x^k - x_{j0}}{\rho_{j0}^k} - \frac{x^l - x_{j0}}{\rho_{j0}^l}, \alpha_{yj}^{kl} = \frac{y^k - y_{j0}}{\rho_{j0}^k} - \frac{y^l - y_{j0}}{\rho_{j0}^l}, \alpha_{zj}^{kl} = \frac{z^k - z_{j0}}{\rho_{j0}^k} - \frac{z^l - z_{j0}}{\rho_{j0}^l}$$

$$\alpha_{xj}^{km} = \frac{x^k - x_{j0}}{\rho_{j0}^k} - \frac{x^m - x_{j0}}{\rho_{j0}^m}, \alpha_{yj}^{km} = \frac{y^k - y_{j0}}{\rho_{j0}^k} - \frac{y^m - y_{j0}}{\rho_{j0}^m}, \alpha_{zj}^{km} = \frac{z^k - z_{j0}}{\rho_{j0}^k} - \frac{z^m - z_{j0}}{\rho_{j0}^m}.$$

$$\alpha_{xj}^{kn} = \frac{x^k - x_{j0}}{\rho_{j0}^k} - \frac{x^n - x_{j0}}{\rho_{j0}^n}, \alpha_{yj}^{kn} = \frac{y^k - y_{j0}}{\rho_{j0}^k} - \frac{y^n - y_{j0}}{\rho_{j0}^n}, \alpha_{zj}^{kn} = \frac{z^k - z_{j0}}{\rho_{j0}^k} - \frac{z^n - z_{j0}}{\rho_{j0}^n}$$

The covariance matrix of the observations is obtained by applying the simple error propagation law. Consider two double differenced observation Φ_{ij}^{kl} and Φ_{ij}^{km}, and define DD as follows:

$$DD := \begin{bmatrix} \Phi_{ij}^{kl} \\ \Phi_{ij}^{km} \end{bmatrix} = F \cdot \Phi, \quad (3.11)$$

where $F = \begin{bmatrix} 1 & -1 & -1 & 1 & 0 & 0 \\ 1 & -1 & 0 & 0 & -1 & 1 \end{bmatrix}$, $\Phi = \begin{bmatrix} \Phi_i^k \\ \Phi_i^k \\ \Phi_i^k \\ \Phi_i^k \\ \Phi_i^k \\ \Phi_i^k \end{bmatrix}$.

Assuming no correlations among each observation in matrix Φ, the covariance of DD is calculated as

$$\begin{aligned} \mathrm{cov}(DD) &= F\,\mathrm{cov}(\Phi)F^T \\ &= \sigma^2 F \cdot F^T \\ &= \sigma^2 \begin{bmatrix} 4 & 2 \\ 2 & 4 \end{bmatrix} \end{aligned} \quad . \tag{3.12}$$

So, the double differenced observables are correlated because of the common satellites and receivers. It should be noted that the above model (3.10) is underdetermined because we have six observations and nine unknowns. Theoretically, the above system can be solved if the receiver could be stationary for one more epoch because each epoch adds six observations while the number of unknowns remain the same. Afterwards, the remote receiver can be in motion and its position can be determined.

If cycle slips or losses of lock occur while the receiver is moving, the ambiguity should be re-determined. The most popular methods in ambiguity fixing are the ambiguity function and the search technique. The former uses the concept of minimum variance of the estimated ambiguities and the latter uses the adjustment technique applied to trial positions in search space. For more details on ambiguity fixing, refer to Remondi (1991), Hwang (1991), etc.

3.4 Inertial Navigation System Overview

The Inertial Navigation System (INS) is a self-contained position and velocity measuring device using sensors which react on the basis of physical laws: Newton's law of motion and Sagnac effect for mechanical and modern ring laser gyro, respectively. Unlike other systems such as GPS, the INS depends entirely on electromagnetic instruments that do not require visual or radio link with the environment. The INS is mainly designed for the vehicles such as cars and ships, but also airplanes. So the fundamental function of the inertial navigation system is to indicate the position, velocity, heading, and direction of vertical over a period of time (Broxmeyer, 1964). In addition to the military applications, INS has been used in many scientific and engineering areas such as auto- navigation, flight control and survey.

The sensors of the INS comprising the Inertial Measurements Unit (IMU) consist of accelerometers and gyroscopes. The accelerometer senses acceleration, more precisely the specific force, and the gyroscope senses angular rate of a moving object for translational and rotational motion, respectively. Among various specific force measurements, measuring the variations of spring or pendulum with a proof mass is most commonly used for accelerometers.

Similarly, the reaction of a spinning proof mass is measured in the mechanical gyroscope. In case of the modern gyroscope, a property of light in a rotating frame, called Sagnac effect, is utilized instead of a spinning proof mass.

The role of gyroscope is to provide a reference frame for navigation. In other words, the accelerometer senses the acceleration in its own frame, while the sought

position is in a reference frame such as the navigation or inertial frame. Using the angular and orientation information from the gyroscopes, the position derived from the accelerometer could be transformed into the reference frame. Therefore, three single-degree-of-freedom (SDF) gyros are necessary with mutually perpendicular sensitive axes to determine the three-dimensional reference for attitude.

3.4.1 Mechanization

There are two types of mechanization of the IMU, namely the stabilized platform and the strapdown configuration. The stabilized platform provides angular motion isolation from the vehicle. In other words, the amount of rotation needed to isolate the platform from the vehicle motion is obtained from the output of gyros. Then, the stabilization is accomplished by rotating the platform back to the original position using the servo motor of the gimbal. Through this feedback, called space stabilization, gyros maintain a fixed orientation in the inertial space. Using the accelerometers mounted on the space-stabilized platform, the specific forces at a fixed orientation can be obtained. Because of the vehicle's motion isolation, the stabilized system usually shows better performance than the strapdown system.

In strapdown mode, the gyros and accelerometers are physically bolted to the vehicle. Therefore, those sensors are subjected to the entire range of dynamics of the vehicle. This means that, in general, the performance of the strapdown system is poorer than that of the local stabilized system. In addition, an extra computation is necessary to transform the data from the body to the navigation frame since the orientation of the platform is not maintained. The advantages of the strapdown system are lower cost, smaller size and lighter weight. Furthermore, the installation on a vehicle is much easier than that of the stabilized system.

3.4.2 Gyroscope

Two major types of gyros are in use, namely the mechanical gyro and the optical gyro. The modern Ring Laser Gyro (RLG) and Fiber Optic Gyro (FOG) are in the category of the optical gyro. As mentioned previously, the physical backgrounds of the mechanical gyro and modern RLG or FOG are totally different. While the mechanical gyro is based on the angular momentum conservation law and implemented in the stabilized system, RLG or FOG are based on the Sagnac effect and implemented in the strapdown system. In both cases, however, the role of the gyro providing a reference for relative attitude, or orientation, is the same. Since this study utilizes the strapdown system, the description on the mechanical gyro will not be discussed.

3.4.2.1 Sagnac Effect

The Sagnac effect describes the propagation of a light beam around a closed path in a frame that rotates with respect to the inertial frame. Because light should not be affected by the dynamics of the environment in which the gyro finds itself, it is the natural alternative to the spinning proof mass of the mechanical gyro for the strapdown system. When a light beam travels in a closed path that is rotating with respect to the inertial space, apparent lengthening or shortening of the path on which the light travels occurs. The lengthening occurs when the light travels in the same direction in which the path rotates and the shortening occurs in the opposite case.

Consider a light beam traversing an arbitrary circuitous planar path having length L in the counterclockwise direction as shown in Figure 3.2. After time t, the light left from the emitter E returned to the same inertial position E. The emitter, however, is not at the position anymore but at the position E' because it is rotating. To catch up with the emitter, the light must travel extra path (ΔL) during extra time Δt. Therefore, one can set up a relationship between the rotation of the path and the apparent lengthening/shortening.

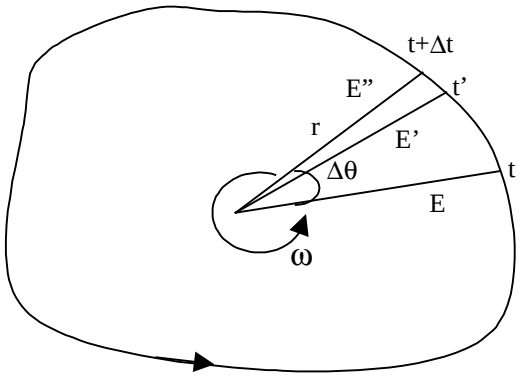

Figure 3.2 The Sagnac effect showing apparent path lengthening.

The differential change in path during a differential time interval dt is given by

$$dt = \frac{r \cdot d\theta}{c} \tag{3.13}$$

In the mean time, the circuit rotates by

$$d(\Delta L) = r \cdot \omega \cdot dt \tag{3.14}$$

Notice that the total apparent lengthening of the path occurs while the light travels a total angle of $2\pi + \Delta\theta$. Also, the integration variable can be changed from angle to area, A, swept out by the light wave using the following relationship:

$$dA = \frac{1}{2} \cdot r \cdot r d\theta \tag{3.15}$$

Substituting (3.13) in to (3.14) and then changing the integration variable using (3.15), one can derive the apparent lengthening as

$$\Delta L = \frac{2\omega}{c} A \,, \tag{3.16}$$

where c is the light velocity and ω is the angular rate of the path with respect to the inertial space.

In the opposite case, that is, the light travels in the opposite direction to that of the path, the apparent shortening (Δl) occurs as

$$\Delta l = -\frac{2\omega}{c} A \tag{3.17}$$

3.4.2.2 Ring Laser Gyro

As one can see in (3.16) and (3.17), it is very difficult to detect the rotation by measuring the change of the wavelength of light. For example, the apparent path lengthening caused by the rotation of $2\pi\,\mathrm{rad/sec}$ of a circuit defined by a circle with radius equal to 10 cm is just $\Delta L \approx 1.3 \cdot 10^{-9}\,\mathrm{m}$. Instead, the RLG uses a fringe pattern of two counter-traversing light beams to detect the rotation of the platform. As shown in Figure 3.3, two light beams traversing in opposite direction are generated by a gas discharge in the resonant cavity of a laser. The resonant cavity is built such a way that the optical path length for each beam and frequencies of two beams are identical when gyro is at rest. When the gyro is rotating about an axis perpendicular to the lasing plane, one beam shows apparent path lengthening, and the other shortening.

Consider a laser with wavelength λ and the integer number N, inside a resonant cavity of length L.

$$L = N\lambda \tag{3.18}$$

The change in apparent length of the resonant cavity implies the change in the wavelength:

$$\Delta L = N\Delta\lambda \,. \tag{3.19}$$

Using $f = c/\lambda$, change in the wavelength can be converted to the change in the frequency:

$$\Delta f = -\frac{f}{L}\Delta L \,. \tag{3.20}$$

From (3.20), (3.16) and (3.17), one can derive the relationship between the angular rate of the rotation and the difference in the frequencies of the two counter-travelling light beams.

$$\delta f = \frac{4}{\lambda}\frac{A}{L}\omega \tag{3.21}$$

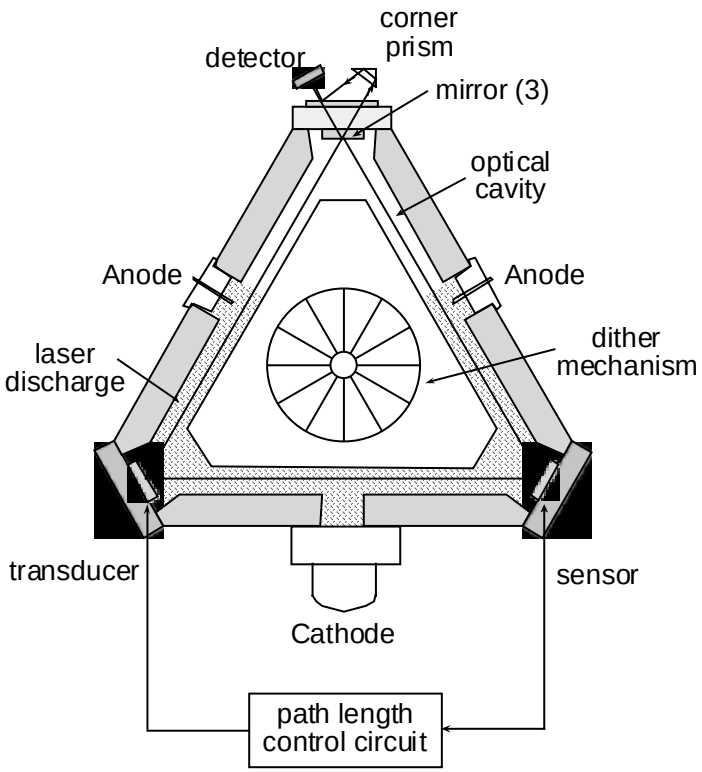

Figure 3.3 Schematic of three-mirror ring laser gyro (Honeywell H-423).

Finally, the relationship between the phase difference and the change in angle is obtained by integrating the above equation.

$$\delta\phi = \int \delta f \, dt = \frac{4A}{\lambda L}\delta\theta \tag{3.22}$$

The phase change is measured by detecting the transitions from light to dark in the fringe pattern. The fringe pattern remains stationary if there is no rotation with respect to the inertial space. In the presence of rotation, however, the fringe pattern migrates and the number of the fringes passing a detector indicates the rate of rotation.

The problem in RLG is so-called frequency lock-in. From imperfections in the various components of the resonant cavity, the two counter-traversing beams oscillate at nearly the same frequency and lock together at the same frequency over a range of low angular rates. In this case, the RLG does not recognize the rotation and produces zero rotation.

To overcome the lock-in problem, an artificial bias can be imposed in the sensed angular rate by generating the deliberate asymmetries into the device. Then, the true rate is obtained by correcting the known effect of the designed asymmetry. There are two main approaches introducing the asymmetries, namely using mechanical motion

and magnetic fields. In the first case, an artificial bias in the form of an alternating rotation (dithering) of the gyro about the sensitive axis is imposed. This means, however, that the gyro has to pass the lock-in range twice per dither period. Therefore, the gyro will not sense the actual rotation for a small amount of time and this causes an error that can be modeled as a random walk. In the second case, so-called Faraday cell is placed in the path of the light beams so that a frequency bias between two beams is created by the polarization effect in the cell. The bias modulated by the switching the magnetic field is periodic, but the time in the lock-in range is extremely short because it corresponds to the switching time of the magnetic field. One of the successful implementation of the magnetic asymmetries could be found in the Litton's "zero-lock" RLG which uses four light beams to create two laser gyros in the same cavity. It uses two sets of oppositely polarized beam pairs so that the Faraday bias can be cancelled while the signal is doubled.

The output of the strapdown gyro is the angular rate of the platform, or body, on which the gyro is installed, with respect to the inertial space represented in the b-frame ω_{ib}^{b}. The essential error model for the RLG is given by three components: drift error, scale factor error, and random noise.

$$\delta\omega^{b} = \mathbf{b}_{g} + \mathbf{k}_{g}\omega + \varepsilon_{g} \tag{3.23}$$

The scale factor error includes a constant part and linearly varying parts. The drift bias includes a constant part, effects of the misalignment, and temperature and magnetic sensitivity terms.

3.4.3 Accelerometer

The primitive form of the accelerometer can be well described using the spring-mass combination. Although details of the construction are not the same, all accelerometers operate more or less on the basis of similar principles.

In a modern accelerometer, the degree of freedom of the proof mass is pendulous rather than translational as in the spring-mass combination. As shown in Figure 3.4, there are three axes associated with the accelerometer: input axis (1-axis), output axis (2-axis) and the pendulous reference axis (3-axis) related to the proof mass. The proof mass is the arm of the pendulum hinged to the case so that the applied acceleration is measured from a rotation about the hinged point.

When a specific force is applied along the 1-axis, the pendulous axis will deviate from the reference axis. The rotation occurs around the 2-axis and sensed by the signal generator (SG) at one end that creates a corresponding torque to the torque generator (TG) at the other end to null out the rotation.

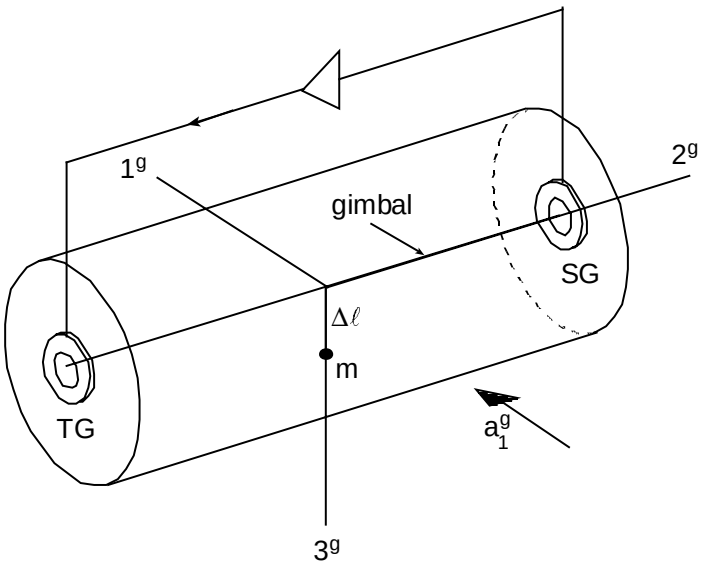

Figure 3.4 Schematic of torque rebalance pendulous accelerometer.

Figure 3.5 shows the cross-section of the QA2000 accelerometer integrated in Honeywell's LaserRef III RLG inertial navigator. The torquer coil/seismic element is supported by the quartz-flexure suspension. When the seismic mass responds to an applied specific force, the capacitor plates generate corresponding ac output voltage. This signal is fed back to the torquer coil, producing an electromagnetic torque to nullify the effects of the sensed acceleration. The feedback current for this counterbalancing is the measurement of the input acceleration.

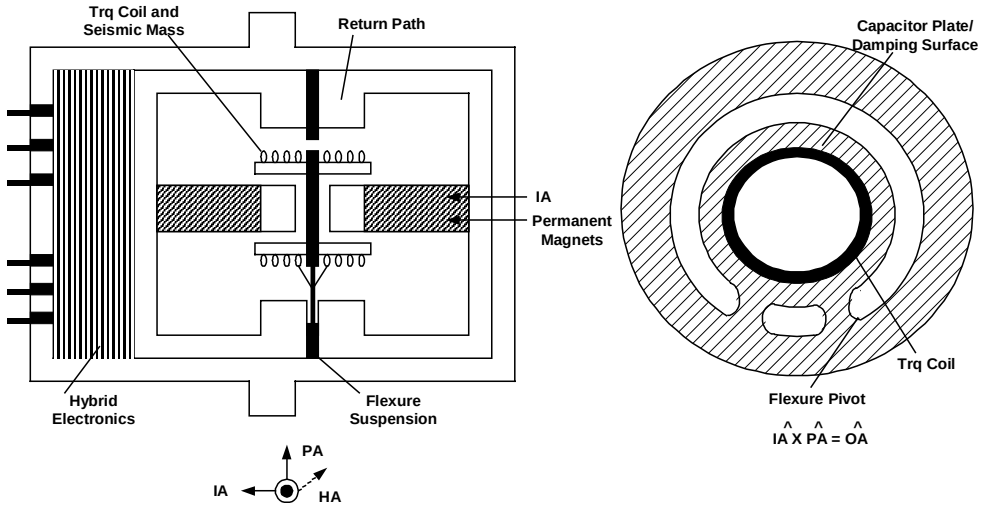

Figure 3.5 QA2000 Accelerometer

The errors affecting the accelerometer measurements are very similar to those for the mechanical gyro. The general model includes a general bias, a scale factor error and the random noise terms.

$$\delta\mathbf{a}^b = \mathbf{b}_a + \mathbf{k}_a\mathbf{a}^b + \varepsilon_a, \tag{3.24}$$

where $\delta\mathbf{a}^b$ is the total error in the body frame, $\mathbf{b}_a$ is the general bias, $\mathbf{k}_a$ is the scale factor error and ε_a is the random noise. In spite of its name, $\mathbf{b}_a$ is considered random.

The general bias term includes unknown constant and anisoelasticity effect due to unequal compliance in the pivots of the pendulum. The scale factor error consists of constant, linear and quadratic dependencies on the input acceleration, and effects generated in the torque rebalance electronics. There is another error, the misalignment error, caused by the offset between the reference axes and the axes of the case. Through calibration, careful design and mechanization, this effect could be significantly reduced or minimized.

3.4.4 Navigation Equation

The output from the a strapdown INS system consists of the inertial acceleration in the body frame $(\mathbf{a}^b)$ and the angular rate of the body frame with respect to the inertial frame (ω_{ib}^b). Therefore, this sensed acceleration should be converted to the n-frame inertial acceleration to be used in the navigation equation. The transformation from the i- to n-frame can be done using gyro data. Then, those accelerations in the n-frame must be integrated to get the position and velocity of a vehicle through the navigation equation.

The fundamental equation (2.6) that modified Newton's Second Law of motion under the existence of the gravitational field, from which the navigation equation is derived, is rewritten for convenience as:

$$\ddot{\mathbf{x}}^i = \mathbf{a}^i + \mathbf{g}^i. \tag{3.25}$$

It states that the kinematic acceleration is the sum of both specific force and gravitation in the inertial frame. Applying the transformation matrix from i- to n-frame:

$$\mathbf{a}^n = C_i^n\mathbf{a}^i = C_i^n(\ddot{\mathbf{x}}^i - \mathbf{g}^i) = C_i^n\ddot{\mathbf{x}}^i - \mathbf{g}^n. \tag{3.26}$$

Now, let $\mathbf{v}^n$ be the e-frame velocity vector coordinatized in the n-frame. Then, from the Coriolis law:

$$\mathbf{v}^n = C_e^n\dot{\mathbf{x}}^e = C_e^nC_i^e(\dot{\mathbf{x}}^i + \Omega_{ei}^i\mathbf{x}^i). \tag{3.27}$$

Solving for $\dot{\mathbf{x}}^i$,

$$\dot{\mathbf{x}}^i = C_n^i\mathbf{v}^n - \Omega_{ei}^i\mathbf{x}^i. \tag{3.28}$$

The time derivative of (3.27) yields

$$\frac{d}{dt}\mathbf{v}^n = \dot{C}_i^n(\dot{\mathbf{x}}^i + \Omega_{ei}^i\mathbf{x}^i) + C_i^n(\ddot{\mathbf{x}}^i + \Omega_{ei}^i\dot{\mathbf{x}}^i). \tag{3.29}$$

Substituting (3.27) and (3.28) into (3.29) and using the differential equation for the transformation (2.46):

$$\frac{d}{dt}\mathbf{v}^n = C_i^n\left(\ddot{\mathbf{x}}^i + (\Omega_{ni}^i + \Omega_{ei}^i)C_n^i\mathbf{v}^n - \Omega_{ei}^i\Omega_{ei}^i\mathbf{x}^i\right). \tag{3.30}$$

Finally, use (2.16) and substitute (3.26) into (3.30):

$$\frac{d}{dt}\mathbf{v}^n = \mathbf{a}^n - (\Omega_{in}^n + \Omega_{ie}^n)\mathbf{v}^n + \bar{\mathbf{g}}^n, \tag{3.31}$$

where $\bar{\mathbf{g}}^n = \mathbf{g}^n - \Omega_{ie}^n\Omega_{ie}^n\mathbf{x}^n$ is the gravity vector being the sum of gravitational and centrifugal acceleration of the Earth.

Using the relationship between the velocity in the n-frame and the e-frame represented by the geodetic latitude, longitude and height,

$$\mathbf{v}^n = \begin{pmatrix} \dot{\phi}(M+h) \\ \dot{\lambda}(N+h)\cos\phi \\ -\dot{h} \end{pmatrix}, \tag{3.32}$$

and substituting the angular rate matrices in (3.31) explicitly, one can derive six differential equations as:

$$\frac{d}{dt}\begin{pmatrix} v_N \\ v_E \\ v_D \\ \phi \\ \lambda \\ h \end{pmatrix} = \begin{pmatrix} a_N + \bar{g}_N - 2\omega_e\sin\phi v_E + \dot{\phi}v_D - \dot{\lambda}\sin\phi v_E \\ a_E + \bar{g}_E - 2\omega_e\sin\phi v_N + 2\omega_e\cos\phi v_D + \dot{\lambda}\sin\phi v_N + \dot{\lambda}\cos\phi v_D \\ a_D + \bar{g}_D - 2\omega_e\cos\phi v_E - \dot{\lambda}\cos\phi v_E - \dot{\phi}v_N \\ \dfrac{v_N}{M+h} \\ \dfrac{v_E}{(N+h)\cos\phi} \\ -v_D \end{pmatrix}. \tag{3.33}$$

These are the navigation equations which need be integrated to get Earth-referenced position and velocity, coordinatized in the n-frame. Note that horizontal gravity values are needed for the north and east components.

As mentioned at the beginning, the outputs from the strapdown IMU must be transformed into the navigation frame. Basically, the acceleration in the body frame can be transformed into the n-frame through the transformation.

$$\mathbf{a}^n = C_b^n\mathbf{a}^b \tag{3.34}$$

Here, the transformation C_b^n can be obtained from the angular rate ω_{nb}^b derived as follows:

$$\omega_{nb}^b = \omega_{ni}^b + \omega_{ib}^b = \omega_{ib}^b - C_n^b\omega_{in}^n. \tag{3.35}$$

The angular rate ω_{ib}^b can be obtained from gyro, and ω_{in}^n is given in formula (2.64) that needs the position and the velocity of the vehicle for evaluation. Note that (2.66) should be integrated to get the transformation C_b^n. The initial conditions for (2.66) involve the initialization procedure of INS.

3.4.5 Initialization and Alignment

Briefly speaking, the initialization is used to determine various initial conditions, to define the navigation frame and resolve error sources. The position and velocity in the inertial navigation is obtained by integrating the acceleration. Thus, the initial conditions are associated with those integration constants and must be supplied by external sources. Furthermore, the initialization of the INS includes the initial alignment of the inertial sensors. This initial direction cosine matrix between the b- and n-frame serves as the starting point for the gyro angle integration (2.66). The effect of misalignment, or initial orientation error, appears as a global trend and will be discussed in detail in Chapter 5 through a simulation.

In the broad sense, the initial alignment also includes the determination of the systematic errors of the IMU. Because errors like the accelerometer bias may change from turn-on to turn-on, they cannot be corrected through a lab calibration procedure. Usually, the initialization takes place while the vehicle is at rest. A priori information on the position and velocity are inserted into the system and used for the initialization and error determination. If the vehicle is moving, an external source of position and/or velocity required, for example GPS, to aid the INS.

One of the most difficult parts in the initialization is to determine the heading. The reason for this is that the vertical orientation error is just weakly coupled to the velocities.

CHAPTER 4

TRADITIONAL AIRBORNE GRAVIMETRY WITH POSITION UPDATE

4.1 Introduction

A schematic diagram for the traditional GPS/INS gravimetry is shown in Figure 4.1. The term 'traditional' is used for this approach because many previous studies on the GPS/INS airborne gravimetry utilized GPS positions/velocities as an external source for estimating the INS systematic errors as well as the gravity disturbances.

There are three procedures involved in the traditional method. First, the raw data from the IMU, $\delta\mathbf{v}, \delta\theta$, are integrated to get the INS positions through the navigation equations. Secondly, the phase data of the GPS are processed to get the GPS positions. Usually, double differencing is used for the reasons explained in Chapter 3. Finally, the INS systematic errors and the gravity disturbances are estimated through the Kalman filter using the GPS position/velocity updates. Here, the INS errors as well as the gravity disturbance are modeled as stochastic processes, and assigned as unknown parameters in the Kalman filter derived from the error dynamics equations.

The primary concerns in the traditional approach consist of two parts: the derivation of the error dynamics equations, and stochastic modeling for the gravity disturbances. Because of the various IMU errors, the indicated positions or velocities of the INS deviate from the true values. The behavior or effects of the IMU errors can be analyzed by investigating the error dynamics equations. Using those equations, the propagation of errors from the sensors to the navigation solution can be identified and analyzed.

The error dynamics equations contain the gravity disturbance terms as one of the errors which should be either modeled or known to estimate the IMU errors. One of the practical ways to model the gravity field is as a stochastic process. Although there are arguments on modeling the gravity field, it is still a good approach in practical gravity determination (Wang, 1997).

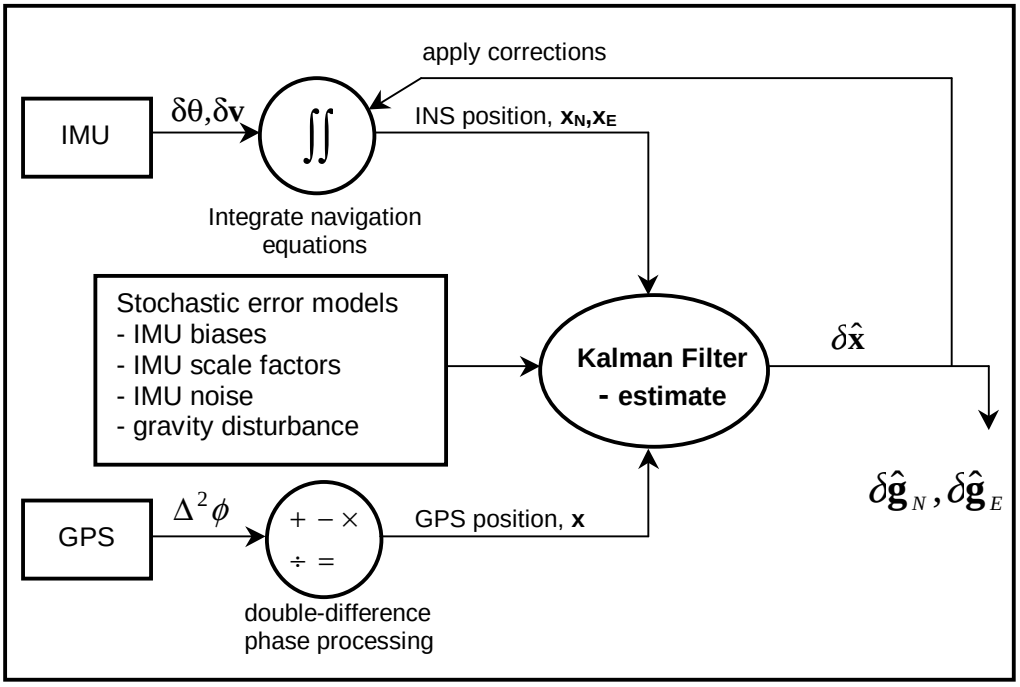

Figure 4.1 Schematic diagram for the traditional GPS/INS gravimetry.

In this chapter, the error dynamics equations of the navigation equation will be derived first. After briefly investigating the stochastic modeling of the IMU errors and gravity disturbances, the estimation of gravity disturbances using real flight data are presented. The analysis of the results closes this chapter.

4.2 Error Dynamics Equations in n-frame

The error dynamics equations of the INS can be obtained by simply applying the differential operator, δ, to the navigation equations (3.31). Here, the differential operator implies making the small changes or perturbations of the values. It is the linear part of an analytic expansion into Taylor's series, and the higher order terms are assumed to be negligible. After applying the differential operator to the navigation equation, they have to be explicitly expressed in terms of the geodetic coordinates to derive the n-frame error dynamics equations.

The linear perturbation of formula (3.31) is

$$\frac{\mathrm{d}}{\mathrm{dt}}\delta\mathbf{v}^{\mathrm{n}} = -\delta(\Omega_{\mathrm{in}}^{\mathrm{n}} + \Omega_{\mathrm{ie}}^{\mathrm{n}})\mathbf{v}^{\mathrm{n}} - (\Omega_{\mathrm{in}}^{\mathrm{n}} + \Omega_{\mathrm{ie}}^{\mathrm{n}})\delta\mathbf{v}^{\mathrm{n}} + \delta\mathbf{a}^{\mathrm{n}} + \overline{\Gamma}^{\mathrm{n}}\delta\mathbf{p}^{\mathrm{n}} + \delta\overline{\mathbf{g}}^{\mathrm{n}}, \tag{4.1}$$

where $\overline{\Gamma}^{\mathrm{n}} = \partial\mathbf{g}^{\mathrm{n}} / \partial\mathbf{p}^{\mathrm{n}}$ is the second-order tensor of partial derivatives of the gravity vector with respect to the coordinates, and $\delta\mathbf{p}^{\mathrm{n}}$ is a vector of differentials along the

axes of the n-frame.

$$\delta \mathbf{p}^n = \begin{pmatrix} (M+h)\delta\phi \\ (N+h)\cos\phi\,\delta\lambda \\ -\delta h \end{pmatrix} \tag{4.2}$$

Note that the perturbation $\delta \mathbf{a}^n$ is the error of the sensed acceleration in the n-frame.

Because the frame of the accelerometer is assumed to be parallel to the b-frame, the accelerometer errors in the b-frame should be transformed to the n-frame. The transformation, however, also contains errors because it is determined by the output from the gyro. Therefore, the dynamics of the errors in the orientation of the b-frame with respect to the n-frame should be considered as well.

Now, let us define the orientation error as:

$$\psi^n = (\psi_1^n, \psi_2^n, \psi_3^n)^T, \quad \Psi^n = \begin{pmatrix} 0 & -\psi_3^n & \psi_2^n \\ \psi_3^n & 0 & -\psi_1^n \\ -\psi_2^n & \psi_1^n & 0 \end{pmatrix} \tag{4.3}$$

Then, the matrix Ψ^n describes the orientation error in the form of a small rotation between the true n-frame and the computed n-frame. Denoting the true transformation as C_b^n and erroneously computed transformation as $\hat{C}_b^n$, the relationship between them is given as:

$$\hat{C}_b^n = (I - \Psi^n) C_b^n \tag{4.4}$$

Then, the error in the transformation is given by

$$\delta C_b^n = \hat{C}_b^n - C_b^n = -\Psi^n C_b^n \tag{4.5}$$

Now, the perturbation of acceleration in the n-frame can be computed as follows:

$$\begin{aligned} \delta \mathbf{a}^n &= C_b^n \delta \mathbf{a}^b + \delta C_b^n \mathbf{a}^b \\ &= C_b^n \delta \mathbf{a}^b - \Psi^n C_b^n \mathbf{a}^b . \\ &= C_b^n \delta \mathbf{a}^b + \mathbf{a}^n \times \psi^n \end{aligned} \tag{4.6}$$

Note that the acceleration error in the n-frame includes the orientation error as well as the acceleration error in the b-frame.

The dynamic behavior of the error angle can be derived by differentiating the equation (4.5).

$$\begin{aligned} \delta \dot{C}_b^n &= \delta(C_b^n \Omega_{nb}^b) = \delta C_b^n \Omega_{nb}^b + C_b^n \delta \Omega_{nb}^b \\ &= -\dot{\Psi}^n C_b^n - \Psi^n C_b^n \Omega_{nb}^b \end{aligned} \tag{4.7}$$

Substituting (4.5) into the second equation of (4.7) and solving for $\dot{\Psi}^n$ yields

$$\dot{\Psi}^n = -C_b^n \delta \Omega_{nb}^b C_n^b, \qquad \dot{\psi}^n = -C_b^n \delta \omega_{nb}^b, \tag{4.8}$$

where $\delta \omega_{nb}^b$ is the error in the rotation rate of the b-frame with respect to the n-frame. To derive the equation for the error $\delta \omega_{nb}^b$, the output of the gyro is divided into two terms, namely the rotation of the n-frame with respect to the i-frame and that of the b-frame with respect to the n-frame.

$$\omega_{ib}^{b} = \omega_{in}^{b} + \omega_{nb}^{b} \tag{4.9}$$

Perturbing the above equation and using $\omega_{in}^{b} = C_{n}^{b}\omega_{in}^{n}$,

$$\begin{aligned} \delta\omega_{ib}^{b} &= \delta C_{n}^{b}\omega_{in}^{n} + C_{n}^{b}\delta\omega_{in}^{n} + \delta\omega_{nb}^{b} \\ &= C_{n}^{b}\Psi^{n}\omega_{in}^{n} + C_{n}^{b}\delta\omega_{in}^{n} + \delta\omega_{nb}^{b} \end{aligned}, \tag{4.10}$$

where $\delta\omega_{in}^{n} = \begin{pmatrix} \delta\dot{\lambda}\cos\phi - (\dot{\lambda}+\omega_{e})\delta\phi\sin\phi \\ -\delta\dot{\phi} \\ -\delta\dot{\lambda}\sin\phi - (\dot{\lambda}+\omega_{e})\delta\phi\cos\phi \end{pmatrix}$ is the error in the angular rate of the n-frame with respect to the i-frame.

Finally, solving for $\delta\omega_{nb}^{b}$ and substituting it into (4.8) yields the dynamic equation for the angles in the transformation from the b-frame to the n-frame:

$$\dot{\psi}^{n} = -\omega_{in}^{n} \times \psi^{n} - C_{b}^{n}\delta\omega_{ib}^{b} + \delta\omega_{in}^{n}. \tag{4.11}$$

Now, using (3.32), one can derive the differentials and dynamic behavior of the velocity errors as follows:

$$\delta\mathbf{v}^{n} = \begin{pmatrix} (\delta M+\delta h)\dot{\phi} + (M+h)\delta\dot{\phi} \\ (\delta N+\delta h)\cos\phi\dot{\lambda} + (N+h)(\cos\phi\delta\dot{\lambda} - \sin\phi\dot{\lambda}\delta\phi) \\ -\delta\dot{h} \end{pmatrix} \tag{4.12}$$

$$\frac{d}{dt}\delta\mathbf{v}^{n} = \begin{pmatrix} (\delta\dot{M}+\delta\dot{h})\dot{\phi} + (\dot{M}+\dot{h})\delta\dot{\phi} + (\delta M+\delta h)\ddot{\phi} + (M+h)\delta\ddot{\phi} \\ (\delta\dot{N}+\delta\dot{h})\dot{\lambda}\cos\phi + (\dot{N}+\dot{h})(\delta\dot{\lambda}\cos\phi - \dot{\lambda}\delta\phi\sin\phi) + (\delta N+\delta h)(\ddot{\lambda}\cos\phi - \dot{\lambda}\dot{\phi}\sin\phi) \\ +(N+h)\left((\delta\ddot{\lambda} - \dot{\lambda}\dot{\phi}\delta\phi)\cos\phi - (\ddot{\lambda}\delta\phi + \delta\dot{\lambda}\dot{\phi} + \dot{\lambda}\delta\dot{\phi})\sin\phi\right) \\ -\delta\ddot{h} \end{pmatrix} \tag{4.13}$$

In above equation, the terms involving $\delta N, \delta M, \dot{N}, \dot{M}, \delta\dot{N}$, and $\delta\dot{M}$ are all second-order terms so that those can be neglected in our linear approximation. In addition, the principal radii of curvature, N and M can be replaced with the Gaussian mean radius, $R = \sqrt{NM}$, to the first-order approximation.

Then, the equation (4.12) and (4.13) can be simplified as:

$$\delta\mathbf{v}^{n} = \begin{pmatrix} \delta h\dot{\phi} + (R+h)\delta\dot{\phi} \\ \delta h\cos\phi\dot{\lambda} + (R+h)(\cos\phi\delta\dot{\lambda} - \sin\phi\dot{\lambda}\delta\phi) \\ -\delta\dot{h} \end{pmatrix} \tag{4.14}$$

$$\frac{d}{dt}\delta\mathbf{v}^{n} = \begin{pmatrix} \delta\dot{h}\dot{\phi} + \dot{h}\delta\dot{\phi} + \delta h\ddot{\phi} + (R+h)\delta\ddot{\phi} \\ \delta\dot{h}\dot{\lambda}\cos\phi + \dot{h}(\delta\dot{\lambda}\cos\phi - \dot{\lambda}\delta\phi\sin\phi) + \delta h(\ddot{\lambda}\cos\phi - \dot{\lambda}\dot{\phi}\sin\phi) \\ +(R+h)\left((\delta\ddot{\lambda} - \dot{\lambda}\dot{\phi}\delta\phi)\cos\phi - (\ddot{\lambda}\delta\phi + \delta\dot{\lambda}\dot{\phi} + \dot{\lambda}\delta\dot{\phi})\sin\phi\right) \\ -\delta\ddot{h} \end{pmatrix} \tag{4.15}$$

Using equation (2.56) and (2.64), the first perturbation term in (4.1) can be derived in terms of the geodetic coordinates as follows:

$$\delta(\Omega_{in}^{n}+\Omega_{ie}^{n})$$
$$=\begin{pmatrix} 0 & \delta\dot{\lambda}\sin\phi+(\dot{\lambda}+2\omega_e)\cos\phi\delta\phi & -\delta\dot{\phi} \\ -\delta\dot{\lambda}\sin\phi-(\dot{\lambda}+2\omega_e)\cos\phi\delta\phi & 0 & -\delta\dot{\lambda}\cos\phi+(\dot{\lambda}+2\omega_e)\sin\phi\delta\phi \\ \delta\dot{\phi} & \delta\dot{\lambda}\cos\phi-(\dot{\lambda}+2\omega_e)\sin\phi\delta\phi & 0 \end{pmatrix} \quad (4.16)$$

Now, based on all the developments above, one can derive linear dynamic error equations in terms of the position, velocity and orientation. The usual form of the linear dynamic model is given as the first order differential equation as follows:

$$\frac{d}{dt}\varepsilon^{n} = F^{n}\varepsilon^{n} + G^{n}\mathbf{u}, \quad (4.17)$$

In our case, the parameter vector is given as:

$$\varepsilon^{n} = (\psi_1^{n}\ \psi_2^{n}\ \psi_3^{n}\ \delta\dot{\phi}\ \delta\dot{\lambda}\ \delta\dot{h}\ \delta\phi\ \delta\lambda\ \delta h)^{T}. \quad (4.18)$$

In addition, consider the vector of system errors composed of errors in angular rate, in acceleration and in gravity:

$$\mathbf{u} = \begin{pmatrix} \delta\omega_{ib}^{b} \\ \delta\mathbf{a}^{b} \\ \delta\mathbf{g}^{n} \end{pmatrix}. \quad (4.19)$$

With $r = R + h$, $\dot{l}_1 = \dot{\lambda} + \omega_e$, and $\dot{l}_2 = \dot{\lambda} + 2\omega_e$, each matrix in (4.17) can be derived in terms of the geodetic coordinates in the n-frame. It should be noted that the systematic errors from IMU's and gravity can be included in the set of system states with proper stochastic modeling. For the explicit representation of the elements in (4.17) augmented by the parameters, the stochastic modeling should be discussed in detail.

4.3 Stochastic Modeling for System Errors and Gravity Disturbance

To complete the dynamic error equations discussed in the previous section, the system errors as well as the gravity disturbance should be identified and modeled. All data from physical instruments and sensors contain random errors, and the data cannot be fully described in a deterministic sense. In this case, the description may be put in probabilistic terms with reasonable models that sufficiently describe the behavior of the observed system. Here, the choice of the model depends on the type of the instrumental or the sensor errors.

Because of the dependencies on time, the errors in the IMU are usually modeled as random or stochastic processes. A stochastic (random) process is defined as a collection, or ensemble, of random variables associated with a deterministic parameter such as a time or space coordinate. At each point in time or in space, the process is a random variable and the probabilistic property of the process, in general, changes in time or space.

In many cases, the first and second-order joint distribution or density functions are enough to characterize a stochastic process. The characterization is usually given by two functions, using the second moments of the probabilistic distributions, called

auto-covariance and cross-covariance functions. The auto-covariance function is defined as

$$\varphi_{x,x}(t_1,t_2) = E\left[x(t_1)x(t_2)\right] = \int_{-\infty}^{\infty} dx_1 \int_{-\infty}^{\infty} dx_2\,(x_1 - E\{x_1\})(x_2 - E\{x_2\})\,f(x_1,t_1;x_2,t_2) \quad (4.20)$$

where $x(t_1)$, $x(t_2)$ are the realizations (observed values) of the random process x at time t_1 and t_2; x_1, x_2 are the random variable x at time t_1 and t_2; $f(x_1,t_1;x_2,t_2)$ is the second-order joint probability density function of the random variable x_1 and x_2 given as:

$$f(x_1,t_1;x_2,t_2) = \frac{\partial^2 F(x_1,t_1;x_2,t_2)}{\partial x_1 \partial x_2}, \quad (4.21)$$

where $F(x_1,t_1;x_2,t_2) = \Pr\left[(x(t_1) \le x_1 \text{ and } x(t_2) \le x_2\right]$ is the corresponding joint probability distribution function.

The cross-covariance function is similarly defined as

$$\varphi_{x,y}(t_1,t_2) = E\left[x(t_1)y(t_2)\right] = \int_{-\infty}^{\infty} dx \int_{-\infty}^{\infty} dy\,(x - E\{x\})(y - E\{y\})\,f(x,t_1;y,t_2), \quad (4.22)$$

where $x(t_1)$, $y(t_2)$ are the realizations (observed values) of the random process x and y at time t_1 and t_2, respectively; $f(x,t_1;y,t_2)$ is the second-order joint probability density function of the random variable x and y:

$$f(x,t_1;y,t_2) = \frac{\partial^2 F(x,t_1;y,t_2)}{\partial x \partial y}, \quad (4.23)$$

where $F(x,t_1;y,t_2) = \Pr\left[(x(t_1) \le x \text{ and } y(t_2) \le y\right]$ is the corresponding joint probability distribution function.

Of course, the most easily modeled process is the stationary process whose probabilities do not change in time or under parallel shift in space. The joint probability density function for any set of random variables of a stationary process corresponding to any set of time coordinates is independent of the time origin. Furthermore, the stationary process is said to be time-invariant; if and only if the mean value and the variance of the random variable x_k at any time k are the same, and the second-order probability density function does not depend on the time origin but depends on the time interval $\tau = t_2 - t_1$. Thus, the covariance functions are functions of the single variable τ.

$$\varphi_{x,x}(\tau) = E\left[x(t_1)x(t_1+\tau)\right] \quad (4.24)$$

$$\varphi_{x,y}(\tau) = E\left[x(t_1)y(t_1+\tau)\right] \quad (4.25)$$

Some useful properties of these covariance functions for the stationary processes are:

$$\varphi_{xx}(0) = E\left[x^2\right] - [E\{x\}]^2 \quad (4.26)$$

$$\varphi_{xx}(-\tau) = \varphi_{xx}(\tau), \qquad \varphi_{xy}(-\tau) = \varphi_{yx}(\tau) \quad (4.27)$$

$$\varphi_{xx}(0) \ge \left|\varphi_{xx}(\tau)\right| \quad (4.28)$$

An important concept associated with stationary random processes is the ergodic hypothesis stating that any statistics calculated by averaging over all members

of an ergodic ensemble at a fixed time can also be calculated by averaging over all time of a single representation member of the ensemble. Briefly speaking, it means that the stochastic properties of the ergodic process can be analyzed from the temporal behavior of one single realization. It should be noted that not all stationary processes are ergodic. A typical example for this case is the ensemble of functions that are constant in time. The common statistics associated with an ergodic process are:

$$E[x] = \lim_{T\to\infty} \frac{1}{2T} \int_{-T}^{T} x(t)dt \tag{4.29}$$

$$E[x^2] = \lim_{T\to\infty} \frac{1}{2T} \int_{-T}^{T} x^2(t)dt \tag{4.30}$$

$$\varphi_{xx}(\tau) = \lim_{T\to\infty} \frac{1}{2T} \int_{-T}^{T} x(t)x(t+\tau)dt - [E\{x\}]^2 \tag{4.31}$$

$$\varphi_{xy}(\tau) = \lim_{T\to\infty} \frac{1}{2T} \int_{-T}^{T} x(t)y(t+\tau)dt - E\{x\}E\{y\} \tag{4.32}$$

4.3.1 System Error for the IMU

As any other physical instruments, gyros and accelerometers also contain system errors represented by specific force errors and angular rate errors, respectively. In general, both gyro and accelerometer measurements are affected by general biases, scale factor errors and white noise, although the detailed error models for inertial navigation sensors depend on the particular instrument design. For measurements from accelerometers, non-orthogonality of the axes, second-order scale non-linearity, and correlated noise could be considered in extended error models (Wei and Schwarz, 1994). The extended models for the gyros could also include the non-orthogonality of the axes and correlated noise.

The major error sources of gyro and accelerometer measurements are those basic common elements (biases, scale factor errors and white noise). Since other error sources are not large relative to the basic elements, they are neglected in this study for simplicity (see equations (3.23), (3.24)). Clearly, the effects of the general biases of the accelerometer and the gyro appear as long-term trends while the effect of the scale factor error appears as short-term variations. The quantitative effect of each error parameters is given in Chapter 5 through acceleration simulations.

The necessary concepts to describe the basic elements of the IMU errors in the stochastic modeling are random constant and white noise. Continuous white noise, $\Omega(t)$, is defined to be a stationary random process having a constant spectral density function over all frequencies (Brown and Hwang, 1992, p. 99). The auto-covariance function of the white noise is given by:

$$\varphi_{\Omega}(\tau) = q\delta(\tau), \tag{4.33}$$

where q is a constant and the delta function is defined as:

$$\delta(t-\tau)=0; t\neq\tau, \qquad \int_{-\infty}^{\infty} f(\tau)\delta(t-\tau)d\tau = f(t) \tag{4.34}$$

for any square-integrable function of f(t). This means that random variables from the white noise process are completely uncorrelated for any set of time instances. A discrete white noise process, $W(t_k)$, can be derived from the continuous white noise using an averaging process with respect to time. The mean of the discrete white noise is the same as that of the continuous white noise and the variance is given as $q/\Delta t$.

$$E(\Omega(t)) = E(W(t_k)); \quad \sigma_w^2 = \frac{q}{\Delta t} \tag{4.35}$$

If the distribution of each random variable of the discrete white noise process is Gaussian with zero mean, the process is called Gaussian white noise $W(t_k) := W_k \sim N(0, q/\Delta t)$.

A random constant assumes a constant value for all variables of a single realization of the process. The random constant is represented by the following differential equation:

$$\dot{x}(t) = 0; \qquad x(t_0) = x_0, \tag{4.36}$$

where x_0 is a random variable. It should be noted that the random constant is stationary but not ergodic. Also, it is fully correlated. The mean of the random constant may be assumed to be zero and the auto-covariance would be the variance σ_x^2. The discrete form of the random constant is represented as:

$$x_{k+1} = x_k. \tag{4.37}$$

The general biases and scale factor errors for the gyros and accelerometers can be modeled as random constants since these are known to be very stable after turn on. Using the linear dynamic equations in (4.36), the general biases and the scale factors can be included as unknown parameters (random effects) in the error dynamics equation (4.19).

4.3.2 Gravity Disturbances

The last row of the systematic error vector (4.19) is associated with the error in the Earth's gravity field. In other words, it is the difference between the actual Earth's gravitation and a selected model for the gravitation. The most popular gravity model in the field of navigation is the normal gravity field generated by an ellipsoid of revolution. This ellipsoid contains the Earth's mass and its equipotential surface approximates the Earth's mean sea level surface. It should be noted that the normal gravity vector on its surface does not have horizontal components because, by definition, it is perpendicular to the ellipsoidal normal. At given altitude, however, the north-south component of the normal gravity is not zero (see Heiskanen and Moritz, (5-34)). The actual horizontal component of the gravity vector with a magnitude at the order of $4 \sim 6 \times 10^{-4}$ m/s^2 causes position error up to several hundred meters (Jekeli, 1995a) when neglected.

To compensate the position error caused by neglecting the horizontal gravity

vector, one can model the incremental gravity field, or gravity disturbance vector, as a spatial process. Many forms of spatial models have been developed to represent the random-like fashion of the variations of the horizontal gravity field disturbances. These models are used in accounting for position errors and/or to obtain optimal estimates for the disturbing gravity field. In airborne gravimetry, the spatial models of the disturbing gravity field have been used for estimating the gravity field while assuming that all other INS related errors could be estimated using other instruments like GPS. Usually, the models for the gravity field assume ergodicity and, hence, stationarity and some isotropic covariance function that depends on two parameters: variance and the correlation distance. For details or forms of the covariance models, see Wang and Jekeli (1998), Jekeli (1995), Knickmeyer (1990), Forsberg (1987) and Eissfeller and Spietz (1989).

One of the often used models for the horizontal gravity components along a trajectory is the Gauss-Markov process. The (first order) Markovian property states that the conditional probability density of the random variable at any time is the same as the conditional probability density of the variable given just the most recent values of the process. If the process is also Gaussian, the process is called a Gauss-Markov process. With some information on variance and correlation distance obtained from an empirical covariance function, one could integrate the gravity model into the error dynamics equation.

The differential equation for the first-order Gauss-Markov model is given by

$$\dot{x}(t) = -\beta x(t) + \Omega(t) \tag{4.38}$$

where β is a constant, and Ω is a zero mean Gaussian white noise process with covariance:

$$E(\Omega(t)\Omega(t')) = 2\sigma^2\beta\delta(t-t'). \tag{4.39}$$

The process, $x(t)$, in this case is stationary with zero mean, and covariance function and the corresponding PSD (power spectral density, Fourier transform of the covariance) are given by

$$C_x(\tau) = \sigma^2 e^{-\beta|\tau|}, \tag{4.40}$$

$$\Phi_x(\omega) = \frac{2\sigma^2\beta}{\omega^2+\beta^2}. \tag{4.41}$$

The inverse of the constant β, $1/\beta$, called the correlation time and defines the degree of correlation. When β approaches zero, the signal becomes a random constant.

The higher-order Gauss-Markov processes are also defined on the basis of higher-order differential equations with the parameter β. The differential equation for the third-order model and the corresponding quantities are given as:

$$\dddot{x}(t) + 3\beta\ddot{x}(t) + 3\beta^2\dot{x}(t) + \beta^3 x(t) = \Omega(t), \tag{4.42}$$

$$E(\Omega(t)\Omega(t')) = \frac{16}{3}\beta^5\sigma^2\delta(t-t'), \tag{4.43}$$

$$C_x(\tau) = \sigma^2 e^{-\beta|\tau|}(1+\beta|\tau| + \frac{1}{3}\beta^2\tau^2); \qquad \Phi_x(\omega) = \frac{(16/3)\beta^5\sigma^2}{(\omega^2+\beta^2)^3}. \tag{4.44}$$

4.4 Kalman Filter Estimation in the Conventional Approach

Establishing the stochastic models for the INS systematic errors and the gravity disturbances, one can revise the error dynamics equation by adding more parameters into the vector ε^n of equation (4.19). In other words, a 30-state linear error dynamics equation can be derived that models the general biases and scale factor errors for both gyros and accelerometers as random constants, and the gravity disturbances as the third-order Gauss-Markov models;

$$\frac{d}{dt}\mathbf{x}^n = \mathbf{F}^n\mathbf{x}^n + \mathbf{G}^n\mathbf{u}. \tag{4.45}$$

Note that the notation for the error vector ε^n is now changed to $\mathbf{x}^n$ denoting it as the state vector. The state vector $\mathbf{x}^n$ is composed of 3 orientation errors, 3 velocity errors, 3 position errors, 3 accelerometer biases (random effects), 3 accelerometer scale factors, 3 gyro biases (random effects), 3 gyro scale factors and 9 parameters associated with the third-order Gauss-Markov gravity disturbance vector.

$$\begin{aligned}\mathbf{x}^n = (&\psi_N\psi_E\psi_D\delta\dot{\phi}\,\delta\dot{\lambda}\,\delta\dot{h}\,\delta\phi\,\delta\lambda\,\delta h\,b_{aN}b_{aE}b_{aD}k_{aN}k_{aE}k_{aD}b_{gN}b_{gE}b_{gD}k_{gN}k_{gE}k_{gD}\\ &\delta g_N\delta g_E\delta g_D\delta g'_N\,\delta g'_E\,\delta g'_D\,\delta g''_N\,\delta g''_E\,\delta g''_D)^T\end{aligned} \tag{4.46}$$

The dynamics matrix **F**, the noise influence matrix **G** and the white noise vector **u** are given as below. Note that each element in the matrices F_{12}, F_{13} and G is a 3×3 matrix.

$$F^n = \begin{bmatrix} F_{11} & F_{12} & F_{13} \\ 0 & 0 & 0 \\ 0 & 0 & F_{33} \end{bmatrix}$$

$$F_{11} = \begin{bmatrix}
0 & -\dot{l}_1\sin\phi & \dot{\phi} & 0 & \cos\phi & 0 & -\dot{l}_1\sin\phi & 0 & 0 \\
\dot{l}_1\sin\phi & 0 & \dot{l}_1\cos\phi & -1 & 0 & 0 & 0 & 0 & 0 \\
-\dot{\phi} & -\dot{l}_1\cos\phi & 0 & 0 & -\sin\phi & 0 & -\dot{l}_1\cos\phi & 0 & 0 \\
0 & \dfrac{-a_3^n}{r} & \dfrac{a_2^n}{r} & \dfrac{-2\dot{h}}{r} & -\dot{l}_1\sin 2\phi & \dfrac{-2\dot{\phi}}{r} & \Gamma_{11}^n - \dot{\lambda}\dot{l}_2\cos 2\phi & \Gamma_{12}^n\cos\phi & \dfrac{\ddot{\phi} + \frac{1}{2}\dot{\lambda}\dot{l}_2\sin 2\phi + \Gamma_{13}^n}{-r} \\
\dfrac{a_3^n}{r\cos\phi} & 0 & \dfrac{-a_1^n}{r\cos\phi} & 2\dot{l}_1\tan\phi & 2(\dot{\phi}\tan\phi - \dfrac{\dot{h}}{r}) & \dfrac{-2\dot{l}_1}{r} & \begin{matrix}2\dot{l}_1(\dot{\phi} + \dfrac{\dot{h}\tan\phi}{r}) \\ +\ddot{\lambda}\tan\phi + \Gamma_{21}^n\sec\phi\end{matrix} & \Gamma_{22}^n & \dfrac{2\dot{\phi}\dot{l}_1\tan\phi - \ddot{\lambda} - \dfrac{\Gamma_{23}^n}{\cos\phi}}{r} \\
a_2^n & -a_1^n & 0 & 2r\dot{\phi} & 2r\dot{l}_1\cos^2\phi & 0 & -r\dot{\lambda}\dot{l}_2\sin 2\phi - r\Gamma_{31}^n & -r\cos\phi\Gamma_{32}^n & \dot{\phi}^2 + \dot{\lambda}\dot{l}_2\cos^2\phi + \Gamma_{33}^n \\
0 & 0 & 0 & 1 & 0 & 0 & 0 & 0 & 0 \\
0 & 0 & 0 & 0 & 1 & 0 & 0 & 0 & 0 \\
0 & 0 & 0 & 0 & 0 & 1 & 0 & 0 & 0
\end{bmatrix}, \tag{4.47}$$

$$F_{12}^{n} = \begin{bmatrix} 0 & 0 & -C_b^n & -C_b^n\left[\omega_{ib}^b\right] \\ D^{-1}C_b^n & D^{-1}C_b^n\left[a^b\right] & 0 & 0 \\ 0 & 0 & 0 & 0 \end{bmatrix},$$
$$F_{13}^{n} = \begin{bmatrix} 0 & 0 & 0 \\ D^{-1} & 0 & 0 \\ 0 & 0 & 0 \end{bmatrix} \tag{4.48}$$

$$F_{33}^{n} = \begin{bmatrix} 0 & 0 & 0 & 1 & 0 & 0 & 0 & 0 & 0 \\ 0 & 0 & 0 & 0 & 1 & 0 & 0 & 0 & 0 \\ 0 & 0 & 0 & 0 & 0 & 1 & 0 & 0 & 0 \\ 0 & 0 & 0 & 0 & 0 & 0 & 1 & 0 & 0 \\ 0 & 0 & 0 & 0 & 0 & 0 & 0 & 1 & 0 \\ 0 & 0 & 0 & 0 & 0 & 0 & 0 & 0 & 1 \\ -\beta_1^3 & 0 & 0 & -3\beta_1^2 & 0 & 0 & -3\beta_1 & 0 & 0 \\ 0 & -\beta_2^3 & 0 & 0 & -3\beta_2^2 & 0 & 0 & -3\beta_2 & 0 \\ 0 & 0 & -\beta_3^3 & 0 & 0 & -3\beta_3^2 & 0 & 0 & -3\beta_3 \end{bmatrix} \tag{4.49}$$

$$G^{n} = \begin{bmatrix} -C_b^n & 0 & 0 \\ 0 & D^{-1}C_b^n & D^{-1} \\ 0 & 0 & 0 \\ 0 & 0 & 0 \\ 0 & 0 & 0 \\ 0 & 0 & 0 \\ 0 & 0 & 0 \\ 0 & 0 & 0 \\ 0 & 0 & 0 \\ 0 & 0 & I \end{bmatrix}, \quad \mathbf{u} = \begin{bmatrix} w_g \\ w_a \\ w_{\delta g} \end{bmatrix}, \quad D\{\mathbf{u}\} = \begin{bmatrix} \sigma_g^{\,2} & 0 & 0 \\ 0 & \sigma_a^{\,2} & 0 \\ 0 & 0 & \sigma_{\delta g}^{\,2} \end{bmatrix} \tag{4.50}$$

where D is the matrix converting from angular to linear measure and inverting the vertical axis; $\sigma_g^{\,2}$, $\sigma_a^{\,2}$ and $\sigma_{\delta g}^{\,2}$ are variances of the white noise for gyro, accelerometer and gravitational disturbance respectively.

$$D = \begin{bmatrix} R+h & 0 & 0 \\ 0 & (R+h)\cos\phi & 0 \\ 0 & 0 & -1 \end{bmatrix} \tag{4.51}$$

Optimal estimates for the 30 states at each epoch are easily obtained from the error dynamics equations and additional observations by Kalman filtering. Since the Kalman filter is well described in the literature (Gelb, 1994; Brown and Hwang, 1997),

only the essential concepts and equations are presented. There are three things to be defined before applying a Kalman filter: System model, Measurement model and Initial conditions. The measurement model, also called the observation equations, is given by

$$\mathbf{Z}_k = \mathrm{H}\mathbf{x}_k + \mathbf{v}_k, \mathbf{v}_k \sim \mathrm{N}(0, \mathrm{R}_k), \tag{4.52}$$

where the subscript k indicates the epoch to which the data refer, $\mathbf{Z}$ is the 3×1 observation vector (GPS position – INS position), H is the 3×30 design matrix with 1 for elements at the positions (1,7), (2,8), (3,8) and zeros for all other elements, $\mathbf{v}$ is the 3×1 observation error vector assumed normally distributed with zero mean and 3×3 covariance matrix R.

The system model representing the dynamics of the parameters at time t_{k-1} and t_k is given as:

$$\mathbf{x}_k = \Phi_{k-1}\mathbf{x}_{k-1} + \mathrm{G}_{k-1}\mathbf{w}_{k-1}, \qquad \mathbf{w}_k \sim \mathrm{N}(0, \mathrm{Q}_k), \tag{4.53}$$

where Φ_{k-1} is the state transition matrix between times t_k and t_{k-1}. Assuming the system dynamics matrix F is constant during transition time (Δt), the transition matrix can be calculated as follows.

$$\Phi_{k-1} = \mathrm{e}^{\mathrm{F}(t_k - t_{k-1})} = \mathrm{I} + \mathrm{F}\Delta t + \frac{1}{2!}(\mathrm{F}\Delta t)^2 + \frac{1}{3!}(\mathrm{F}\Delta t)^3 + \ldots\ldots \tag{4.54}$$

Note that the state transition matrix Φ_{k-1} and the input matrix G_{k-1} are assumed constant during transition times, and the input noise vector $\mathbf{w}_k$ is described by a Gaussian, zero-mean, white-noise processes with covariance matrix Q_k derived using the relationships between the continuous and discrete white noise (see equations (4.33) and (4.35)). It is assumed that $\mathbf{v}_k$ and $\mathbf{w}_k$ are not correlated with each other. If there are no measurements, the dynamics of the state vector totally depend on the system model.

For the initial conditions, we need to define the estimates and variances of the state parameters at starting time. The initial estimates are set to zero for all error states. In addition, the initial variances are set to the values from the manufacturer's specifications for INS errors. The initial variance and the correlation distance for the gravity disturbance vector could be obtained from previous spatial analysis of the incremental field being surveyed. Table 4.1 shows the initial variances for the states applied in this study.

The advantage of the Kalman filter lies in the fact that the estimation procedure is explicitly divided into two stages: prediction and update. In addition, the procedures for the state estimates are independent of those of the covariances of the estimates (Figure 4.2). Therefore, one can conduct covariance analyses without using real data. These analyses are useful for a pre-planning or a feasibility test. For the covariance analysis of airborne gravimetry, see Jekeli (1995) and Knickmeyer (1990).

INS Error Parameters	Standard deviation
Accelerometer Biases (random)	±25 mGal
Accelerometer Scale Factor	±10 ppm
Gyro Bias (random)	±0.005 deg/hr
Gyro Scale Factor	±10 ppm
Gyro White Noise	±0.002 deg/$\sqrt{\text{hr}}$
Accelerometer White Noise	±40 mgal/$\sqrt{\text{Hz}}$
Velocity	±1 m/s
Position	±10 m
Orientation for Horizontal Direction	±2 arcsec.
Orientation for Vertical Direction	±1 arcmin.
3rd order G.M Process for Gravity Disturbances	±20 mGal
Inverse of the Correlation Time	1×10^{-4}

Table 4.1 INS error parameter specification.

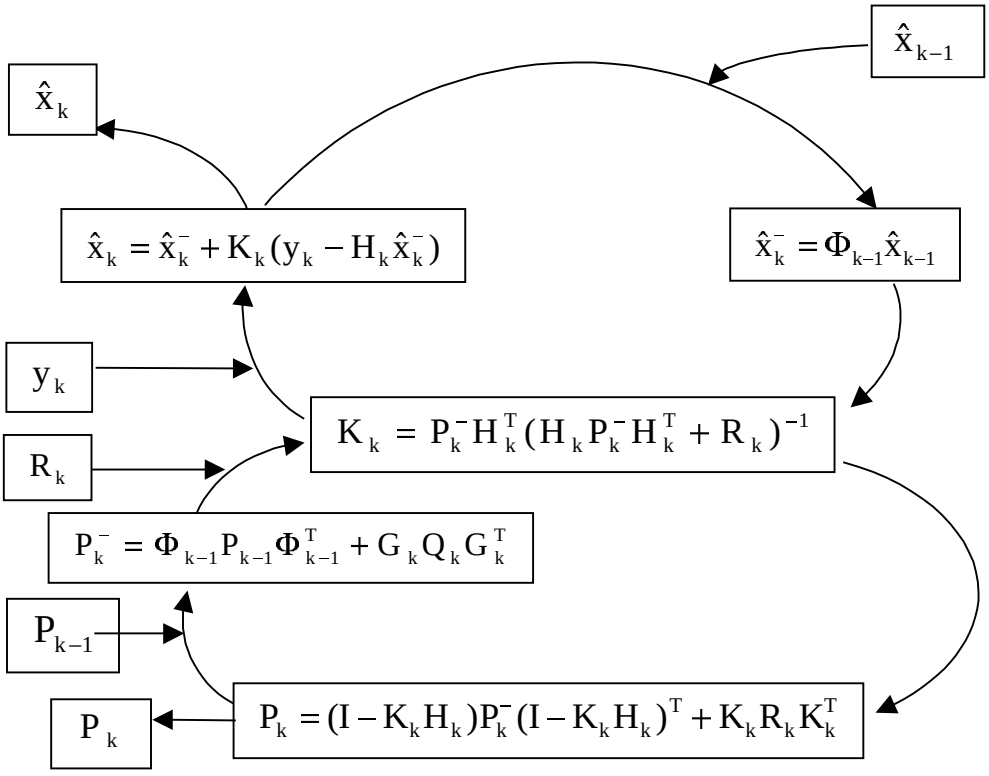

Figure 4.2 Kalman filter loop following Jekeli (1995a).

If no real measurements are available, one can perform only the prediction given by

$$\hat{\mathbf{x}}_k^- = \Phi_{k-1}\hat{\mathbf{x}}_{k-1}, \tag{4.55}$$

$$P_k^- = \Phi_{k-1}P_{k-1}\Phi_{k-1}^T + G_k Q_k G_k^T, \tag{4.56}$$

where P denotes the covariance matrix for the states.

Note that the negative sign on the superscript means the observation at that time t_k has not been accounted for. So, the predicted states only depend on the system transition matrix, and covariances of those depend on the corresponding error propagation laws.

Once actual data are available, one can perform the updating procedure that results in new estimates for the states and covariances that include the information from the measurement.

$$\hat{\mathbf{x}}_k = \hat{\mathbf{x}}_k^- + K_k(\mathbf{y}_k - H_k\hat{\mathbf{x}}_k^-), \tag{4.57}$$

$$P_k = (I - K_k H_k)P_k^-(I - K_k H_k)^T + K_k R_k K_k^T, \tag{4.58}$$

where K is the Kalman gain matrix defined as

$$K_k = P_k^- H_k^T (H_k P_k^- H_k^T + R_k)^{-1}. \tag{4.59}$$

In general, the GPS position is derived from the double differencing procedure as mentioned in Chapter 3. Currently, the accuracy of the positions derived from the double differencing is less than ±10 cm in the kinematic case. Since the observation vector in this traditional approach is the difference between the GPS and INS positions, the navigation equations (3.33) should be integrated first. The integrated positions from INS, of course, include all the effects of the system errors. Using the more accurate positions from GPS, system errors in INS are to be estimated in the Kalman filter. At the same time, the gravity disturbance vector is also to be determined based on the selected gravity model. The algorithm for integrating the navigation equations using quaternions is given in the Appendix A.

4.5 Results from the Traditional Approach

4.5.1 Test Data Description

The data used in this study were provided by M. Wei, under the promotion of the Special Study Group 3.164, Airborne Gravimetry Instrumentation and Methods, of the International Association of Geodesy (IAG). These data were collected by the University of Calgary on 1 June 1995 for the purpose of conducting an airborne gravity survey over a part of the Rocky Mountains to assess repeatability as well as the accuracy of airborne gravimetry using GPS and INS. The strapdown inertial system, Honeywell LASEREF III, together with two GPS receivers, Ashtech Z-XII and NovAtel GPSCard, were equipped on the airplane. To perform the DGPS positioning, three base stations were also operated on the ground. The data include the coordinates of the airborne and ground GPS antennas at 0.5s intervals, and raw accelerometer and gyro data from INS at a data rate of 50 Hz.

In this survey, four flights, of which three flight data are usable, in the east-west

direction over the same ground track were carried out. The overlapping flight trajectory was designed to meet the objectives of the test. The total length of the east-west profile was 250 km and the flying altitude was 5.5 km. Average flying speed was about 430 km/h so the corresponding spectral resolution for 90 and 120 seconds smoothing was about 5.0 km to 7.0 km. For details on the data description, see Wei and Schwarz (1998).

Figure 4.3 shows the trajectories of the three flights. Lines 1 and 3 are almost on top of each other and the line 2 is a little north (.005 degree ≈ 540 meters) from those.

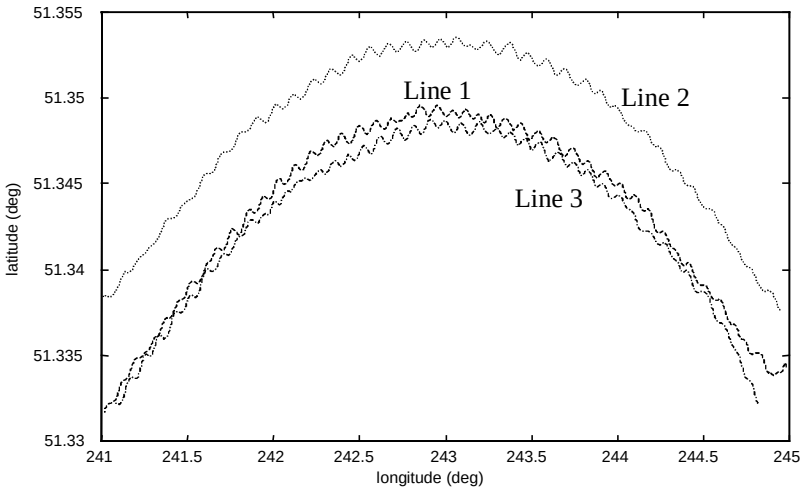

Figure 4.3 Flight trajectory for the test data June 1995. Dashed line (middle) line is leg1, dotted line (top) is leg 2, and dash-dotted (bottom) line is leg 3.

Note the high frequency variations of the trajectories showing the dynamics of the flight. The main oscillations occurred around the first (roll) and the third (yaw) axes of the body frame. Probably, these dynamics are caused by the auto-pilot function of the airplane which automatically maintains the direction and the velocity of the airplane. Comparing the attitude of the airplane (Figure 4.4) with the trajectory shows that those variations correspond well to the roll and yaw motions of the airplane with periods of 50-60 seconds.

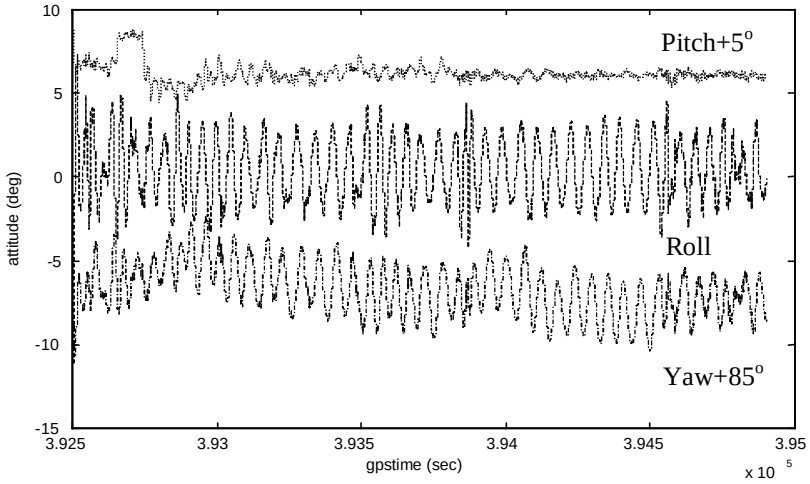

Figure 4.4 The attitude of the airplane for Line 1 (392500-394900 GPS seconds).

Obviously, it is very hard to separate the gravity signal with the frequency in the range of these dynamics. The effect of dynamics will be explained in more detail in the next Chapter.

4.5.2 Horizontal Gravity Disturbances from the Traditional Approach

Using the algorithm explained in the previous sections, the traditional approach of position update with gravity modeling was tested. It should be mentioned that only the horizontal components of the gravity disturbance vector could be estimated in the conventional approach, since the INS is unable to navigate in the vertical in the free-inertial mode (see section 4.5.3).

Figure 4.5 shows the horizontal gravity disturbance estimates of all three legs for the north and east direction as determined by the traditional algorithm. One can notice the high frequency oscillations with periods of 50-60 seconds in the north component, which are caused by the roll dynamics of the aircraft motion. The very high frequency variations in the line 2 and 3 of the east component are caused by a numerical instability of the filter due to unknown effects.

In addition, low frequency trends as well as the biases (random) still appear to remain in all legs. This means that the biases of the accelerometers could not be estimated unless external information on the gravity, for example the gravity values at the starting and ending point, is provided. Therefore, some further data processing is necessary to remove the high frequency errors, low frequency trends, as well as the effects of airplane dynamics. For these purposes, B-spline smoothing and wave number correlation filtering (WCF) has been adopted in this approach.

The usual method to remove high frequency components from a signal is to

apply a low pass filter, or a smoother. In this study, a third-order B-spline smoother with window length of 60 seconds was applied to remove the high frequency error from the estimated gravity disturbances. Because of its simplicity and flexibility, the B-spline smoother is distinguished by its elegant theory and model behavior in numerical calculations (Kincaid and Cheney, 1996, p. 392).

To remove low frequency trends as well as other residual errors that are not correlated between overlapping trajectories, one can apply the wavenumber correlation filter (WCF) developed by von Frese et al. (1997). Basically, the WCF decomposes space domain data into wave domain coefficients through a Fourier transformation, and then constructs the correlation spectrum by comparing coefficients of a pair of co-registered data at corresponding wavelength.

The wavenumber correlation coefficient between two data sets $\overline{x}$ and $\overline{y}$ is defined as:

$$CC_k = \cos(\Delta\theta_k) = \frac{\overline{x}_k \bullet \overline{y}_k}{\left|\overline{x}_k\right|\left|\overline{y}_k\right|}, \tag{4.60}$$

where CC_k is the correlation coefficient for the wave number k, $\Delta\theta_k$ is the phase difference of the data set $\overline{x}$ and $\overline{y}$, $\Delta\theta_k = \theta_{\overline{x}} - \theta_{\overline{y}}$, and $\bullet$ denotes the scalar product of vectors. By setting the correlation tolerance, the components showing less correlation than the tolerance is assumed as noise and filtered out. For example, if the correlation tolerance is set to 0.5 all components having correlation coefficient larger than the tolerance are kept as signal. For a detailed derivation of the wave number correlation coefficient, see Kim (1995).

The repeated tracks provide an opportunity to decorrelate the gravity signal from some of the system errors, since presumably the gravity signature has not changed from one leg to the other. In other words, since we have three overlapping flight legs, one can assume that the gravity signal is commonly detected in all three legs, but the random noise and system errors would not usually be common for those legs. Therefore, using WCF, one can filter out the random noise or overall trends that are not common in other lines. With the WCF the removal of overall trends as well as the medium frequency airplane dynamics effects could be achieved. It should be noted that two filtered data sets are obtained from WCF, thus the average of those are presented as results from WCF. As a matter of fact, tracks do not have to be on top of each other to apply WCF. As long as the signal could be co-registered such as in parallel tracks, WCF can be applied.

The correlation tolerance in this study is set to zero. It should be noted that the correlation tolerance is decided rather subjectively based on the signal characteristics. In other words, there is a trade-off between the correlation and noise, but it is intended to keep the correlated signal as much as possible for each pair of tracks. Therefore, after examining the correlation coefficients for each frequency component, one has to decide the tolerance imposing the amount of signals to be extracted.

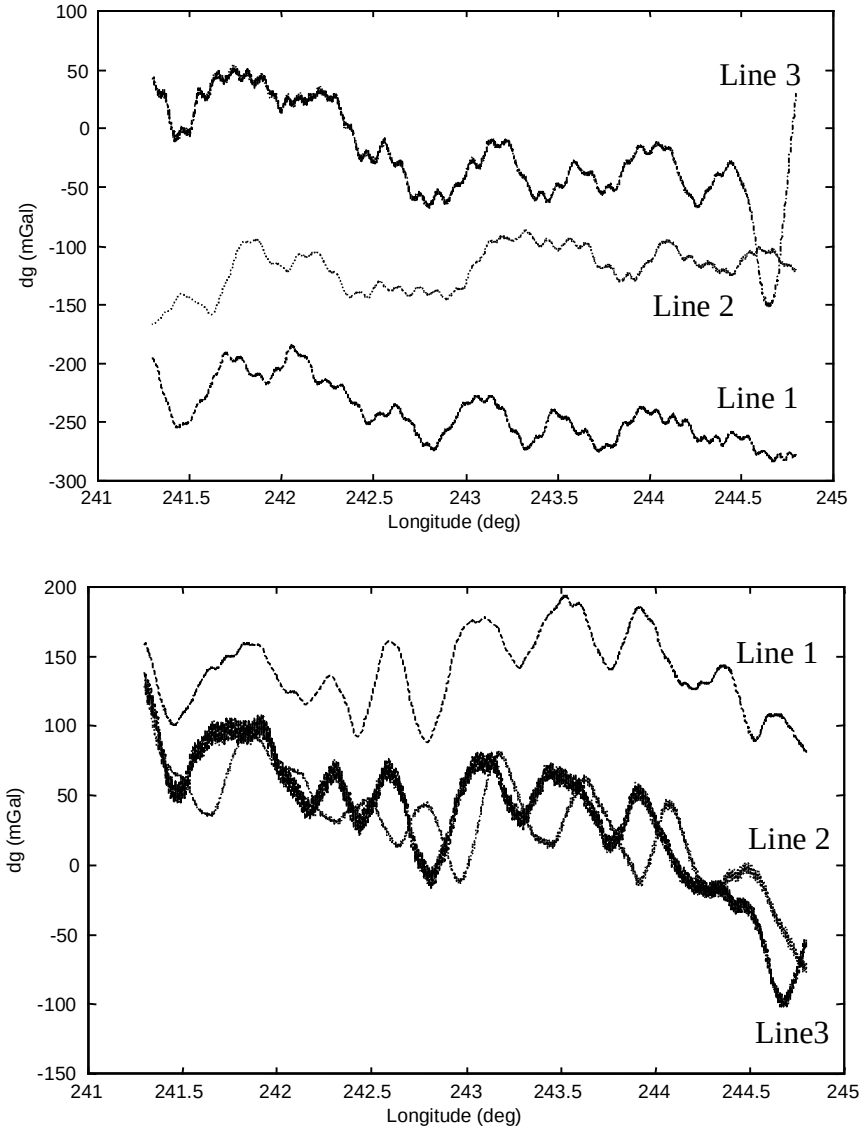

Figure 4.5 Gravity disturbance components, north (top) and east (bottom), computed from the traditional position update Kalman-filtering. The dashed, dotted, and dash-dotted lines are the gravity components calculated for legs 1, 2 and 3, respectively.

Finally, we assume that the gravity values for the endpoints are known in order to remove the biases random effects. This endmatching is done by applying linear corrections to the estimates based on values at both ends of each leg using reference data provided by the National Imagery and Mapping Agency (NIMA). The reference data consist of the deflections of vertical (horizontal gravity component) for this area extracted from 2 min. by 2 min. grids of gravity anomalies.

It should be noted that this additional data procedures could be applied in different order. In other words, one can apply the endmatching first, and then the WCF, or the other way around. Interestingly, the order of the processing seems to affect the results of the gravity estimates. The results of the first case were better than the other (compare Table 4.2 and 4.3).

Figure 4.6 shows the horizontal gravity disturbance estimates after applying the 60-seconds smoothing, WCF and endmatching. The High frequency oscillations are removed by the smoothing, the gravity components along all three lines are adjusted to match given values at the end points, and the global trends are reduced by WCF. Estimated gravity disturbances, generally, show higher amplitude than the reference data. The reason for this could be explained through model error, including wrong statistical models for the INS error parameters and for the gravity disturbances, as well as wrong initial values from insufficient a priori knowledge in the orientation of the INS. As a matter of fact, the results shown in Figure 4.6 were selected from repeated use of trials of different models for the gravity disturbances and initial variances for the parameters. For the gravity disturbance, the 3rd order Gauss-Markov model with correlation distance in the range of 10-1000 km and variance in the range of 100-10000 mGal^2 were tested. The gravity disturbance estimates were more sensitive to the correlation distance than the variances in this case.

Therefore, it is very crucial to establish an appropriate model for the gravity disturbances as well as to assign good correlation distance and initial variances in the traditional approach. A numerical comparison with respect to the reference gravity data is given in Table 4.2. It should be mentioned that the wavenumber correlation filtering should be done between legs having opposite directions. That is, it seems that some systematic errors appear to be associated with the direction (see the phase delay in leg 2 of the east component in Figure 4.5). This will be demonstrated more clearly in case of the acceleration update algorithm and will be explained in the next chapter.

The best result with the traditional approach is obtained for the north component from the combination of lines 1 and 2. In both combinations in Table 4.2, the north components are better estimated than the east component. If these errors are attributed to incorrect modeling, especially the gravity modeling errors, then one might conjecture that the adopted Gauss-Markov process for the gravity disturbance was better for the north component than for the east component. As a matter of fact, the east component estimates turned out to be better in the acceleration algorithm (see Chapter 5) that does not rely on a statistical model for the gravity disturbances.

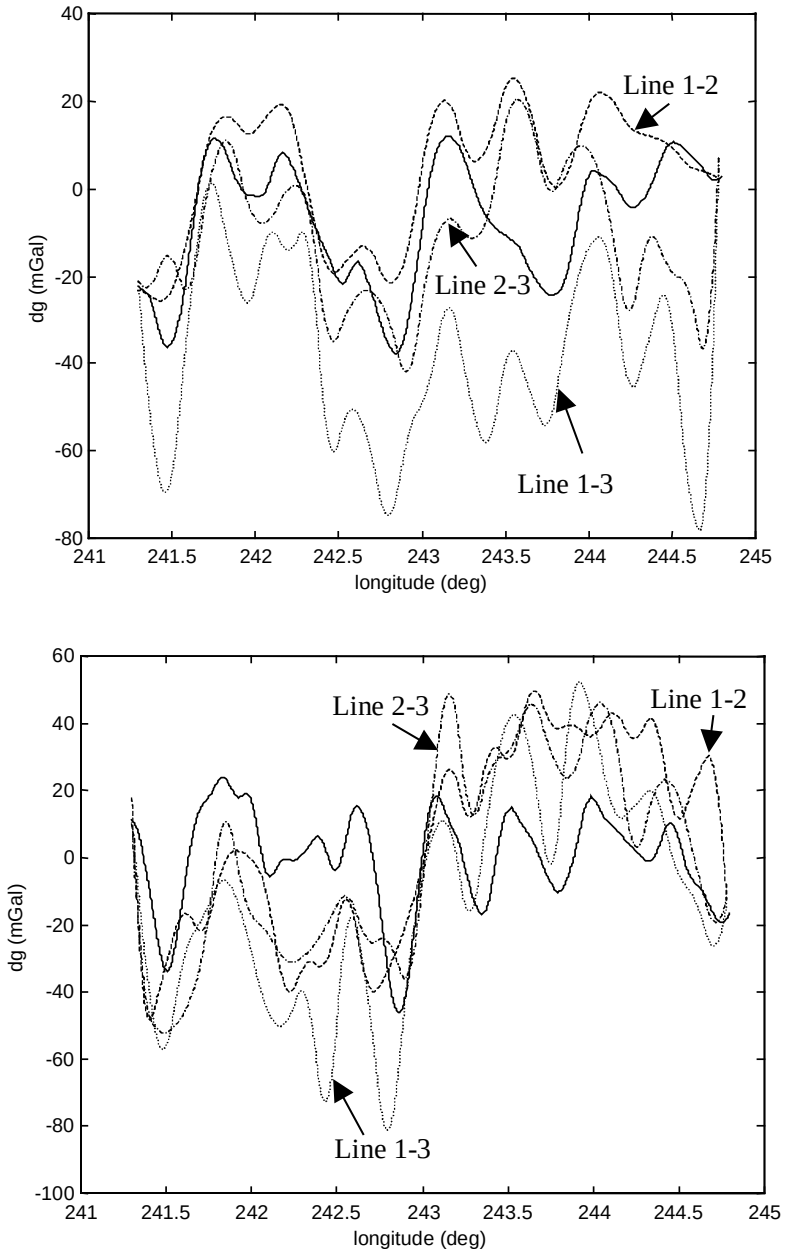

Figure 4.6 Gravity disturbance components, north (top) and east (bottom), after applying 60-seconds smoothing, WCF and endmatching. The solid line shows the reference gravity data; the dashed, dotted, and dash-dotted lines show the gravity components calculated from the combinations of lines 1-2, 1-3, and 2-3, respectively.

	Lines 1/2 (mGal)		Lines 2/3 (mGal)	
	Mean	Std. Dev.	Mean	Std. Dev.
North	11.67	9.98	-3.61	17.13
East	4.68	28.88	-0.16	25.74

Table 4.2 Mean and standard deviation of the difference between the calculated horizontal gravity disturbance from the traditional approach and the control data. The data are processed by first applying the 60-seconds smoothing, then WCF and endmatching.

Figure 4.7 shows the horizontal gravity disturbances after 60-seconds smoothing, end-matching and WCF. Note the partially reversed order of processing compared to the previous case. Although the low wavelength parts of the estimates for this case and the previous case are very similar, there are some minor differences in the local peaks and valleys due to from the change in order of the processing steps. The standard deviations of the differences between the reference gravity and the estimated gravity are given in Table 4.3.

	Lines 1/2 (mGal)		Lines 2/3 (mGal)	
	Mean	Std. Dev.	Mean	Std. Dev.
North	7.65	8.87	7.62	16.21
East	9.03	26.34	0.32	25.52

Table 4.3 Mean and standard deviation of the difference between the calculated horizontal gravity disturbance from the traditional approach and the control data. The data are processed by first applying the 60-seconds smoothing, then endmatching and WCF.

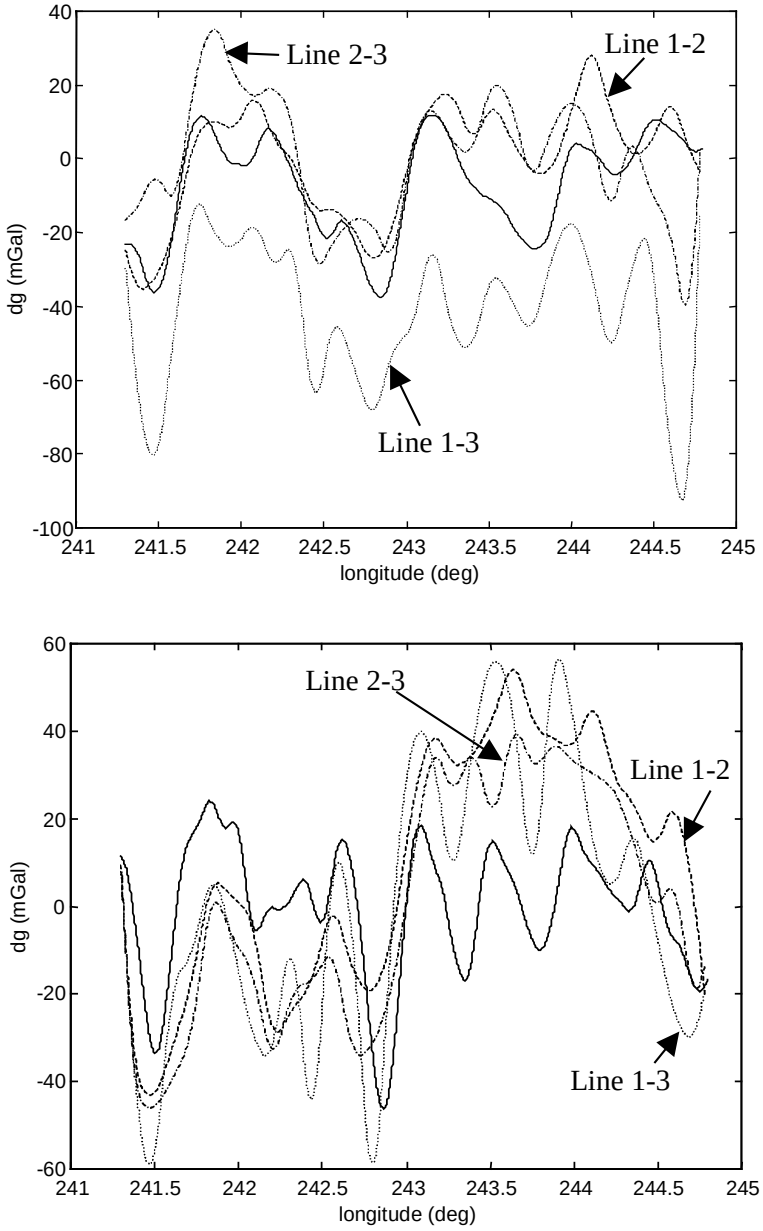

Figure 4.7 Gravity disturbance components, north (top) and east (bottom), after applying 60-seconds smoothing, endmatching and WCF. The solid line shows the reference gravity data; the dashed, dotted, and dash-dotted lines show the gravity components calculated from the combinations of lines 1-2, 1-3, and 2-3, respectively.

4.5.3 Vertical Gravity Disturbances from the Traditional Approach

As mentioned, the vertical component of the gravity disturbance can not be estimated using the traditional method. The reason for this can be explained by a simple analysis showing the instability of the vertical channel in the INS.
The analysis starts with the fundamental equation of airborne gravimetry again.

$$\ddot{\mathbf{x}}^{i} = \mathbf{g}^{i}(\mathbf{x}^{i}) + \mathbf{a}^{i} \tag{4.61}$$

Note that the dependency of the gravitational acceleration on the position vector is explicitly expressed. Applying the linear differential operator, δ, to (4.61),

$$\delta\ddot{\mathbf{x}} = \frac{\partial \mathbf{g}}{\partial \mathbf{x}}\delta\mathbf{x} + \delta\mathbf{g} + \delta\mathbf{a} \tag{4.62}$$

Now, use the spherical approximation of the gravitational acceleration, $\mathbf{g} = \left(\frac{-\mathrm{kM}}{\mathrm{r}^2}\right)\mathbf{n}$, where $\mathbf{n}$ is the unit normal vector pointing outward along the radial direction; kM is the gravitational constant times the mass of the Earth ($\mathrm{kM} \approx 3.986 \times 10^{14}\,\mathrm{m}^3/\mathrm{s}^2$). And approximate $\frac{\partial \mathbf{g}}{\partial \mathbf{x}} \approx \frac{\mathrm{kM}}{\mathrm{r}^3}\begin{pmatrix} -1 & 0 & 0 \\ 0 & -1 & 0 \\ 0 & 0 & 2 \end{pmatrix}$, then the differential equations for the components of the position error are given by

$$\delta\ddot{\mathbf{x}}_1 + \frac{\mathrm{kM}}{\mathrm{r}^3}\delta\mathbf{x}_1 = \delta\mathbf{g}_1 + \delta\mathbf{a}_1, \tag{4.63}$$

$$\delta\ddot{\mathbf{x}}_2 + \frac{\mathrm{kM}}{\mathrm{r}^3}\delta\mathbf{x}_2 = \delta\mathbf{g}_2 + \delta\mathbf{a}_2, \tag{4.64}$$

$$\delta\ddot{\mathbf{x}}_3 - \frac{2\mathrm{kM}}{\mathrm{r}^3}\delta\mathbf{x}_3 = \delta\mathbf{g}_3 + \delta\mathbf{a}_3. \tag{4.65}$$

The homogeneous solution of the horizontal components, (4.63) and (4.64), represents the forced harmonic oscillation with Schuler frequency, $\omega_s = \sqrt{\mathrm{kM}/\mathrm{r}^3}$ while that of the vertical component increases exponentially on time. So, initial errors in horizontal position and velocity are modulated by the Schuler frequency and that in vertical position causes exponential growth with respect to time. This instability in the vertical channel consequently causes the corresponding navigation solution fail. Therefore, the position update will not be able to distinguish the gravity signal from other errors in the vertical channel.

During the past two decades, a couple of methods have been developed for scalar gravimetry in which only the down component is estimated. The instruments in the scalar gravimetry are composed of either a gravimeter (Brozena et al., 1989; Brozena and Peters, 1994; LaCoste et al., 1982; Salychev et al., 1994) or an INS (Wei and Schwarz, 1998; Glennie et al., 1999) in combination with external positioning systems such as GPS, radar, Loran C, etc. In the first case, a stable platform system is used to maintain the sensor direction to the local down, and a strapdown system is employed in the second case.

A method developed at the University of Calgary, called Strapdown Inertial Scalar Gravimetry (SISG), showed that the down component can be recovered with accuracy of ±2-3 mGal with 90- or 120-second low pass filtering (Wei and Schwarz, 1998). The first step of the SISG technique is to transform the specific forces measured in the body frame into the local level frame using the attitude information from the gyro. Secondly, the GPS acceleration is derived from the DGPS position solution by applying a numerical differentiator. Thirdly, the difference between the specific force and the GPS acceleration is calculated to obtain the gravity disturbance. The errors in INS such as biases (random) scale factors, and drift rates are estimated and taken out by a closed-loop Kalman filter using the GPS phase and Doppler observations. For details about the equations and GPS/INS integration strategy, see Cannon (1991).

Although the SISG technique uses GPS double-differenced phase and Doppler measurements instead of GPS derived position or velocity for the estimation of IMU's errors, the estimation still needs the integration of the error dynamics equations derived from the navigation equations. In addition, the gravity disturbance vector needs to be modeled because the error dynamics equations contain the gravity terms. These two aspects distinguishes the traditional approach explained in this chapter and a new acceleration update algorithm explained in the next chapter. Detailed conceptual and numerical comparisons between the traditional and the new approach are given in next chapter.

CHAPTER 5

A NEW ACCELERATION UPDATING KALMAN FILTER FOR VECTOR GRAVIMETRY

5.1 Overview

As investigated in the previous chapter, the traditional approach of GPS/INS airborne gravimetry integrates the navigation equation to get the INS positions with a selected gravity model, then the observables from GPS such as phase, Doppler shift, position and velocity are used to estimate the INS system errors. Conventionally, the calculation of the traditional approach is performed in the navigation frame. The estimates of the gravity disturbance, in this case, very much depend on the gravity models so that one has to have a fairly good a-priori information on the gravity field or perform many trial-and-error experiments by changing the models and parameters. Therefore, the disadvantage of this approach is its dependency on the model for the gravity and the expensive computation of the INS position integration. In addition, the navigation equations in the n-frame involved with much mathematical formulas and physical concepts and make the problem unnecessarily complicated.

Alternatively, the gravity disturbance vector can be obtained by direct differencing between the specific forces measured from INS and the kinematic accelerations derived from GPS (Jekeli, 1992). In this case, the GPS acceleration is used as an update in the estimation of the INS system errors. The precision of GPS positions with current technology is better than ±10 cm and that of the velocity is better than ±1 cm/sec in the post-processing kinematic mode. Since the derived GPS accelerations after low pass filtering with a period of 90 seconds have a precision better than ±1 mGal (Wei and Schwarz, 1995), it can be used to estimate the system errors in the INS. Then, the difference between the GPS acceleration and adjusted INS acceleration would reflect the gravity signal.

The whole schematic procedures of the new acceleration update algorithm are shown in Figure 5.1. Mainly, four principal procedures are involved in this new technique. First, the GPS accelerations are derived from the GPS positions calculated through the DGPS technique by applying a numerical differentiator. In this study, a 5^{th} order B-spline differentiator (de Boor, 1978, p.144) was applied to the GPS positions to obtain the GPS accelerations. Since the numerical differentiation tends to amplify high frequency components, the derived GPS accelerations should be smoothed to

reduce those high frequency effects. For this purpose, a 3rd order B-spline smoother

(*ibid*.) with window length of 60 seconds was applied to the raw GPS accelerations. Secondly, the raw INS data (increments of velocities and angles) are integrated to generate the necessary transformation matrix for the INS accelerations. A third order integration algorithm, using a quaternion approach, was applied for this procedure. The integrated acceleration was also smoothed by the same 3rd order smoother which was applied to GPS acceleration for consistency. Thirdly, Kalman filtering is performed to estimate the INS system errors. Here, the GPS acceleration is used as update value and the residuals from the filter are interpreted as the approximate estimates of the gravity disturbances. Finally, the residuals from three flight lines are processed with WCF (wavenumber correlation filter) to eliminate uncorrected system errors and extract the gravity signals with correlations among the lines. The tolerance of the correlation coefficient applied in this last procedure is zero for extracting frequency components having positive correlation among the lines.

Compared to the traditional approach, this alternative approach is conceptually much simpler because the integration of the navigation equation is not necessary. In addition, the computation in the i-frame makes the Kalman filter equations much simpler so that the computational expenses are less than for the traditional approach. In this case, the gravity is not modeled parametrically, so the dependency on a gravity model is also eliminated in the estimation procedure.

In this chapter, the detailed explanations of the above procedures are presented. Then, the mathematical model and the Kalman filter are verified through simulations based on real dynamics of an aircraft. The results are presented and an analysis of the test flight ends this chapter.

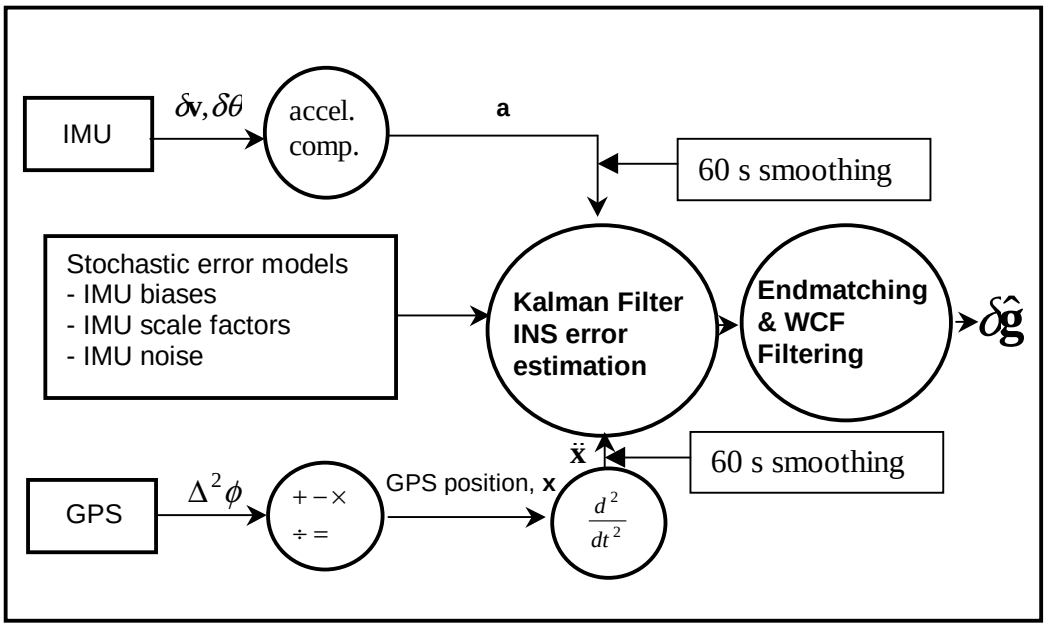

Figure 5.1 Alternative Data Processing for Vector Gravimetry.

5.2 Data Processing

5.2.1 GPS Acceleration

Once the precise GPS positions are calculated using the DGPS technique, a numerical differentiator can be applied twice to get the GPS accelerations. Conventionally, the GPS positions are given in the ECEF coordinate system, so the transformation of the positions from e- to i-frame should be performed before the differentiation. Using the precise GPS positions provided by the University of Calgary (see section 4.5.1), a 5^{th} order B-spline differentiator (de Boor, 1978, p.144) is applied to obtain the GPS accelerations. Because of the characteristics of the numerical differentiation, the derived GPS accelerations show high frequency effects that make the identification of the real motions difficult. Note the four high dynamic peaks caused by the vehicle turns (Figure 5.2).

The dynamics of the vehicle can be seen after applying a low pass filter or smoother to the raw acceleration. Using a B-spline with 60 seconds window length (*ibid.*), the high frequency components in the raw GPS acceleration is smoothed out (Figure 5.3). Note the patterns of oscillations in the y and z components that seem to be associated with the vehicle dynamics. The overall amplitude of the acceleration is in the range of several thousands of mGal excluding the turns.

5.2.2 INS Acceleration

The raw data from the INS system are the increments of the velocities and angles with respect to the i-frame obtained in the b-frame by accelerometers and gyros, respectively. Using those raw data, it is possible to construct the accelerations in an arbitrary frame. Therefore, one has to decide on a frame in which the data are integrated and select a method for the numerical integration. The i-frame and a third order quaternion integration algorithm are selected for this alternative method for their conceptual and numerical simplicity.

Let's consider the output from the IMU, accelerometer and gyro pulses, $\delta\mathbf{v}_l$ and $\delta\theta_l$, respectively; where $\delta\mathbf{v}_l$ is a vector of increments in sensor-frame velocity generated by the three accelerometers and $\delta\theta_l$ is a vector of increments in sensor-frame angles generated by the three gyros at time l. Defining the corresponding time increments, δt, those are written as:

$$\delta\mathbf{v}_l = \int_{\delta t} \mathbf{a}^s(t)dt, \qquad \delta\theta_l = \int_{\delta t} \omega_{is}^s(t)dt, \tag{5.1}$$

where the superscript s means the sensor frame (s-frame). The acceleration in the i-frame can be constructed by applying a transformation that is derived from the orientation information in the $\delta\theta_l$'s to the acceleration in the s-frame calculated from $\delta\mathbf{v}_l$'s.

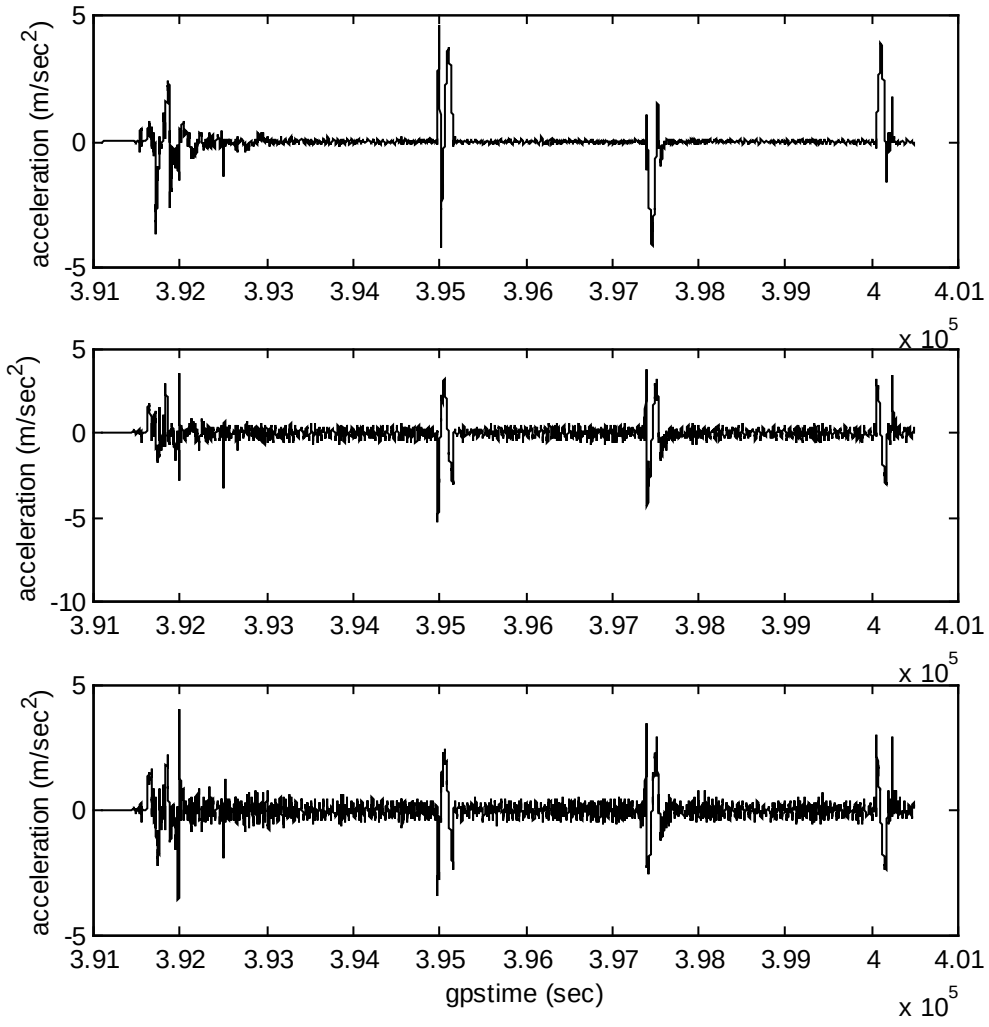

Figure 5.2 The derived GPS accelerations in the i-frame; X (top), Y (middle) and Z (bottom).

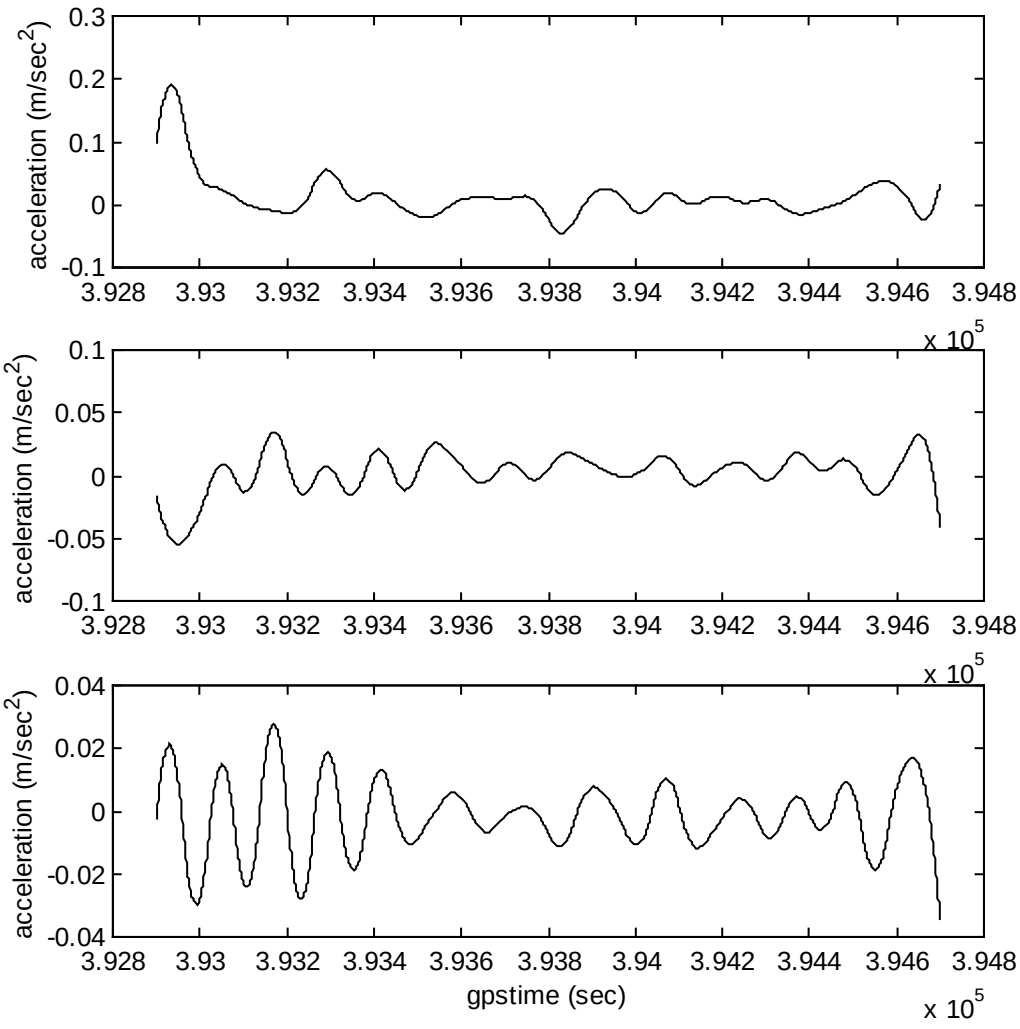

Figure 5.3 GPS acceleration after applying 60 seconds smoothing for line 1; X (top), Y (middle) and Z (bottom).

The transformation matrix from s- to i-frame can be constructed by integrating the differential equation (2.46).

$$\dot{C}_s^i = C_s^i \Omega_{is}^s \tag{5.2}$$

As stated in section 2.4.3, the equivalent differential equation can be derived in terms of quaternions (see 2.50, 2.53-2.55).

$$\dot{\mathbf{q}} = \frac{1}{2} A \mathbf{q} \tag{5.3}$$

where A is a 4×4 skew-symmetric matrix of time dependent angular rates:

$$A = \begin{bmatrix} 0 & \omega_1 & \omega_2 & \omega_3 \\ -\omega_1 & 0 & \omega_3 & -\omega_2 \\ -\omega_2 & -\omega_3 & 0 & \omega_1 \\ -\omega_3 & \omega_2 & -\omega_1 & 0 \end{bmatrix} \tag{5.4}$$

Using (5.3), one can integrate $\mathbf{q}$ over a certain time interval δt, then the element in the transformation matrix C_s^i can be obtained according to (2.36).

One of the popular numerical integration algorithms is the Runge-Kutta algorithm that is known to be very stable and to have much flexibility. It imitates the Taylor series method without requiring the analytic differentiation of the original differential equation (Cheney and Kincaid, 1996, p. 581). A third order Runge-Kutta algorithm is selected to perform the numerical integration for the quaternions. Since it requires that the function being integrated is evaluated at either end of the integration interval and half-way in between, the integration interval is twice the data interval.

$$\Delta t = 2\delta t \tag{5.5}$$

Now, let's assume that the angular rate $\omega \equiv \omega_{is}^s$ is expressed as:

$$\omega(t) = \omega_{l-2} + \dot{\omega}_{l-2}(t - t_{l-2}) + O(\Delta t^2); \ \left| t - t_{l-2} \right| \le \Delta t, \tag{5.6}$$

where the subscripts denote the time index for evaluation of the quantity at the corresponding epochs spanning intervals δt.

With (5.6) and (5.1),

$$\delta\theta_{l-1} = \int_{t_{l-2}}^{t_{l-1}} \omega(t')dt' = \omega_{l-2}\delta t + \frac{1}{2}\dot{\omega}_{l-2}\delta t^2 + O(\Delta t^3) \tag{5.7}$$

$$\delta\theta_l = \int_{t_{l-1}}^{t_l} \omega(t')dt' = \omega_{l-2}\delta t + \frac{3}{2}\dot{\omega}_{l-2}\delta t^2 + O(\Delta t^3) \tag{5.8}$$

Solving for ω_{l-2} and $\dot{\omega}_{l-2}$;

$$\omega_{l-2} = \frac{1}{2\delta t}(3\delta\theta_{l-1} - \delta\theta_l) + O(\Delta t^2) \tag{5.9}$$

$$\dot{\omega}_{l-2} = \frac{1}{\delta t^2}(\delta\theta_l - \delta\theta_{l-1}) + O(\Delta t) \tag{5.10}$$

Substituting (5.9) and (5.10) into (5.6) with specified variable t yields:

$$\omega_{l-2}\Delta t = 3\delta\theta_{l-1} - \delta\theta_l + O(\Delta t^3) \tag{5.11}$$

$$\omega_{l-1}\Delta t = \delta\theta_{l-1} + \delta\theta_l + O(\Delta t^3) \tag{5.12}$$

$$\omega_l \Delta t = 3\delta\theta_l - \delta\theta_{l-1} + O(\Delta t^3) \tag{5.13}$$

Therefore, these observed quantities are accurate up to the second order:

$$\hat{\omega}_{l-2} \Delta t = 3\delta\theta_{l-1} - \delta\theta_l \tag{5.14}$$

$$\hat{\omega}_{l-1} \Delta t = \delta\theta_{l-1} + \delta\theta_l \tag{5.15}$$

$$\hat{\omega}_l \Delta t = 3\delta\theta_l - \delta\theta_{l-1} \tag{5.16}$$

Now, the third-order R.K. algorithm for $\dot{\mathbf{q}} = f(\mathbf{q}, t)$ is given by

$$\hat{\mathbf{q}}_l = \hat{\mathbf{q}}_{l-2} + \frac{1}{6}(\Delta\mathbf{q}_0 + 4\Delta\mathbf{q}_1 + \Delta\mathbf{q}_2), \tag{5.17}$$

where

$$\Delta\mathbf{q}_0 = f(\hat{\mathbf{q}}_{l-2}, t_{l-2})\Delta t \tag{5.18}$$

$$\Delta\mathbf{q}_1 = f(\hat{\mathbf{q}}_{l-2} + \frac{1}{2}\Delta\mathbf{q}_0, t_{l-1})\Delta t \tag{5.19}$$

$$\Delta\mathbf{q}_2 = f(\hat{\mathbf{q}}_{l-2} + 2\Delta\mathbf{q}_1 - \Delta\mathbf{q}_0, t_l)\Delta t \tag{5.20}$$

With an initial value, (5.17) provides quaternions at intervals of Δt for the desired transformation from the s- to the i-frame.

Considering (5.3) with $f(\mathbf{q}, t) = A(t)\frac{\mathbf{q}}{2}$ and defining $\hat{B}_l = \hat{A}_l \Delta t$, one can express the iteration formula (5.17) in terms of the matrix $\hat{B}$.

$$\Delta\mathbf{q}_0 = \frac{1}{2}\hat{B}_{l-2}\hat{\mathbf{q}}_{l-2} \tag{5.21}$$

$$\Delta\mathbf{q}_1 = \frac{1}{2}\hat{B}_{l-1}\left(I + \frac{1}{4}\hat{B}_{l-2}\right)\hat{\mathbf{q}}_{l-2} \tag{5.22}$$

$$\Delta\mathbf{q}_2 = \frac{1}{2}\hat{B}_l\left[I + \hat{B}_{l-1}\left(I + \frac{1}{4}\hat{B}_{l-2}\right) - \frac{1}{2}\hat{B}_{l-2}\right]\hat{\mathbf{q}}_{l-2} \tag{5.23}$$

After substituting these into (5.17), the final iteration equation for quaternions is given by

$$\hat{\mathbf{q}}_l = \left[I + \frac{1}{12}\left(\hat{B}_l + 4\hat{B}_{l-1} + \hat{B}_{l-2}\right) + \frac{1}{12}\left(I + \frac{1}{4}\hat{B}_l\right)\hat{B}_{l-1}\hat{B}_{l-2} + \frac{1}{12}\hat{B}_l\left(\hat{B}_{l-1} - \frac{1}{2}\hat{B}_{l-2}\right)\right]\hat{\mathbf{q}}_{l-2} \tag{5.24}$$

The accuracy of the above equation is up to the third-order yielding the fourth order error.

The initial value of the above equation can be obtained from the initialization process of the IMU, or from a ZUPT algorithm in the Kalman filter. Once the initial matrix is obtained, the inverse relationship of (2.36) can be used to get the initial elements for the quaternion:

$$a = \frac{1}{2}\left(1 + \left(C_s^i\right)_{1,1} + \left(C_s^i\right)_{2,2} + \left(C_s^i\right)_{3,3}\right)^{1/2} \tag{5.25}$$

$$b = \frac{1}{4a}\left(\left(C_s^i\right)_{2,3} - \left(C_s^i\right)_{3,2}\right) \tag{5.26}$$

$$c = \frac{1}{4a}\left(\left(C_s^i\right)_{3,1} - \left(C_s^i\right)_{1,3}\right) \tag{5.27}$$

$$d = \frac{1}{4a}\left(\left(C_s^i\right)_{1,2} - \left(C_s^i\right)_{2,1}\right) \tag{5.28}$$

Having quaternions to represent the rotational information, one can compute the transformation matrix from s-frame to i-frame and get the acceleration in the i-frame by applying the transformation to the acceleration in the s-frame. For the acceleration in the s-frame, one can use the first-order calculation as follows:

$$\hat{\mathbf{a}}_l^s = \frac{1}{2\delta t}(\delta \mathbf{v}_{l+1} + \delta \mathbf{v}_l) \tag{5.29}$$

Figure 5.4 shows the INS acceleration integrated using the algorithm explained above. Comparing it with the GPS acceleration (Figure 5.2), one can notice similarities in shorter-wavelength characteristics and differences in the global trends. As in case of GPS acceleration, the same 3rd order B-spline filter (60-s averaging) was applied to INS acceleration to reduce the high frequency components (Figure 5.5).

While the high frequency noise, mostly coming from the accelerometer white noise, is eliminated, the slope trends in the x and y components still remain. Note the magnitudes of the INS accelerations. These are caused by the gravitational acceleration ($\approx 9.8\,\mathrm{m/sec^2}$ in the down component) distributed in all three axes in the i-frame.

Using GPS positions, the smoothed accelerations of the GPS and INS can be transformed into the n-frame. Figure 5.6 presents the difference between those two accelerations in the n-frame for all three lines. In an ideal situation, this should be the gravity disturbance vector according to the fundamental equation. The results, however, have still some systematic errors like global trends in horizontal components. It should be emphasized that the line 2 has the opposite systematic errors to the line 1 and 3 in the horizontal components. Note the high frequency oscillation in the north component. Because the airplane mainly flew in the E-W direction, the roll motions of the vehicle directly affect the acceleration of the north component. Those high frequency oscillations are considered as effects from the dynamics of the aircraft, called phugoid motion (Boedecker and Neumayer, 1994).

As one can see, just taking direct differences between the GPS and INS accelerations already shows the signature of the gravity. Especially, the down component signal is very well detected; for example, look at the low anomaly around $\lambda = 242.9^\circ$ and the high anomaly around $\lambda = 241.4^\circ$. Since the down component is not much affected by the orientation errors, it does not have a significant global trend.

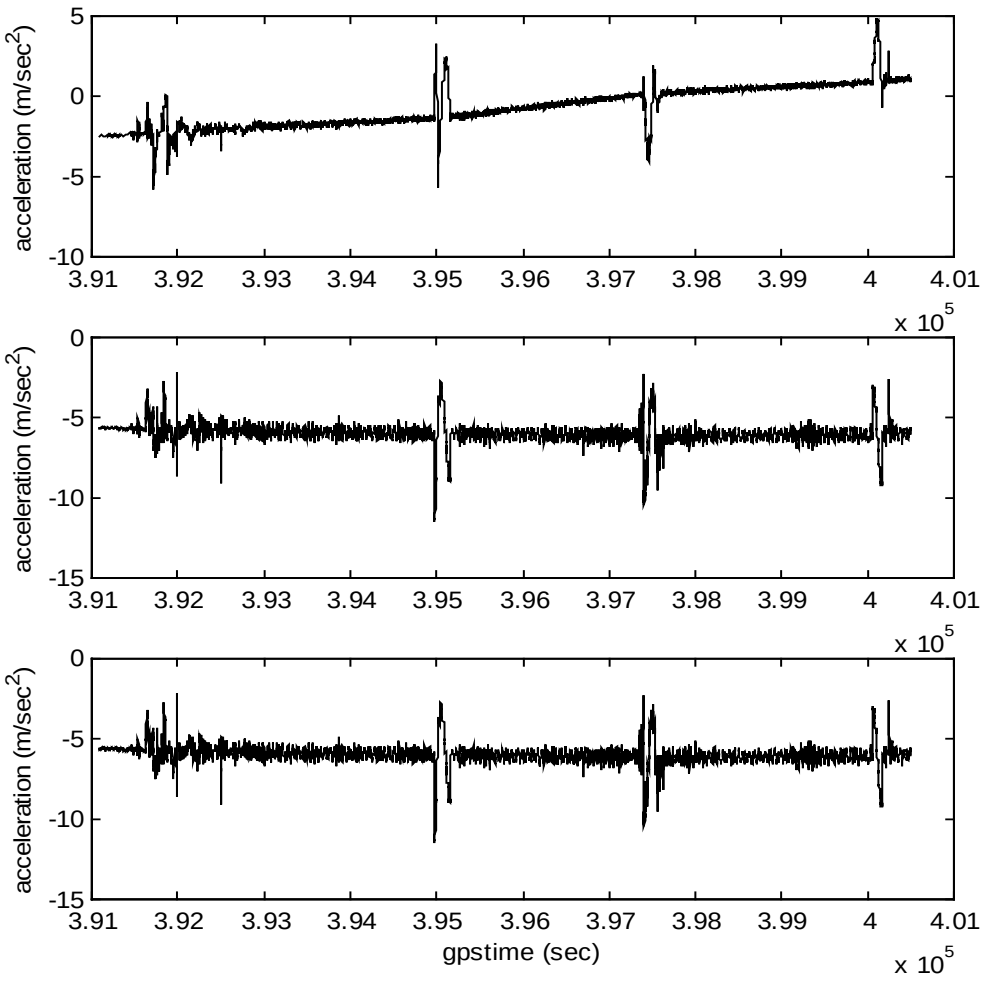

Figure 5.4 The integrated INS acceleration in the i-frame; x (top), y (middle) and z (bottom).

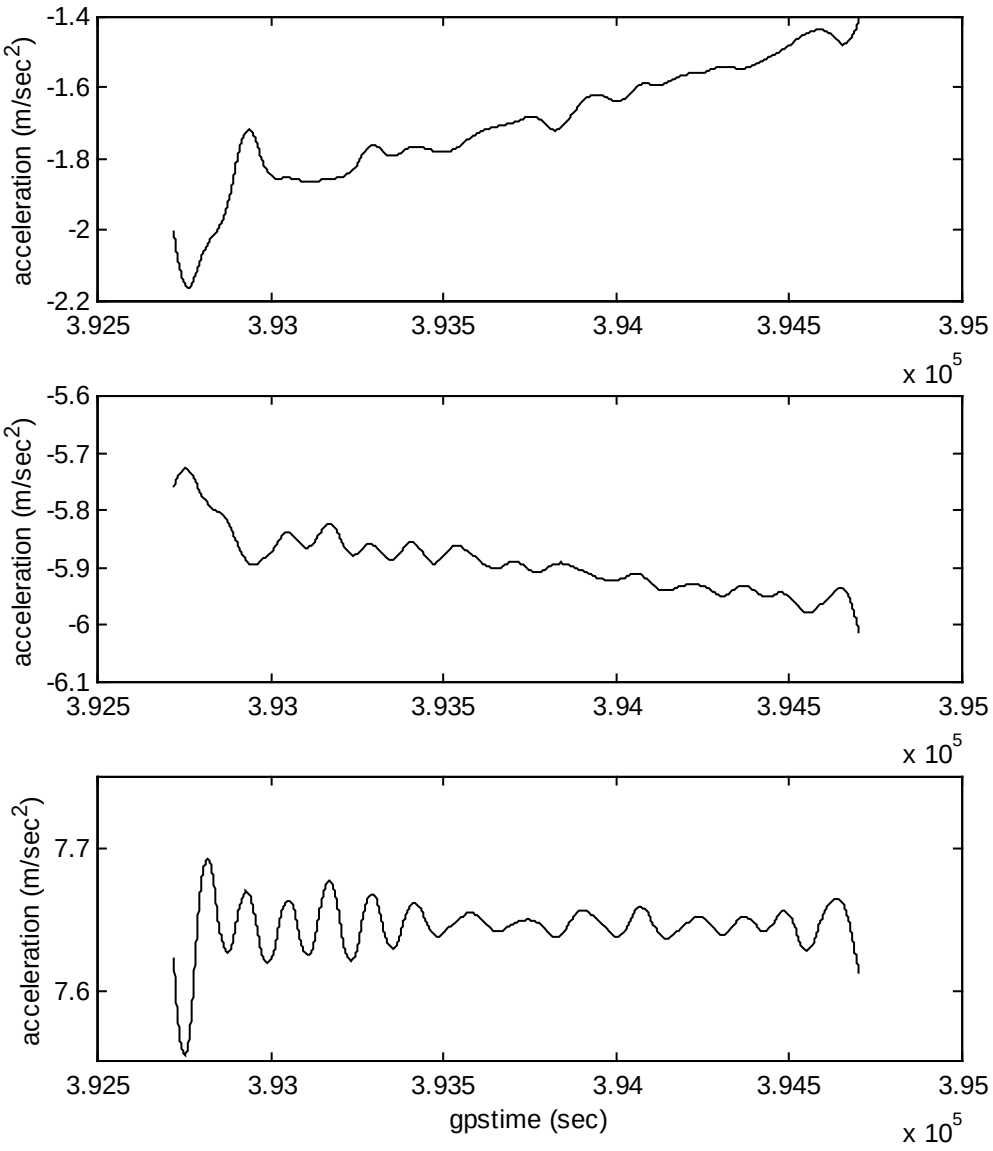

Figure 5.5 INS acceleration in i-frame after applying 60 seconds smoothing for line 1; X (top), Y (middle) and Z (bottom).

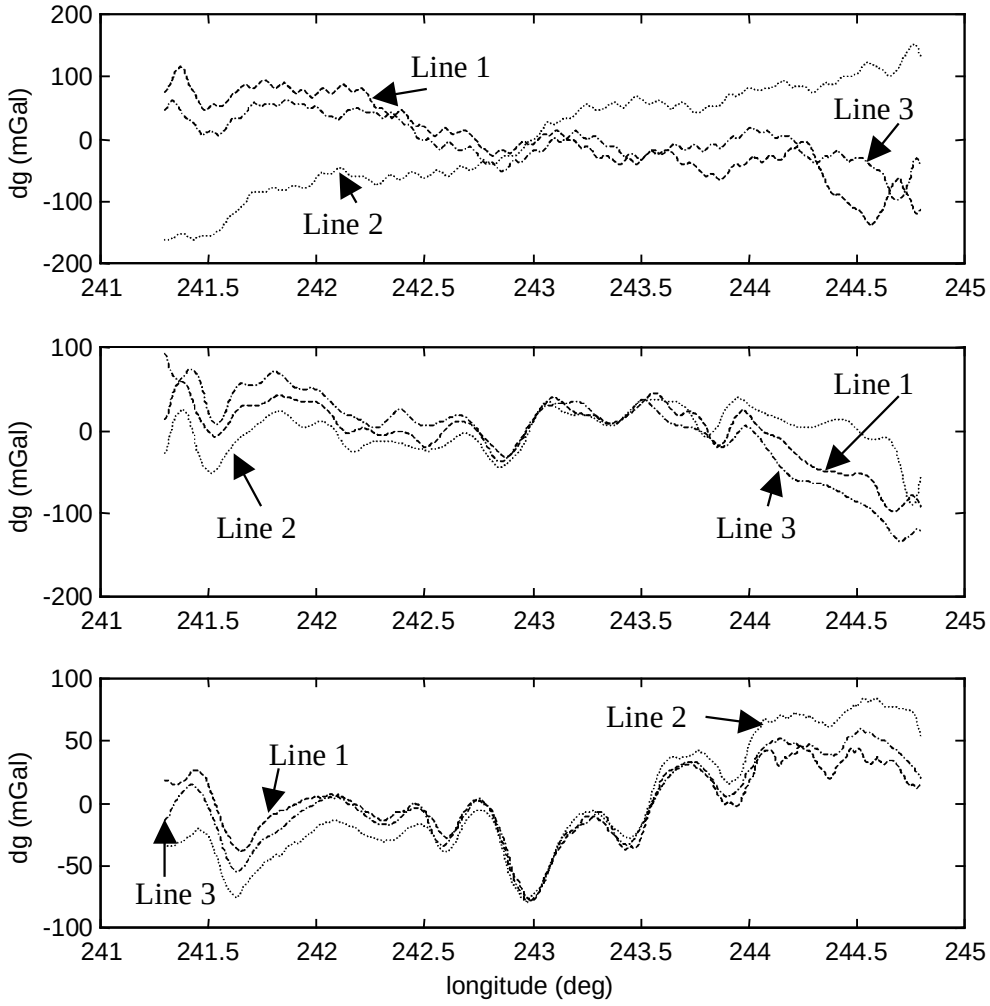

Figure 5.6 Difference between the smoothed GPS and INS acceleration in n-frame for line 1 (dashed), line 2 (dotted), and line 3(dash-dotted) ; North (top), East (middle) and Down (bottom).

5.2.3 Kalman Filtering Using GPS Acceleration Update

In the previous section, the gravity signal has been already exposed, more or less, after the direct differencing between the GPS and INS accelerations. The global trends which appear in the horizontal components are assumed to be the effect of orientation error and the gyro drift that cannot be eliminated by smoothing or low pass filtering. Therefore, it is necessary to develop a proper mathematical model from which the INS system error could be estimated and subsequently removed.

Again, the mathematical model for the new acceleration update algorithm starts from the fundamental equation (2.6). It should be noted that the fundamental equation is given in terms of acceleration, not position. Since we are seeking gravitation, the approach using accelerations is more straightforward than using position as in the traditional approach.

The fundamental equation (2.6) can be expressed by observed accelerations of GPS and INS:

$$\tilde{\ddot{\mathbf{x}}}^{i} - \delta\ddot{\mathbf{x}}^{i} = \tilde{\mathbf{a}}^{i} - \delta\mathbf{a}^{i} + \mathbf{g}^{i}, \tag{5.30}$$

where the superscript i denotes the inertial frame; $\tilde{\ddot{\mathbf{x}}}^{i}$ is the GPS observed acceleration; $\tilde{\mathbf{a}}^{i}$ is the INS observed specific force; $\mathbf{g}^{i}$ is the gravitation; $\delta\ddot{\mathbf{x}}^{i}, \delta\mathbf{a}^{i}$ are the total errors for the GPS and INS observed acceleration, respectively, interpreted as random effects.

The error of the kinematic accelerations from GPS is assumed to be white noise, and the same INS error model as in the traditional case is considered (see (3.23) and (3.24)). The accelerometer error $\delta\mathbf{a}^{i}$ can be expressed in terms of the error in the body frame (b-frame) and the orientation error (see (4.6)):

$$\delta\mathbf{a}^{i} = C_{b}^{i}\delta\mathbf{a}^{b} + \tilde{\mathbf{a}}^{i} \times \psi^{i}, \tag{5.31}$$

where C_{b}^{i} is the transformation matrix from body to inertial frame, $\delta\mathbf{a}^{b}$ is the accelerometer error in the body frame and ψ^{i} is the orientation error in the inertial frame. Including only the general error parameters, the accelerometer and gyro errors in the body frame are modeled as follows:

$$\delta\mathbf{a}^{b} = \mathbf{b}_{a} + \mathbf{k}_{a}\mathbf{a}^{b} + \varepsilon_{a}, \tag{5.32}$$

$$\delta\omega_{ib}^{b} = \mathbf{b}_{g} + \mathbf{k}_{g}\omega_{ib}^{b} + \varepsilon_{g}, \tag{5.33}$$

where $\mathbf{b}_{a}$ and $\mathbf{b}_{g}$ are biases (random effects); $\mathbf{k}_{a}$ and $\mathbf{k}_{g}$ are scale factor errors; ε_{a}, ε_{g} represent the white noise; and $\delta\omega_{ib}^{b}$ is the gyro error in the body frame. The subscript 'a' refers to the accelerometer while 'g' refers to the gyro.

With (5.33), the dynamics of the orientation error ψ^{i} are given as follows:

$$\dot{\psi}^{i} = -C_{b}^{i}\delta\omega_{ib}^{b} = -C_{b}^{i}\mathbf{b}_{g} - C_{b}^{i}[\omega_{ib}^{b}]\mathbf{k}_{g} - C_{b}^{i}\varepsilon_{g}, \tag{5.34}$$

where $[\omega_{ib}^{b}]$ is the diagonal matrix that contains the angular rates of body frame rotation with respect to the inertial frame.

Using equation (5.34) and the models for the random parameters associated with the INS, the error dynamics equation can be set up as follows.

$$\begin{bmatrix} \dot{\mathbf{b}}_a \\ \dot{\mathbf{b}}_g \\ \dot{\mathbf{k}}_a \\ \dot{\mathbf{k}}_g \\ \dot{\psi} \end{bmatrix} = \begin{bmatrix} 0 & 0 & 0 & 0 & 0 \\ 0 & 0 & 0 & 0 & 0 \\ 0 & 0 & 0 & 0 & 0 \\ 0 & 0 & 0 & 0 & 0 \\ 0 & -C_b^i & 0 & -C_b^i[\omega_{ib}^b] & 0 \end{bmatrix} \begin{bmatrix} \mathbf{b}_a \\ \mathbf{b}_g \\ \mathbf{k}_a \\ \mathbf{k}_g \\ \psi \end{bmatrix} + \begin{bmatrix} 0 & 0 & 0 & 0 & 0 \\ 0 & 0 & 0 & 0 & 0 \\ 0 & 0 & 0 & 0 & 0 \\ 0 & 0 & 0 & 0 & 0 \\ 0 & 0 & 0 & 0 & -C_b^i \end{bmatrix} \begin{bmatrix} 0 \\ 0 \\ 0 \\ 0 \\ \varepsilon_g \end{bmatrix} \tag{5.35}$$

Note that biases and scale factors are modeled as random effects, i.e. parameters for which stochastic prior information is assumed.

After some manipulations with proper substitutions, the equation (5.30) can be expressed as:

$$\tilde{\ddot{\mathbf{x}}}^i - \tilde{\mathbf{a}}^i - \mathbf{g}^i = -C_b^i \mathbf{b}_a - C_b^i[\tilde{\mathbf{a}}^b]\mathbf{k}_a - \tilde{\mathbf{a}}^i \times \psi^i - C_b^i \varepsilon_a + \delta\ddot{\mathbf{x}}^i, \tag{5.36}$$

where $[\tilde{\mathbf{a}}^b]$ is the diagonal matrix that contains measured accelerations in the body frame. The gravitation vector $\mathbf{g}^i$ can be expressed as the sum of the normal gravitation vector γ_n^i and the gravity disturbance vector $\delta\mathbf{g}^i$ in the inertial frame. Therefore, in theory, one has to mathematically model the gravity disturbance vector $\delta\mathbf{g}^i$ to obtain the estimates. As described in Chapter 1, however, the modeling of the disturbing gravity field is very controversial in the field of geodesy. Furthermore, none of the mathematical models for the gravity perfectly represents the actual gravity field. Therefore, as a result of not knowing the gravitation vector $\mathbf{g}^i$, it can be approximated by the normal gravitation vector γ_n^i of a selected ellipsoid (e.g. GRS80; Moritz, 1992). Now, expressing the gravitation as the sum of the normal gravitation and gravity disturbances, the equation (5.36) is changed as:

$$\tilde{\ddot{\mathbf{x}}}^i - \tilde{\mathbf{a}}^i - \gamma_n^i = -C_b^i \mathbf{b}_a - C_b^i[\tilde{\mathbf{a}}^b]\mathbf{k}_a - \tilde{\mathbf{a}}^i \times \psi^i - C_b^i \varepsilon_a + \delta\ddot{\mathbf{x}}^i + \delta\mathbf{g}^i. \tag{5.37}$$

Note that the left side is composed of observations (GPS, INS accelerations) and a calculated quantity (normal gravity), while the right side contains unknowns treated as random parameters and white noises, plus the gravity disturbance.

Clearly, the equation (5.37) would contain a model error when omitting the gravity disturbance vector $\delta\mathbf{g}^i$. The main idea of this approach is that the effect of the non-random gravity disturbance is largely reflected in the residuals after the adjustment via Kalman filter. To investigate this effect in detail, let us set up the explicit form of the Kalman filtering observation equations using the equations (5.37).

$$\mathbf{z} := \tilde{\ddot{\mathbf{x}}}^i - \tilde{\mathbf{a}}^i - \gamma_n^i \tag{5.38}$$

$$\mathrm{H} := \begin{bmatrix} -C_b^i & 0 & -[\tilde{\mathbf{a}}^i]C_b^i & 0 & [\tilde{\mathbf{a}}\times] \end{bmatrix} \tag{5.39}$$

$$\mathbf{x} := \begin{bmatrix} \mathbf{b}_a^T & \mathbf{b}_g^T & \mathbf{k}_a^T & \mathbf{k}_g^T & \psi^T \end{bmatrix}^T \tag{5.40}$$

$$\mathbf{v} = (-C_b^i \varepsilon_a + \delta\ddot{\mathbf{x}}^i) + \delta\mathbf{g}^i \tag{5.41}$$

Note that each component in the H matrix is a 3×3 matrix and in $\mathbf{x}$ it is a 3×1 vector. So now, we have a 15-state system, and the observation is the difference of acceleration vectors, not of the positions. Again, the initial conditions for the states

would be obtained from the manufacturer's specification or from controlled experiments.

The Kalman filter for the above model (5.35) through (5.41) generates the residual, $\tilde{\mathbf{v}}$, containing the adjusted observation errors (i.e. the difference between the observations, **z**, and the adjusted observations as modeled $H\hat{\mathbf{x}}$) which represents – in large parts – the estimated gravity disturbance vector. Therefore, if the part $(-C_b^i \varepsilon_a + \delta\ddot{\mathbf{x}}^i)$ can be assumed considerably small, having random characteristics, and if the total difference of the observations and adjusted observations, $\mathbf{z} - H\hat{\mathbf{x}}$, has distinguished characteristics with respect to the gravity signature, the residual vector will be a good approximation for the gravity disturbance vector.

In summary, the two approaches differ as follows:

Method 1 (Traditional Method):

- Integrate INS acceleration and estimate INS system errors using updates from GPS position.
- Treat δg_N and δg_E as stochastic parameters.
- Calculation is performed in n-frame.
- Vertical gravity disturbance cannot be estimated.

Method 2 (New Algorithm):

- Differentiate GPS positions and use in combination with INS acceleration as observation update to estimate orientation and other INS errors.
- Include $\delta\mathbf{g}$ as the main portion in the total random error budget and analyze the residuals after the adjustment with respect to this characteristics.
- Calculation is performed in i-frame.
- Total vector, $\delta\mathbf{g}$, can be determined.

Note that one could also include $\delta\mathbf{g}$ in the total random error budget for Method 1. Again, one would then expect to see an effect in the residuals of the observations. But these are residuals in position, not acceleration, and it would be virtually impossible to extract the gravity disturbance from them.

5.2.4 WCF

In the previous section, it is explained that the residual vector from the Kalman filter would be at least an approximation of the estimated gravity disturbance vector under the condition of $(-C_b^i \varepsilon_a + \delta\ddot{\mathbf{x}}^i)$ being small, and distinguishable characteristics in the difference between the observations and the adjusted observations. Otherwise, the signal, the gravity disturbance in this case, might still be extracted using WCF. As explained in section 4.5.2, the observations of overlapping or almost parallel lines are required to apply WCF. In addition, it would be better if those lines represent flights in opposite directions to remove the uncompensated system errors.

5.3 Simulation based on the Real Dynamics

To verify the developed algorithm as well as to investigate the behavior of the INS system errors, it is necessary to perform a simulation based on the real dynamics. Although Wei and Schwarz (1994) have carried out a similar simulation, its primary assumption was the local level flight. Therefore, the effect of the vehicle dynamics was not characterized at all, although major features in the INS errors were well investigated. So, this section focuses on a numerical investigation of the INS error model in a real dynamics situation. In addition, this will determine if the developed INS error model and Kalman filtering are appropriate for the GPS/INS airborne vector gravimetry.

5.3.1 Establishing Simulation Data

To simulate the real dynamics of an airborne gravimetry mission, the GPS position data for the June 1995 test flight over the Rocky Mountains were chosen as the base data. In addition, the attitude estimates from the University of Calgary and gravity information from Calgary as well as NIMA data were also used to simulate the IMU sensor data.

The procedure used in this study to conduct the simulation is as follows.

1. Section extraction from GPS position data. GPS position data at GPS seconds from $t = 395200$ to $t = 397200$ corresponding to Line 2 are extracted.
2. Interpolate GPS 2 Hz position data to 50 Hz data. A cubic spline interpolator is used.
3. Compute GPS acceleration by numerical differentiation in the inertial frame. A B-spline differentiation with 1-second intervals of smoothing was performed.
4. Simulate gravitation data at each observation position by interpolation of the gravity information from NIMA and Calgary.
5. Compute transformation matrices C_n^i and C_b^i using attitude and position.
6. Simulate errorless INS accelerometer and gyro raw data.

$$\mathbf{a}^b = C_i^b(\ddot{\mathbf{x}}^i - C_n^i\mathbf{g}^n) \tag{5.42}$$

$$\omega_{ib}^b = \frac{1}{\delta t}\left[I - C_i^b(t)C_b^i(t-\delta t)\right] \tag{5.43}$$

7. Integrate the simulated INS raw data to get INS acceleration and assume it as true INS acceleration. Because of numerical round-off error, the simulated INS raw data do not correspond to the original GPS acceleration and gravitation data.
8. Simulated GPS accelerations by taking the difference between the gravitation and INS accelerations.

As indicated in steps 7 and 8, INS accelerations should be assumed as true values because of the round-off error in the procedure of making INS raw data. So, the simulated GPS acceleration of step 8 does not exactly match with the original position-derived acceleration. In other words, the GPS position integrated from the

simulated GPS acceleration is not the same as the original GPS position.

The position data, however, are only used for the calculation of the normal gravitation and the transformation matrix from navigation to inertial frame, C_n^i, in the Kalman filter. So, by using the original GPS position data and simulated GPS and INS acceleration, a near-perfect gravitational signal can be obtained.

5.3.2 Numerical Test for each INS Error Parameter

Because perfect simulated GPS and INS data are available, artificial systematic errors for each INS error parameter such as biases, scale factor errors, and initial orientation errors can be added to the raw simulated INS data. After integrating the IMU data, one can see the effect of the added errors to the INS acceleration, and the error parameters will be determined through the Kalman filter. For the magnitude of error parameters, the specification for the Litton LN93 INS were used (Table 5.1). The initial variance of an error parameter is set to the square of the intentionally added error for the parameter; and the variances of other parameters are set to zero to see the effect of just one error.

	Bias Error	Scale Factor Error	White Noise
Accelerometer	±20 mGal	±40 ppm	$\pm 5\,\text{mGal}/\sqrt{\text{Hz}}$
Gyro	$\pm 0.003^o$/hr	±0.2 ppm	$< \pm 0.001^o/\sqrt{\text{hr}}$

Table 5.1. The Error Specification for the LN 93 INS

5.3.2.1 Accelerometer Bias

Figure 5.7 shows the true gravity disturbance, the observations (GPS acceleration-INS acceleration-Normal gravity) and the residuals from Kalman filtering after 20 mGal of constant accelerometer bias is added to the simulated INS raw data for all three axes. As one can expect, the bias appears in the observations on each axis. The bias, however, does not appear as a constant in the navigation frame. That is, although the bias is a constant in the body frame, it is affected by the vehicle motion and then is not constant in the navigation frame. In fact, the bias effect is varying up to 1.5 mGal depending on the dynamics in this case.

The residuals out of the Kalman filter show that the filter is stabilized in the down direction within 120 seconds while the east and north components take more time. The residuals after stabilization, however, are not close to zero but have a systematic appearance with substantial high-frequency undulations in the north component. This can be explained by the high-dynamics of the vehicle and

mismodeling effects. In other words, if the model is correct, the residuals should be close to zero without any systematic appearances. Furthermore, the estimates for the bias should be 20 mGal. This can be tested, by taking out the simulated gravitation from the observation vector, generating the observation vector as purely a constant of 20 mGal in each axis in the body frame. Using $\mathbf{g}^i$ instead of γ^i, the resulting estimation indicated that the accelerometer biases are well determined as expected. The filter estimates the biases as 20 mGal for all axes at the first epoch. If normal gravitation is used instead of true gravitation, however, a mismodeling effect is included; hence, the estimates for the biases are also changed. By ignoring the gravity disturbances from the parametric model, the effect is nevertheless included in the observation error represented as random with mean of zero. The simulated gravity disturbances, however, are not random white noise and their mean is not zero. Therefore, the filter attempts to change the bias estimates to match the observations under the maximum allowance of the covariance to make the residuals as small as possible.

Note that the residuals of the down component are decreasing continuously comparing with the control data. This is caused by the increasing tendencies at the down component which causes the estimates of the bias for the down component to be as large as 120 mGal. The dynamics of the roll with an amplitude of 5 degree (see Figure 4.4) coupled with the down component's wrong bias estimates of 120 mGal caused the high frequency anomalies up to 10 mGal in the north component.

5.3.2.2 Accelerometer Scale Factor Error

Figure 5.8 shows the effect of an accelerometer scale factor error of ±40 ppm. As for the case of accelerometer bias, high frequency effects appear in the horizontal components with standard deviations of ±1.11 mGal for north and ±0.15 mGal for east. Note that the scale error effect for the down component appears as a bias of 40 mGal ($40 \times 10^{-6} \times g \approx 40$) because the down component is rather insensitive to the horizontal motions. The residuals from the Kalman filter have a lot of high frequency content showing that the filter tries to compensate the gravity effect with a scale factor error.

5.3.2.3 Gyro bias

Figure 5.9 shows the effect of a gyro bias of 0.003 deg/hr. The observation shows almost linear trends generating errors up to 25 mGal for north and 30 mGal for east with respect to the control data at the end of the line. In addition, high frequency errors in the horizontal components also appear in the observation. Especially, the high frequency in the east component of the observation is caused by the airplane dynamics (roll) since the orientation errors caused by the gyro bias are coupled with the down acceleration and thus affect the horizontal components as seen in equation (4.47).

The down component, however, does not have an overall trend because of its insensitivity to the orientation error. In addition, the standard deviation of the down

component with respect to the control data is relatively small (±0.45 mGal) compared to the horizontal components (±7.5 and ±8.6 mGal for north and east, respectively).

The differences between the residuals and the true values show that the filter is not stabilized in the horizontal components for the first 400 seconds because of the mismodeling effect. The standard deviations of the observations and residuals with respect to the control data after the first 400 seconds (respectively, ±5.8, ±4.1 mGal for north; ±6.9, ±5.1 mGal for east; ±0.5, ±0.4 mGal for down) indicate that the filter successfully removes the overall trends from the observations.

5.3.2.4 Gyro Scale Factor Error

The effect of a gyro scale factor error of ±0.2 ppm on the INS acceleration is very small (less than the standard deviation of ±0.01mGal with respect to the control data) for all three components, like the accelerometer scale factor error in horizontal components (Figure 5.10). The residuals as estimates of the gravity disturbance, however, show high frequency errors in the north component and low frequency errors in the east. The standard deviations for the residuals relative to the control data are ±4.2, ±2.7, ±0.2 mGal for north, east, and down, respectively. Basically, this means that the gyro scale factor error is not really estimated by the Kalman filter.

5.3.2.5 Initial Orientation Error

Figure 5.11 shows the effect of an initial misalignment of +2 arc-second in the horizontal and +2 arc-minute in the vertical, respectively. In the observation, the linear trend is shown in north direction (error of 60 mGal at the end of line) while the east component contains very large high frequency errors up to the amplitude of 25 mGal.

The north orientation error and high dynamics coupled with the down acceleration caused the dominant high frequency error in the east component. In contrast, the east orientation error with less dynamics caused a low-frequency trend in the north component. The standard deviations of the observations and residuals with respect to the control data shows that the filter is very effective in removing the orientation error (respectively, ±17, ±5.2 mGal for north; ±13.7, ±4.9 mGal for east; ±1.2, ±0.3 mGal for down). As one can see from the figure, the mean of the observations and residuals relative to the control data also shows significant reduction of orientation error is achieved through the filter (respectively, 42.9, –9.9 mGal for north; 11.5, 2.8 mGal for east; 0.07, 0.0 mGal for down).

5.3.2.6 Including All Error Parameters

Figure 5.12 shows the joint effect on the observation of all error parameters explained up to now. The simulated observations have long term errors caused by the initial orientation error and gyro biases as well as high frequency components caused by

scale factor errors. It should be mentioned that one has to be careful in establishing the parameter vectors in the estimation procedure. In other words, we know that some error parameters like accelerometer and gyro scale factor errors cannot be readily estimated through the filter, so it is natural to exclude those from the error parameter vector. One way to determine the optimal set of meaningful error parameters is to make a test of different combinations of the parameters and compare the results with the control values.

From intensive tests, the best results from the Kalman filter were obtained (Table 5.2), when the only error parameter considered was the orientation error (see also Figure 5.12). Thus, the overall trends caused by orientation error have been effectively removed through filtering.

	Mean (mGal)	Standard Deviation (mGal)
North	-4.25	±5.88
East	5.87	±7.55
Down	19.32	±0.78

Table 5.2 Estimated mean and standard deviation of the difference between the true gravity disturbance and the residual from the filter (with only orientation errors as system error parameters).

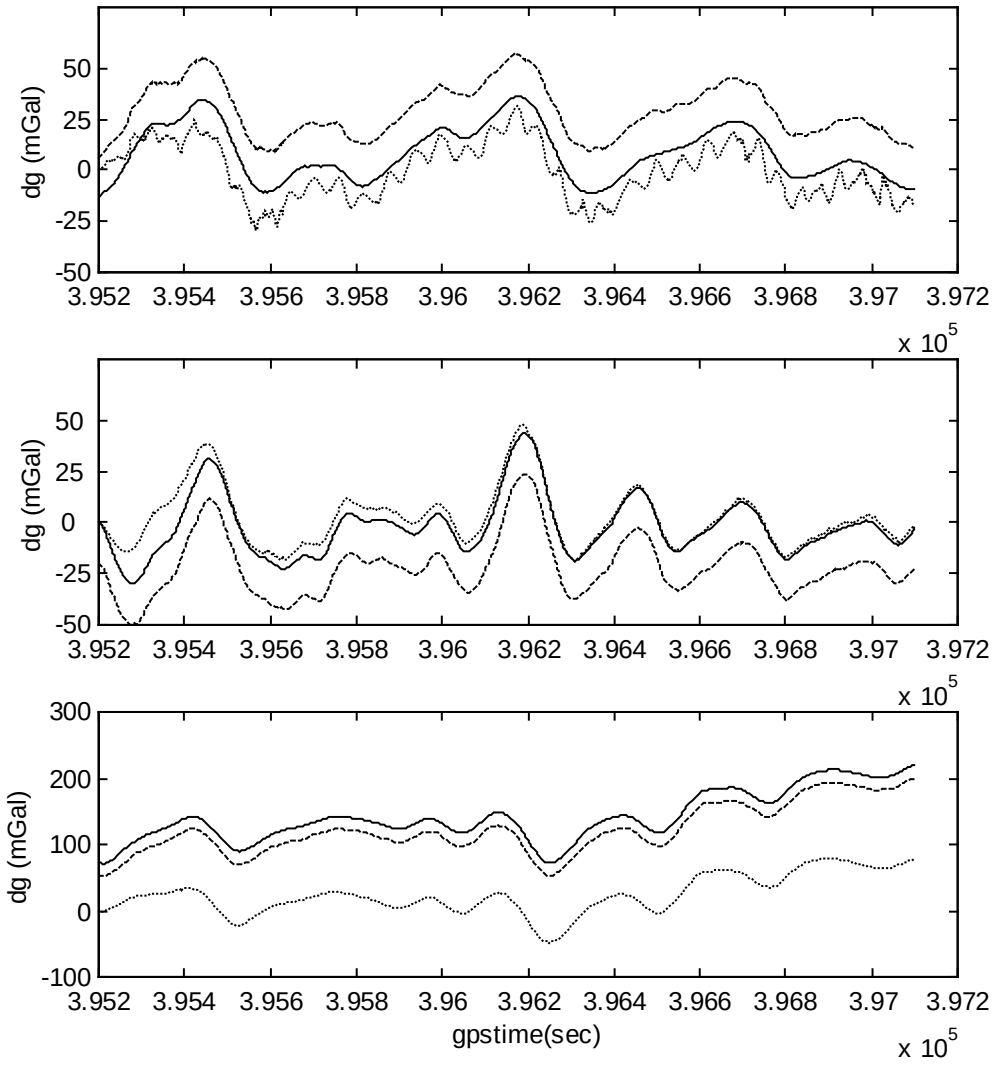

Figure 5.7 Control data (solid), observations (dashed) after adding 20 mGal of accelerometer bias, and residuals (dotted) from the Kalman filter for north (top), east (middle) and down (bottom).

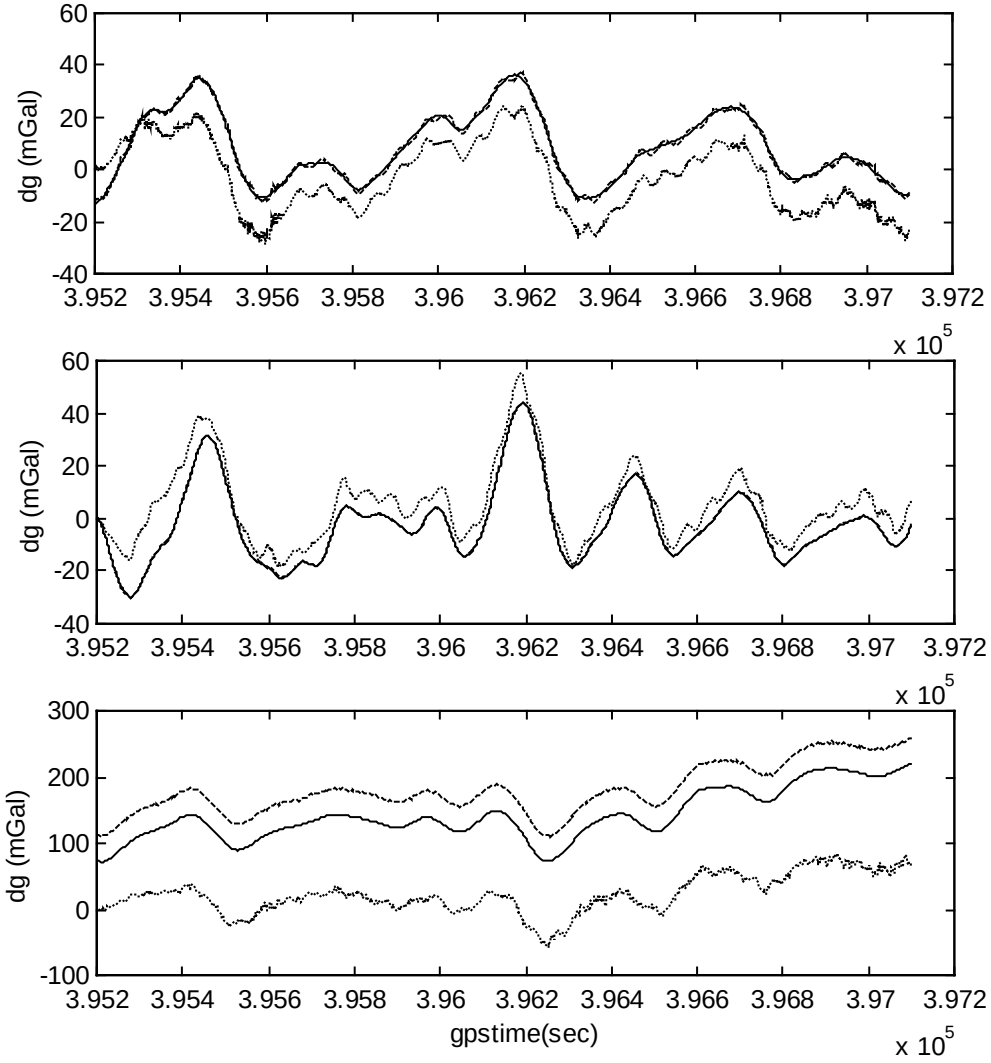

Figure 5.8 Control data (solid), observations (dashed) after adding 40 ppm of accelerometer scale factor error, and residuals (dotted) from the Kalman filter for north (top), east (middle) and down (bottom).

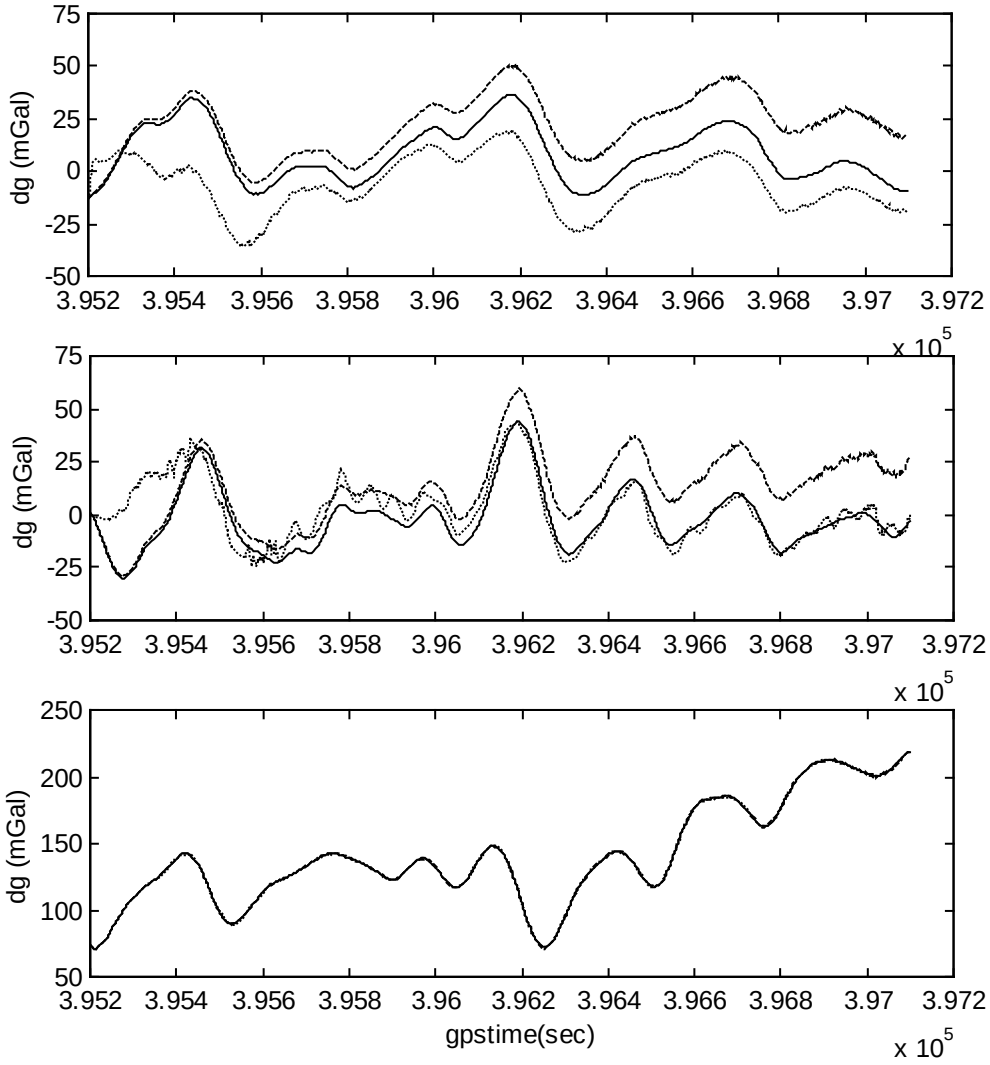

Figure 5.9 Control data (solid), observations (dashed) after adding 0.003 deg/hr of gyro bias, and residuals (dotted) from the Kalman filter for north (top), east (middle) and down (bottom).

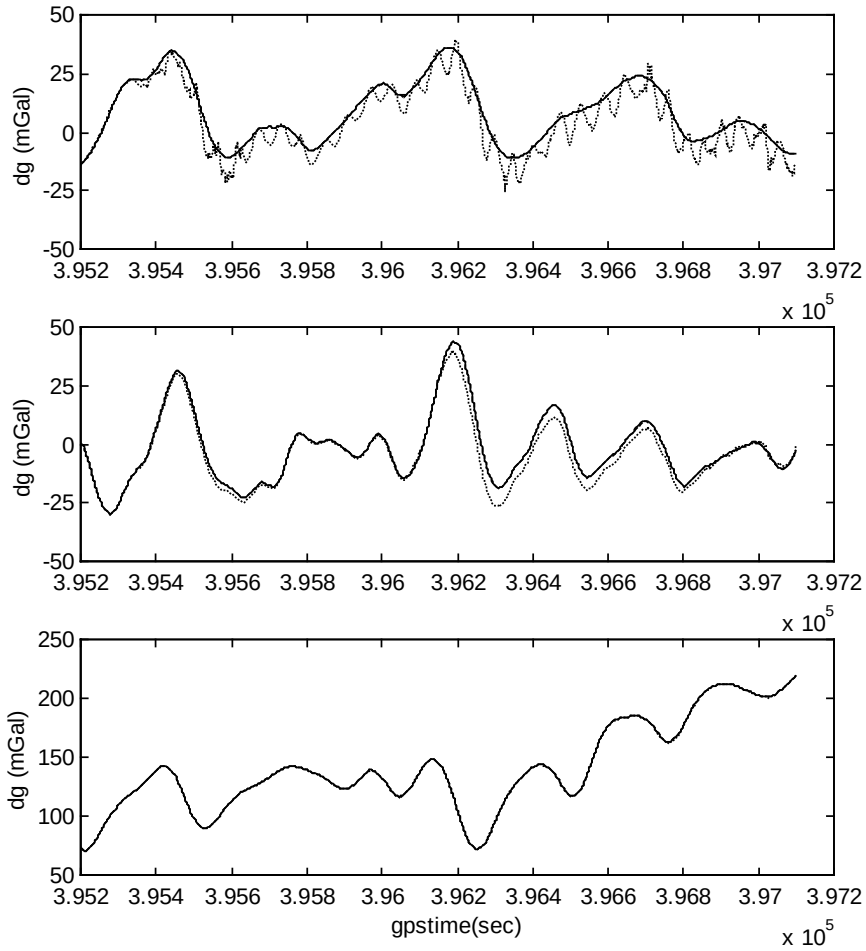

Figure 5.10 Control data (solid), observations (dashed) after adding 0.2 ppm of gyro scale factor error, and residuals (dotted) from the Kalman filter for north (top), east (middle) and down (bottom).

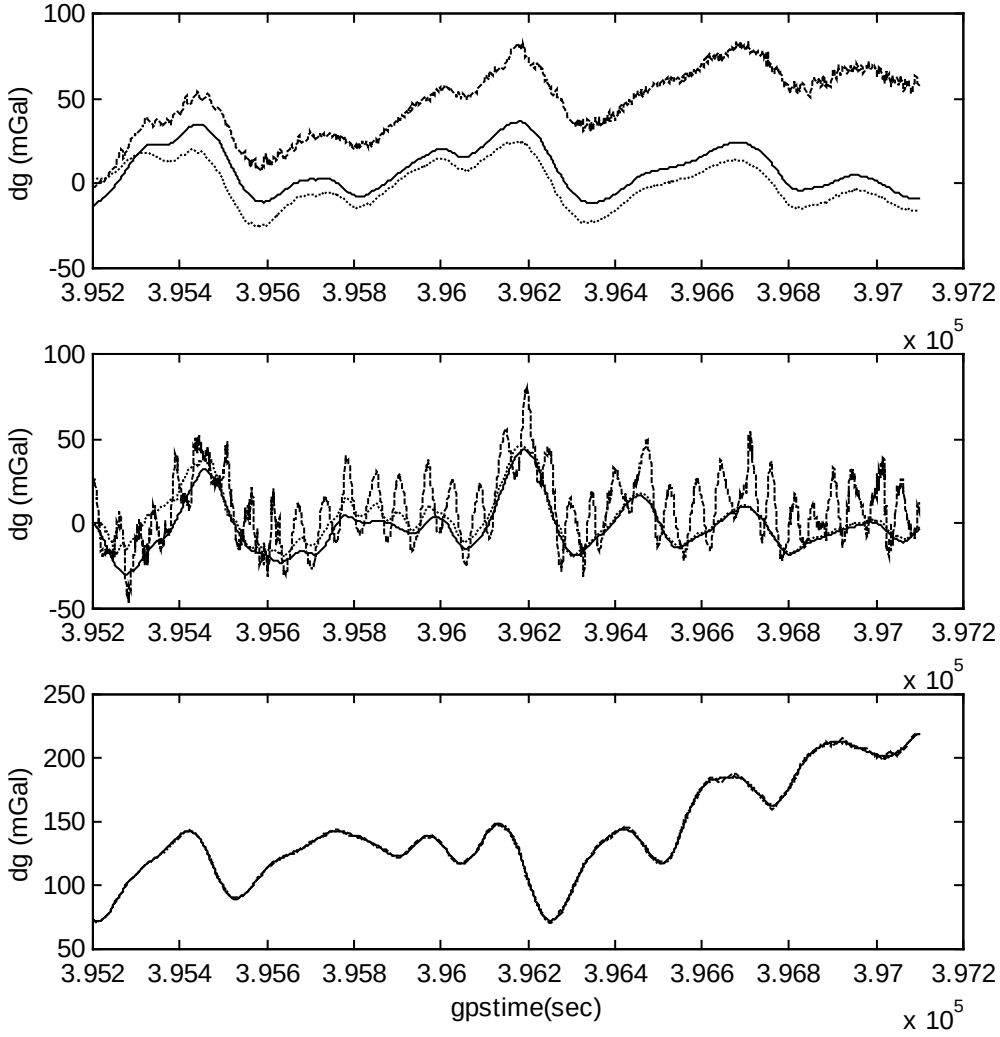

Figure 5.11 Control data (solid), observations (dashed) after adding 2 arc second of horizontal and 2 arc minute of vertical orientation error, and residuals (dotted) from the Kalman filter for north (top), east (middle) and down (bottom).

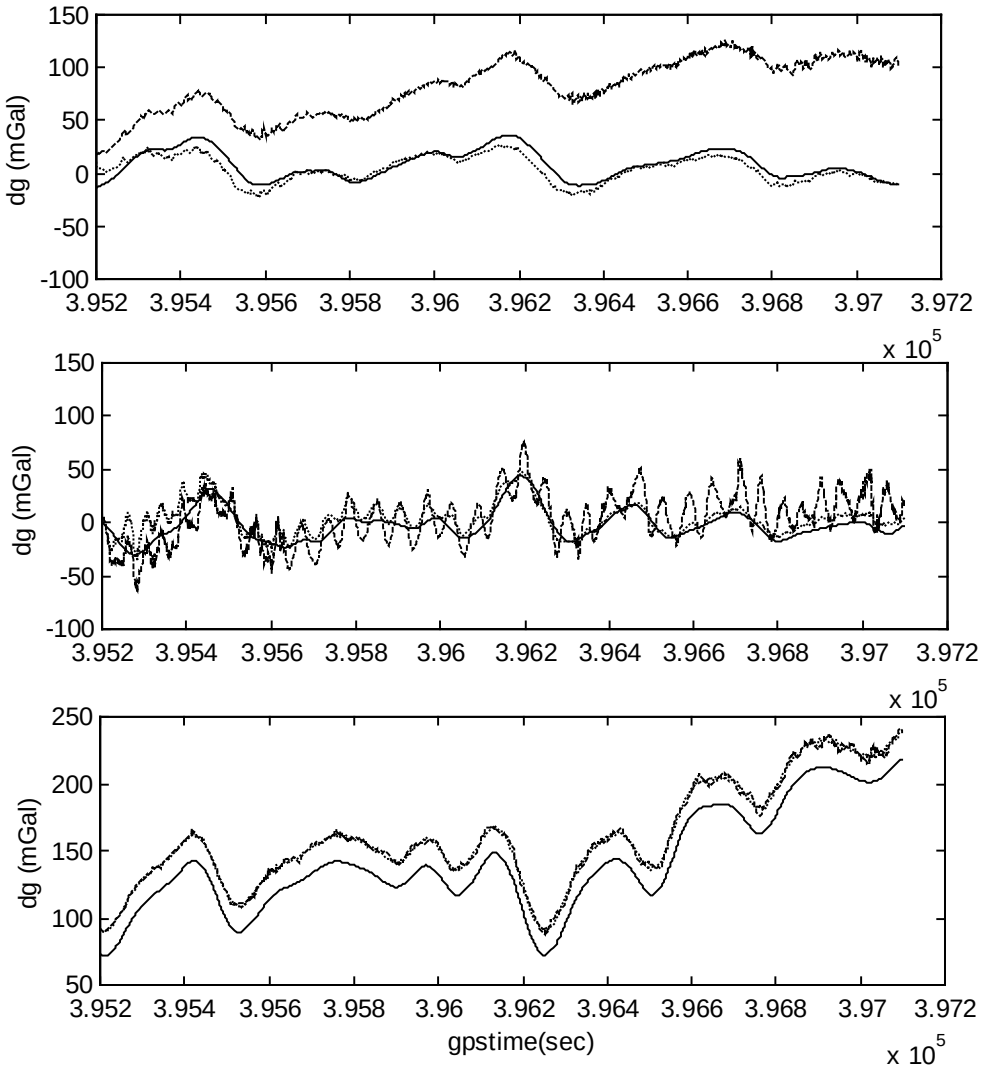

Figure 5.12 Control data (solid), observations (dashed) after adding all previous errors, and residuals (dotted) from the Kalman filter for north (top), east (middle) and down (bottom). Error parameters modeled in this case were only the orientation errors.

5.4 Results from the Real Test Flight

The investigations on the INS error characteristics through the simulations provide a basic idea on the types of INS errors to be included in the analysis of real test

flight data. The smoothed (60s) observation vector (GPS acceleration – INS acceleration – normal gravitation) for the test flight clearly shows the long term trends caused by orientation error or gyro biases and the short term error (see north component) caused by the airplane dynamics (Figure 5.13). Note that the high frequency errors caused by scale factor errors are almost eliminated by the smoothing. Also note the big anomalies at the vehicle turns.

5.4.1 Residuals from Kalman Filtering

As mentioned in the previous section on the simulation, the parameter vector in the Kalman filter should be assigned in such a way that the targeted error effects could be eliminated or reduced. Looking at the smoothed observations again (Figure 5.13), one can notice that the major error appears in the long wavelength.

A numerical comparison using computed means and standard deviations of the observations with respect to the control data, is shown in Table 5.3. The large standard deviations for the horizontal components ±(18-78 mGal) are mostly caused by the overall trends due to the orientation error (see corresponding Figure 5.13). It should be noted that the down component shows a much better standard deviation than the horizontal components. Especially, the down component of line 3 already has a very good standard deviation of ±4.5 mGal. This is because the down component is less sensitive to the orientation errors. Therefore, the orientation error and/or gyro biases should be the appropriate candidates for the system error parameters, to remove the long-term errors. In addition, one has to notice that discontinuities occur at vehicle's turns. Because of the discontinuities, the slopes of the trends as well as the biases are different before and after each turn. Therefore, it might be a good idea to include the accelerometer biases in the model parameter vector.

(mGal)

		Line 1	Line 2	Line 3
North	S.D.	63.36	77.85	35.27
	Mean	-272.94	-573.86	-827.20
East	S.D.	31.06	18.62	46.67
	Mean	-108.53	-16.79	-215.86
Down	S.D.	10.86	12.42	4.54
	Mean	35.42	96.77	131.30

Table 5.3 Estimated means and standard deviations of the observations (GPS acceleration-INS acceleration-Normal gravity) with respect to the control data.

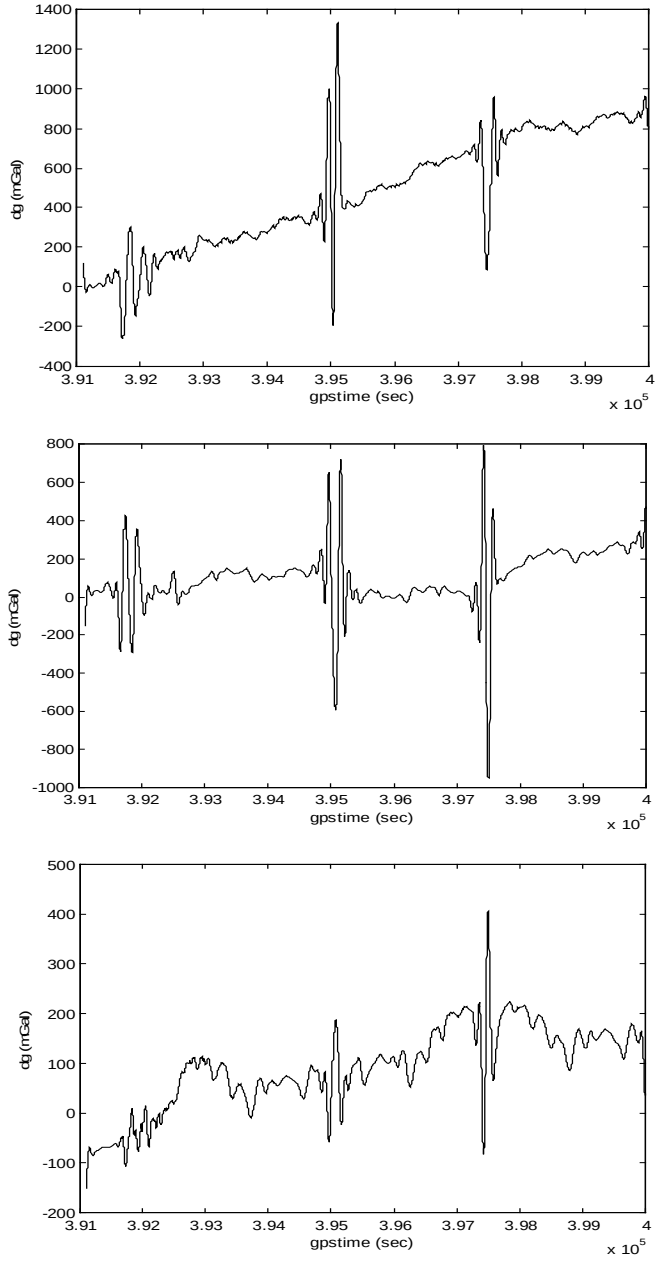

Figure 5.13 Smoothed observation vector for all lines; North (top), East (middle) and Down (bottom).

After numerous tests for different sets of error parameters, the set showing the best results from the Kalman filter are presented. The error parameters in this case are

composed of the accelerometer bias and orientation error. The initial values are set to zeros for all parameters and the variances are set as $(20\ \text{mGal})^2$ for accelerometer biases, $(2\ \text{arc-second})^2$ for horizontal orientation error and $(2\ \text{arc-minute})^2$ for vertical orientation error. The scale factor errors are excluded as already mentioned because the effects are small and would be reduced significantly through the smoothing procedures anyway.

The Figures 5.14-5.16 show the control data versus the residuals from the Kalman filter with error parameters comprising accelerometer biases and orientation errors for all three components. Compared to the smoothed observations in Figure 5.13, the overall trends in north and down component were significantly reduced through the filter. The east components, however, still show systematic errors at both ends of the profiles in all three lines.

The standard deviations of the residuals with respect to the control data show tremendous improvement in all three components; 25~65 mGal in north, 1~16 mGal in east, and 0.5~6 mGal in down component (Table 5.4). The standard deviations for the east component are not as good as for the north component because of the remaining systematic error. Especially, the poor result on the east component of line 3 is caused by the down tendency after the big anomaly around 243^o longitude. Comparing the east components of lines 1 and 3, with line 2, one can see that the remaining systematic errors have dependency on the direction of flight. Therefore, the reason for the poor standard deviations might be the coupling effect of the uncompensated north orientation error with the down acceleration.

Note that the local peaks and valleys in the east component, however, are very well detected so that the results could be refined by further processing such as endmatching and WCF.

(mGal)

		Line 1	Line 2	Line 3
North	S.D.	±11.6580	±13.3326	±14.0436
	Mean	-16.5649	-5.6712	-5.1604
East	S.D.	±17.1909	±17.0348	±20.6910
	Mean	-14.0085	18.4831	-19.9004
Down	S.D.	±5.0227	±6.5081	±3.9132
	Mean	24.9730	52.4192	49.0363

Table 5.4 Estimated means and standard deviations of the difference between the residuals from Kalman filter and the control data (accelerometer bias and orientation error parameters).

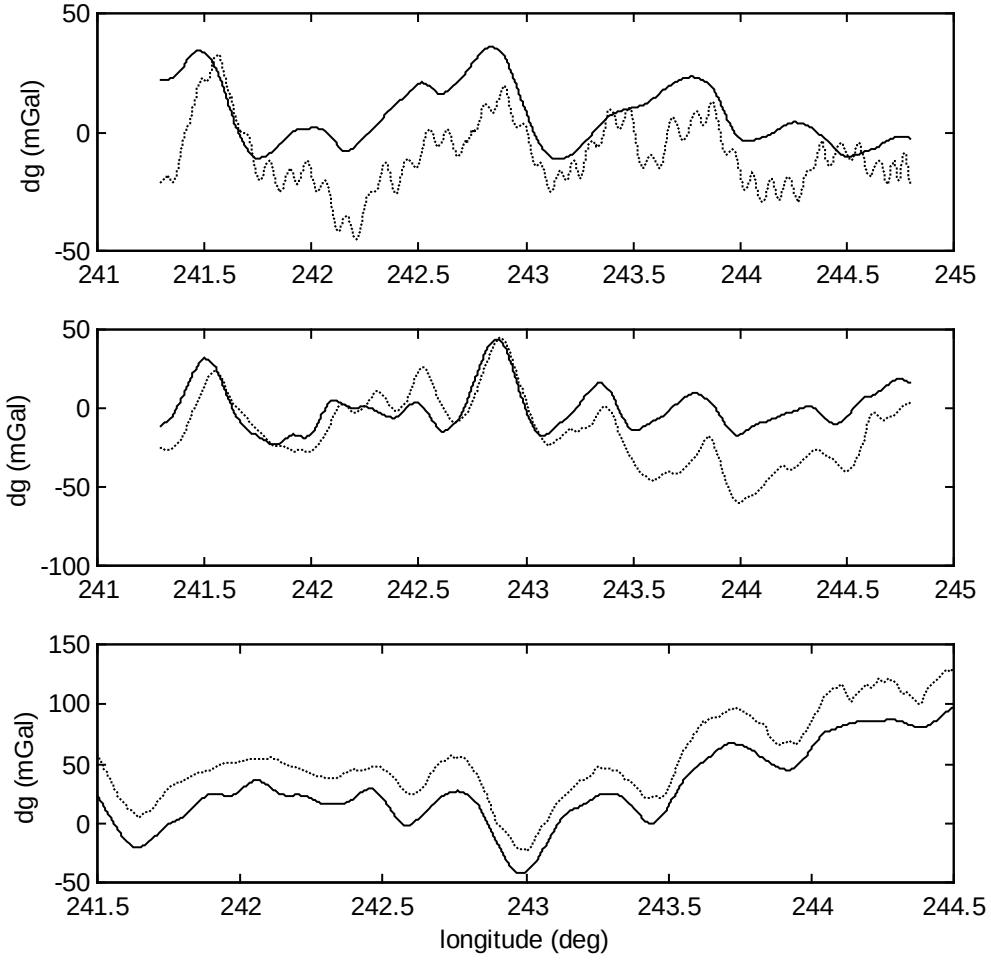

Figure 5.14 Residuals (dotted) from Kalman filter and the control data (solid) for Line 1 (accelerometer bias and orientation error states).

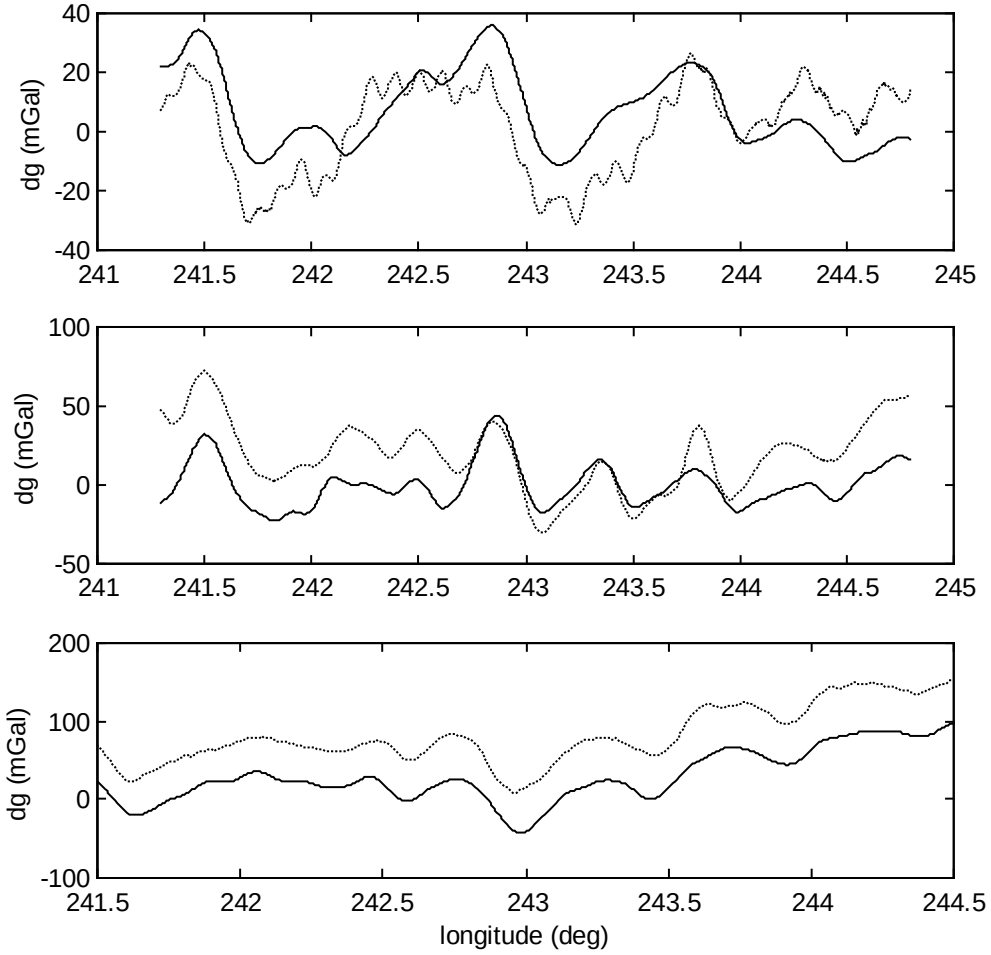

Figure 5.15 Residuals (dotted) from Kalman filter and the control data (solid) for Line 2 (accelerometer bias and orientation error states).

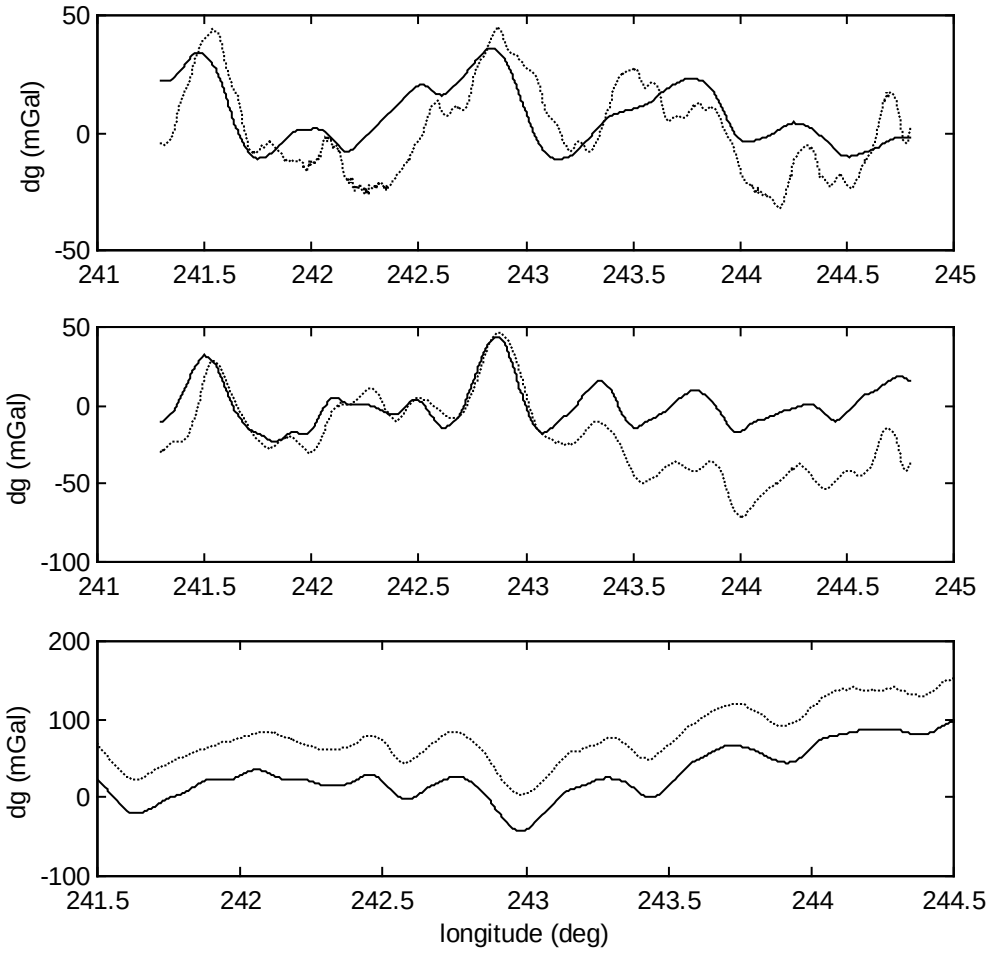

Figure 5.16 Residuals (dotted) from Kalman filter and the control data (solid) for Line 3 (accelerometer bias and orientation error states).

5.4.2 Applying Endmatching

To eliminate the biases and remaining system errors, additional external information on the gravity field is assumed. For example, the gravity values at both ends of the profile are assumed to be available. Thus, by applying a linear correction through endmatching, one can obtain refined residuals having better global trends (Figure 5.17-19).

After applying endmatching, the standard deviations for the east component of lines 2 and 3 as well as the estimated mean differences for the down component are significantly improved (Table 5.5). In some cases, however, the endmatching produced worse results (see north component of line 1 and 3). This shows that the global trends for north are already compensated and a simple linear correction is not enough to eliminate the other effects such as high frequency errors due to the airplane dynamics.

(mGal)

		Line 1	Line 2	Line 3
North	S.D.	±12.1733	±11.1466	±16.8663
	Mean	14.7704	-6.3520	5.9142
East	S.D.	±17.6997	±16.5883	±14.8558
	Mean	-0.9360	-30.5066	15.2725
Down	S.D.	±5.1620	±4.9868	±3.4742
	Mean	-8.2847	2.2427	-1.8933

Table 5.5 Estimated means and standard deviations of the difference between the residual after endmatching and the control data (accelerometer bias and orientation error).

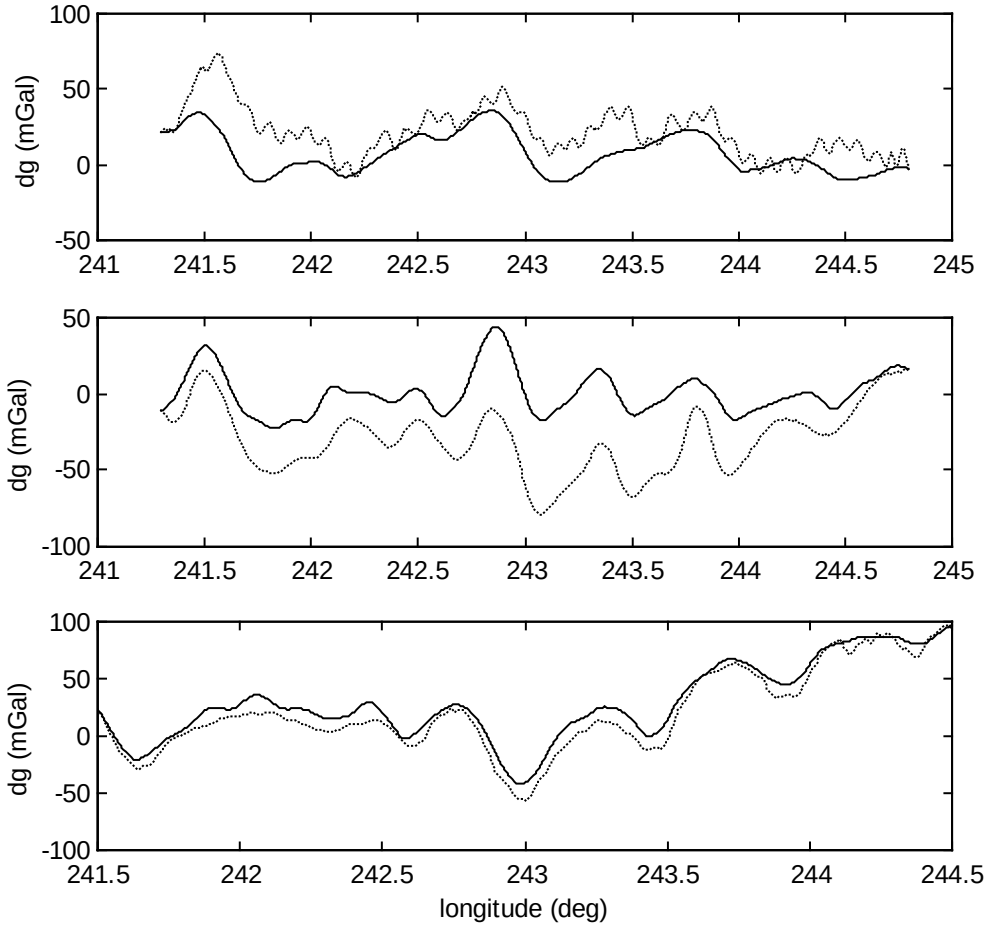

Figure 5.17 Residuals (dotted) after endmatching and control data (solid) for Line 1 (accelerometer bias and orientation error states).

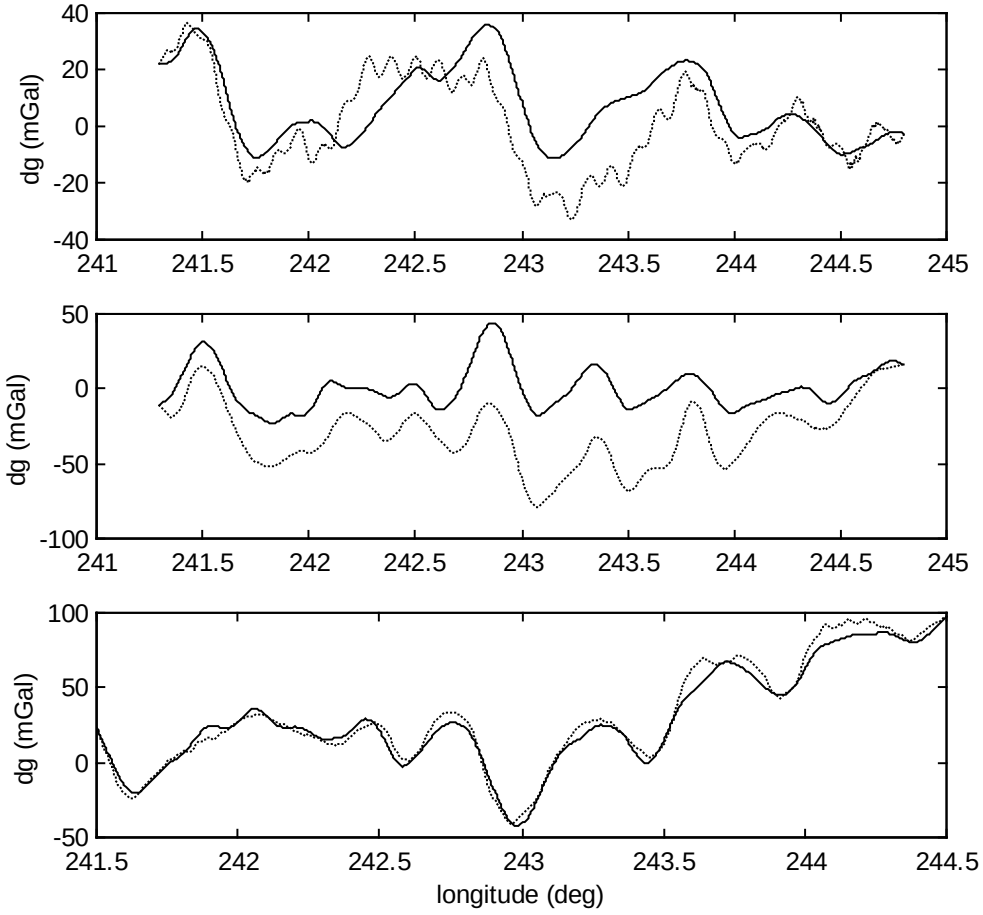

Figure 5.18 Residuals (dotted) after endmatching and control data (solid) for Line 2 (accelerometer bias and orientation error states).

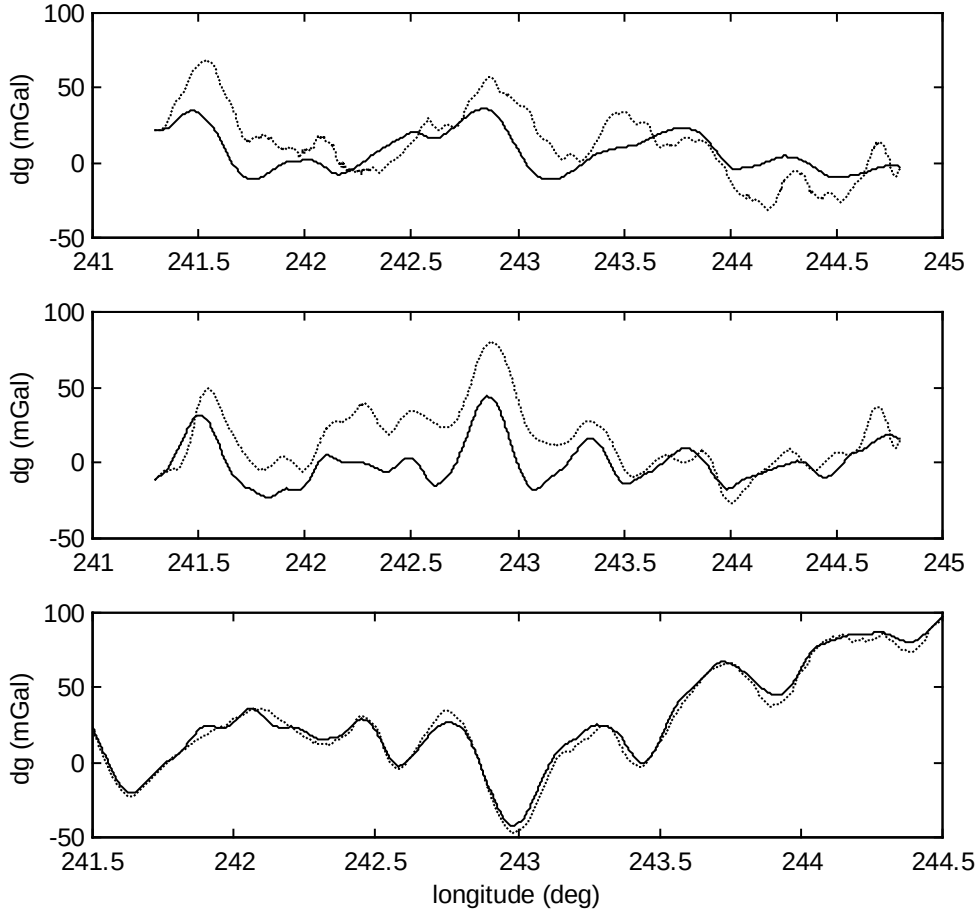

Figure 5.19 Residuals (dotted) after endmatching and control data (solid) for Line 3 (accelerometer bias and orientation error states).

5.4.3 Final Results after WCF

It has been shown that WCF is an efficient method to extract a signal from the

observations measured from overlapping or parallel tracks in the traditional case. Since it operates in the frequency domain, the components having more than a certain amount of correlation will be preserved in corresponding frequency bands (Figure 5.20-22). Therefore, as a final procedure in refining the residuals from the Kalman filter, WCF was applied to all combinations of two parallel tracks (Line1-2, Line1-3 and Line2-3). The results from WCF show significant improvements in combinations Line1-2 and Line2-3.

After applying WCF, one can find a very interesting feature from the results, namely, the dependency of the INS errors on the direction of the flight. That is, WCF generates much better results for the combinations line1-2 and line 2-3, while the line1-3 combination does not show any improvements (Table 5.6).

The residuals for line 1 and line 3 are almost on top of each other, so the characteristics of the long-term INS error are almost the same while for line 2 they have opposite characteristics. Therefore, uncompensated long term errors after the Kalman filtering in opposite travel paths are canceled out through the WCF as in the case of line1-2 and line2-3 combinations. WCF applied to the combination line1-3, however, does not reduce the errors because they have common characteristics and are considered as signals in the WCF.

(mGal)

		Line 12	Line 13	Line 23
North	S.D.	±6.84	±13.12	±7.80
	Mean	4.21	10.34	-0.22
East	S.D.	±6.75	±15.82	±6.70
	Mean	-15.72	-0.31	-0.31
Down	S.D.	±4.38	±3.43	±3.16
	Mean	-3.02	-5.09	0.17

Table 5.6 Estimated mean and standard deviation of the difference between the residuals after endmatching, WCF and the control data (accelerometer bias and orientation error parameters).

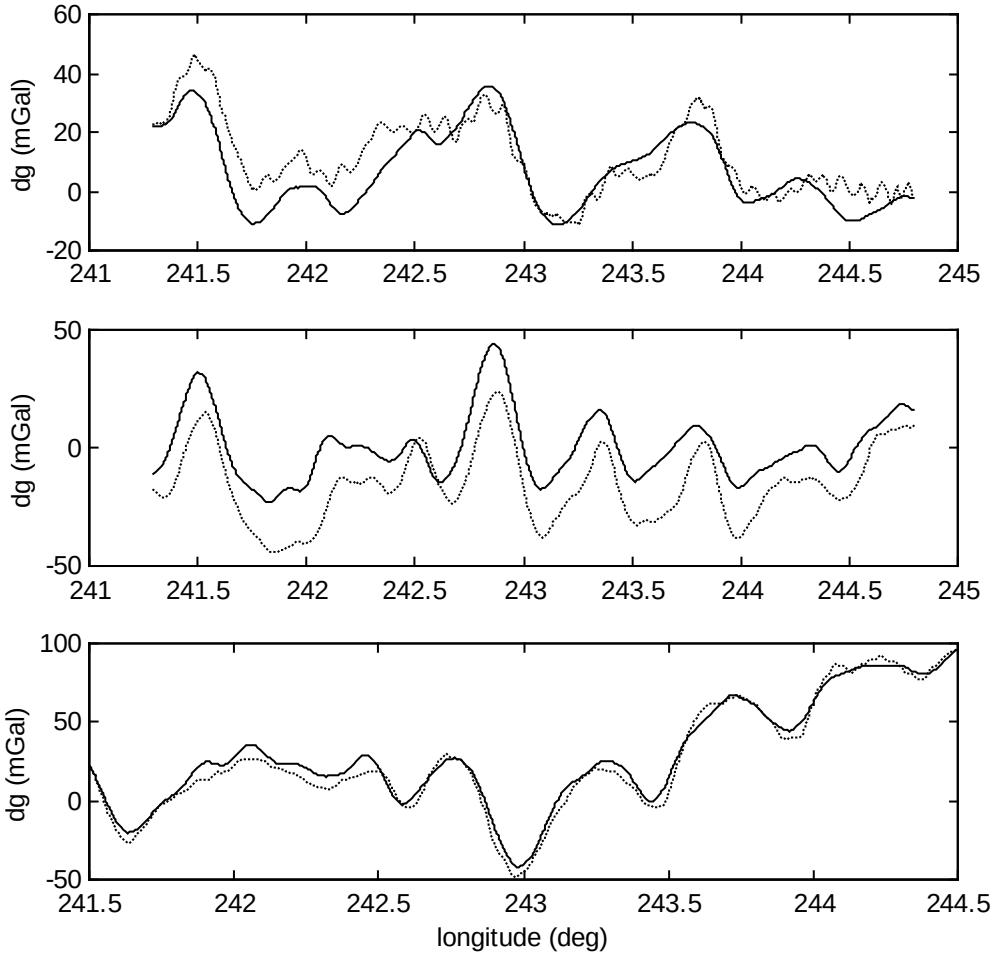

Figure 5.20 Residuals (dotted) after endmatching and WCF vs. control data (solid) for Line 1-2 combination (acceleration bias and orientation error parameter model).

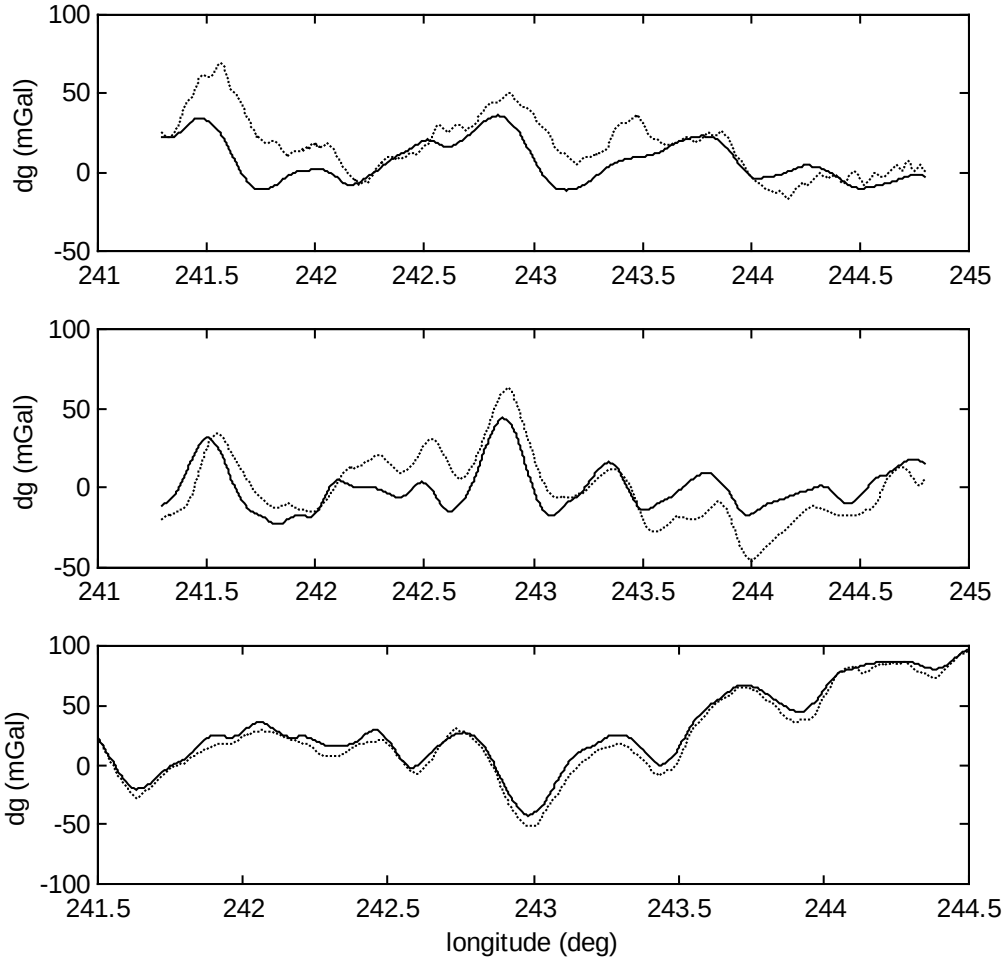

Figure 5.21 Residuals (dotted) after endmatching and WCF vs. control data (solid) for Line 1-3 combination (acceleration bias and orientation error parameter model).

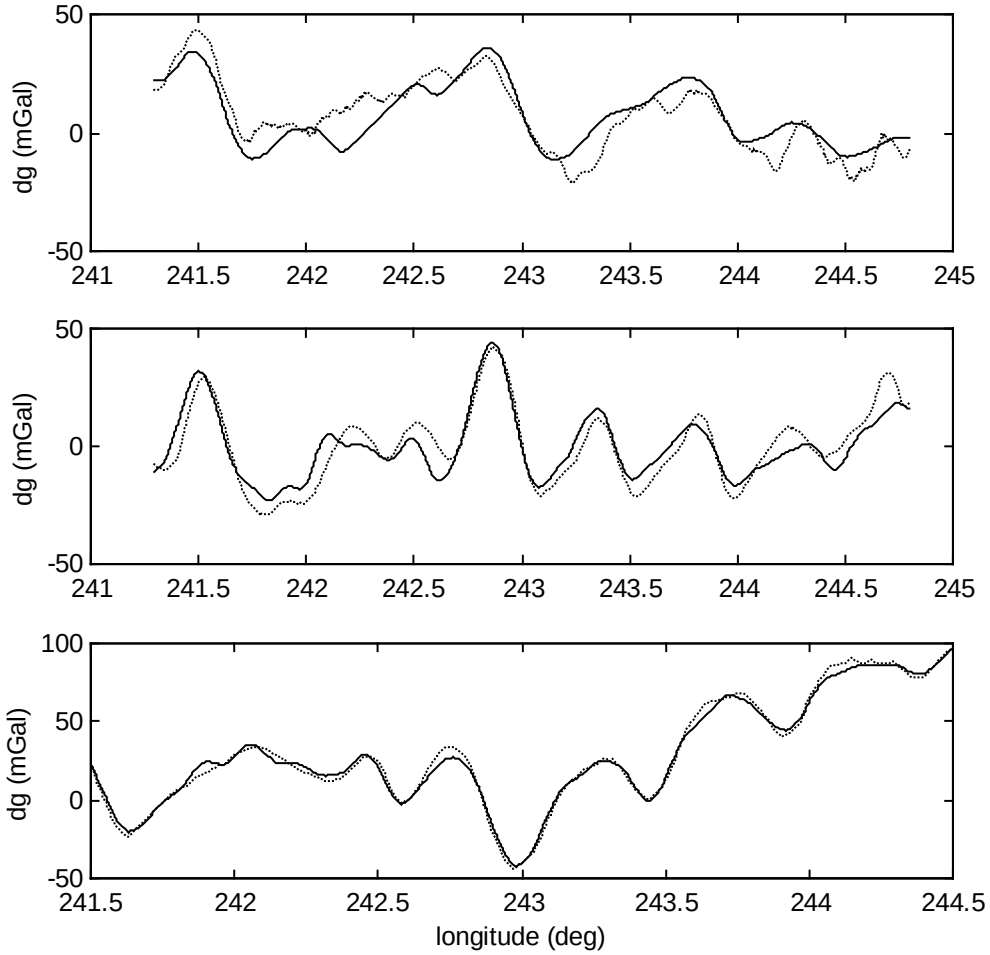

Figure 5.22 Residuals (dotted) after endmatching and WCF vs. control data (solid) for Line 2-3 combination (acceleration bias and orientation error parameter model).

As mentioned before, the estimates for the down component are better than for the horizontal components because the down component is insensitive to the orientation error. The best accuracy of ±3.16 mGal for the down component is

obtained from line 3. The other two lines also show that the down component can be recovered with an accuracy of 3-4 mGal. Although the accuracy is not as good as for the vertical component, the horizontal components also are well estimated with an accuracy of ±(6-8 mGal). Therefore, it can be concluded that the deflection of the vertical can be recovered with an accuracy better than ±2 arc seconds (1 arc second ≈ 4.75 mGal). The resolution corresponding to 60-second smoothing is about 3.5 km, but the resolution of the final results is about 10 km due to the attenuation with altitude.

CHAPTER 6

DISCUSSIONS ON THE NEW ACCELERATION ALGORITHM

6.1 Introduction

Although the results from the new algorithm were comparatively good compared to the control data sets, one might consider using a statistical or empirical model for the gravity disturbances to improve the estimation. As already mentioned several times, the mathematical model in the new approach includes the gravity disturbance invisibly in the total random observation error. Therefore, a modification of the mathematical model would be advisable for theoretical reasons. Toward this aim, two methods are investigated, namely, the iteration method and the inclusion of a parametric gravity model.

6.2 Iteration for better estimates of the INS system errors

Since the gravity disturbance is not included in the Kalman filter states, the estimates of the INS system errors are considered to be somewhat inaccurate. That is, these estimates will include some effect from the gravity signal. Thus, once the residual vector is obtained from the Kalman filter, it can be subtracted from the observation vector so that the filter may generate better estimates for the INS system errors in a modified model.

Starting from the fundamental equation (5.30),

$$\tilde{\ddot{\mathbf{x}}}^i - \delta\ddot{\mathbf{x}}^i = \tilde{\mathbf{a}}^i - \delta\mathbf{a}^i + \mathbf{g}^i, \tag{6.1}$$

one can set up the observation vector, denoted with tilde, as follows:

$$\tilde{\mathbf{y}}^i = \tilde{\ddot{\mathbf{x}}}^i - \mathbf{g}^i, \tag{6.2}$$

where $\tilde{\mathbf{y}}^i$ is the formal definition for the observations, $\tilde{\ddot{\mathbf{x}}}^i$ contains the GPS kinematic accelerations, and $\mathbf{g}^i$ is the true gravitation vector. Note that we measure the specific force $\tilde{\mathbf{a}}^i$. Then, the observation equation for the parameters will be:

$$\delta\mathbf{y} = \tilde{\mathbf{a}}^i - \tilde{\mathbf{y}}^i = \tilde{\mathbf{a}}^i - \tilde{\ddot{\mathbf{x}}}^i + \mathbf{g}^i = \delta\mathbf{a}^i - \delta\ddot{\mathbf{x}}^i. \tag{6.3}$$

Note that the true gravity in the above equation is not available. Thus, using normal gravity as an approximation;

$$\begin{aligned}\delta\mathbf{y}_0 &= \tilde{\mathbf{a}}^i - \tilde{\mathbf{y}}^i{}_0 = \tilde{\mathbf{a}}^i - \tilde{\ddot{\mathbf{x}}}^i + \gamma^i = \delta\mathbf{a}^i - \delta\ddot{\mathbf{x}}^i - \delta\mathbf{g}^i \\ &= \delta\mathbf{a}_s^i + \varepsilon_a^i - \delta\ddot{\mathbf{x}}^i - \delta\mathbf{g}^i\end{aligned} \quad . \tag{6.4}$$

Note that the observation error of the INS is divided into the system parameters (random effects) and random noise ($\delta\mathbf{a}^i = \delta\mathbf{a}_s^i + \varepsilon_a^i$). The gravity disturbance is intentionally included in the total observation error budget since we assume that no information on the gravity disturbances is available. Assuming random noise for the GPS observation error, the total observation error budget in (6.4) is:

$$\varepsilon^i = \varepsilon_a^i - \delta\ddot{\mathbf{x}}^i - \delta\mathbf{g}^i \tag{6.5}$$

If the gravity disturbance has statistically distinguishable characteristics with respect to the INS systematic error parameters, the residuals after Kalman filtering using equation (6.4) will in a certain way reflect the gravity signal. In addition, if the gravity signal is much stronger than the adjusted system noise, one can define:

$$\delta\mathbf{y}_0 - \delta\hat{\mathbf{a}}_s^i = \tilde{\varepsilon}^i =: -\delta\hat{\mathbf{g}} \tag{6.6}$$

The critical factor in the above equation is that the gravity signal should dominate the total observation error and its estimates can hence be equated with the residuals after the Kalman filtering.

Now, one can update the approximated gravitation by adding the first approximation of the gravity disturbance from (6.6).

$$\gamma^i + \delta\hat{\mathbf{g}} := \hat{\mathbf{g}}_1^i \tag{6.7}$$

Because the gravity model error should be significantly reduced through the updated gravitation ($\hat{\mathbf{g}}_1^i$), it is expected that the estimation of the INS system parameters can be improved in a new filtering. By investigating the residuals from the iterative procedure, one can stop iterations, and take out the estimates of the error parameters from the original observation vector, thus generating the estimates for the gravity disturbance vector.

The results from this iteration method, however, showed no improvements at all. The main reason is that the model was updated with wrong estimates of gravity disturbances at each iteration. The residuals from the initial Kalman filter include the effect of not only the gravity disturbances but also some uncompensated system errors. Thus, updates with wrong values did not improve the estimates of the INS system errors, nor the estimated gravity disturbances.

6.3 Model Refinement with a Gravity Model

Obviously, the disadvantage of the new approach is that one cannot get realistic standard deviations for the estimated gravity disturbances because of the way they were estimated. This leads to the lack of satisfaction in the theoretical treatment of the model, and a rigorous solution to that would certainly include a gravity model as part of the observation equation.

The mathematical model is completed with the gravity term as follows (compare with eq. 5.37):

$$\mathbf{x}^i - \mathbf{a}^i - \gamma_n^i = -C_b^i \mathbf{b}_a - C_b^i [\mathbf{a}^b]\mathbf{k}_a - \mathbf{a}^i \times \psi^i + \delta\mathbf{g}^i - C_b^i \varepsilon_a + \delta\mathbf{x}^i . \quad (6.8)$$

Now, a gravity model is introduced to isolate $\delta\mathbf{g}^i$ in the above equation. Since the gravity modeling is not the main issue in this study, the well known third-order Gauss-Markov process and an empirical trigonometric expansion were designed and tested in this study.

6.3.1 Third Order Gauss-Markov Process

A third order Gauss-Markov process (see equation 4.42 ~ 4.44) has been selected for the gravity disturbances and included in the observation model. The number of the parameters increases to 24 by adding 9 parameters for the gravity disturbances and the design matrix H as well as the dynamic matrix F are properly expanded.

$$\underset{3\times 24}{H} := \begin{bmatrix} -C_b^i & 0 & -[\tilde{\mathbf{a}}^i]C_b^i & 0 & [\tilde{\mathbf{a}}\times] & I & 0 & 0 \end{bmatrix}, \quad (6.9)$$

$$\underset{24\times 1}{\mathbf{x}} := \begin{bmatrix} \mathbf{b}_a^T & \mathbf{b}_g^T & \mathbf{k}_a^T & \mathbf{k}_g^T & \psi^T & \delta\mathbf{g}^T & (\delta\mathbf{g}')^T & (\delta\mathbf{g}'')^T \end{bmatrix}^T, \quad (6.10)$$

$$F = \begin{bmatrix} F_{11} & 0 \\ 0 & F_{22} \end{bmatrix}; \qquad F_{11} = \begin{bmatrix} 0 & 0 & 0 & 0 & 0 \\ 0 & 0 & 0 & 0 & 0 \\ 0 & 0 & 0 & 0 & 0 \\ 0 & 0 & 0 & 0 & 0 \\ 0 & -C_b^i & 0 & -C_b^i[\omega_{ib}^b] & 0 \end{bmatrix},$$

$$F_{22} = \begin{bmatrix} 0 & 0 & 0 & 1 & 0 & 0 & 0 & 0 & 0 \\ 0 & 0 & 0 & 0 & 1 & 0 & 0 & 0 & 0 \\ 0 & 0 & 0 & 0 & 0 & 1 & 0 & 0 & 0 \\ 0 & 0 & 0 & 0 & 0 & 0 & 1 & 0 & 0 \\ 0 & 0 & 0 & 0 & 0 & 0 & 0 & 1 & 0 \\ 0 & 0 & 0 & 0 & 0 & 0 & 0 & 0 & 1 \\ -\beta_1^3 & 0 & 0 & -3\beta_1^2 & 0 & 0 & -3\beta_1 & 0 & 0 \\ 0 & -\beta_2^3 & 0 & 0 & -3\beta_2^2 & 0 & 0 & -3\beta_2 & 0 \\ 0 & 0 & -\beta_3^3 & 0 & 0 & -3\beta_3^2 & 0 & 0 & -3\beta_3 \end{bmatrix}. \quad (6.11)$$

The detailed formulations and the equations for the gravity part are the same as described in section 4.4.

As in the traditional case, various values for the gravity model parameters such as correlation distance (10~150 km) and variances (400~1500 mGal^2) were tested. Among them, the best results were achieved with correlation distance about 12 km and variance of 900 mGal^2 and are presented in Figure 6.1 for all three legs. The gravity estimates in this case were more sensitive to the correlation distance than the variances.

As one can see, the estimates are poorer than the residuals with no gravity model in all three components. Overall standard deviations of horizontal components as well as vertical components are up to several times larger than in the case of no gravity model (Table 6.1 vs. Table 5.4). Especially, the east component of leg 1 shows the worst result caused by the instability of the filter at the beginning of the flight.

(mGal)

	Leg 1	Leg 2	Leg 3
North	20.29	13.00	16.64
East	63.62	20.78	33.44
Down	12.53	13.891	6.99

Table 6.1 Standard deviations of the difference between the estimates of the gravity disturbance and the control data.

The standard deviation is as high as ±63 mGal. The best result was obtained for the down component of leg 3 with a standard deviation of ±7 mGal.

Obviously, the proper interpretation of the poorer results would be that the selected Gauss-Markov process does not represent the gravity field well enough in this area so that some part of it is still hidden in the residuals. One can expect refined results by applying the further application of endmatching and WCF. Especially, the east component will be much better by those additional procedures because it seems to have serious systematic errors.

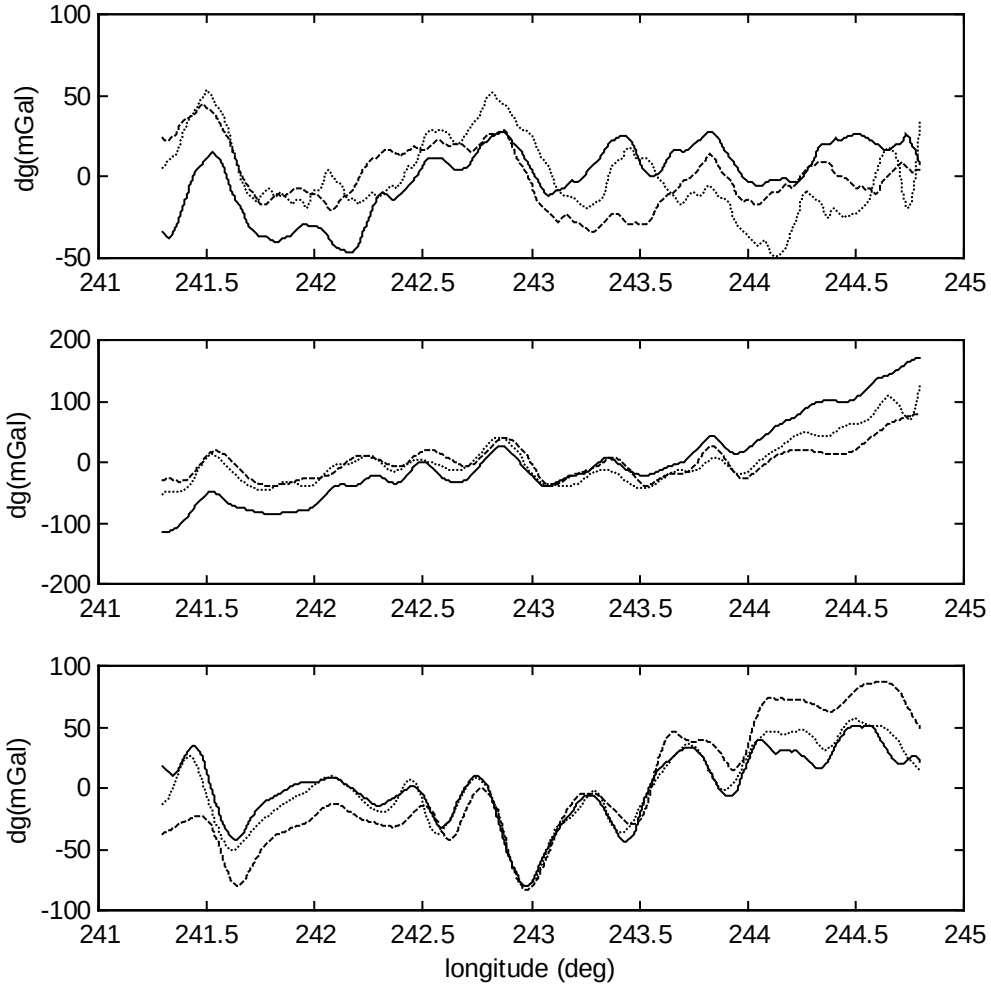

Figure 6.1 Estimated Gravity Disturbances using a third order Gauss-Markov Model for leg 1 (solid), 2 (dashed) and 3 (dotted); North (top), East (middle), Down(bottom).

6.3.2 Empirical Trigonometric Representation for Gravity

In this section, the gravity disturbance is modeled as a sum of trigonometric functions. It should be noted that this approach is purely empirical. Since the residual from the original model seems to reflect the gravity more or less, a frequency analysis was performed to analyze the residual. After identifying the main frequency band or highest frequency contained in the residual, a corresponding combination of trigonometric functions with unknown amplitude is used to model each gravity disturbance component δg_j. In other words, the gravity disturbance is modeled as:

$$\begin{aligned}\delta g_j &= \sum_{k=0}^{n} a_{jk}\cos\frac{2\pi kt}{T}+\sum_{k=0}^{n} b_{jk}\sin\frac{2\pi kt}{T}\\ &= a_{j0}+a_{j1}\cos\frac{2\pi t}{T}+a_{j2}\cos\frac{2\pi\cdot 2t}{T}+\ldots+a_{jn}\cos\frac{2\pi\cdot nt}{T}\\ &\quad +b_{j1}\sin\frac{2\pi t}{T}+b_{j2}\sin\frac{2\pi\cdot 2t}{T}+\ldots+b_{jn}\sin\frac{2\pi\cdot nt}{T}\\ &= D_j\cdot\beta_j\end{aligned} \tag{6.12}$$

The matrix D_j consists of trigonometric functions dependent on time, t. The vector β_j consists of the coefficients of the trigonometric functions. With all three components combined, we have

$\delta\mathbf{g} = D\cdot\beta$,

where

$$\underset{3\times 3(2n+1)}{D}=\begin{bmatrix} D_1 & 0 & 0\\ 0 & D_2 & 0\\ 0 & 0 & D_3\end{bmatrix},$$

$$\underset{1\times(2n+1)}{D_1}=D_2=D_3=\begin{bmatrix}1 & \cos\frac{2\pi t}{T} & \cos\frac{2\pi t\cdot 2}{T} & \ldots & \sin\frac{2\pi t}{T} & \sin\frac{2\pi t\cdot 2}{T} & \ldots & \sin\frac{2\pi t\cdot n}{T}\end{bmatrix}$$

$$\underset{3(2n+1)\times 1}{\beta}=\begin{bmatrix}\beta_1\\ \beta_2\\ \beta_3\end{bmatrix};\beta_1=\begin{bmatrix}a_{10}\\ a_{11}\\ a_{12}\\ \vdots\\ a_{1n}\\ b_{11}\\ \vdots\\ b_{1n}\end{bmatrix},\beta_2=\begin{bmatrix}a_{20}\\ a_{21}\\ a_{22}\\ \vdots\\ a_{2n}\\ b_{21}\\ \vdots\\ b_{2n}\end{bmatrix},\beta_3=\begin{bmatrix}a_{30}\\ a_{31}\\ a_{32}\\ \vdots\\ a_{3n}\\ b_{31}\\ \vdots\\ b_{3n}\end{bmatrix} \tag{6.13}$$

It should be mentioned that the gravity is modeled as a function of time assuming a constant velocity of the vehicle for the purpose of simplicity.

Substituting equation (6.12) into equation (6.8) yields:

$$\ddot{\mathbf{x}}^i-\mathbf{a}^i-\gamma_n^i=-C_b^i\mathbf{b}_a-C_b^i[\mathbf{a}^b]\mathbf{k}_a-\mathbf{a}^i\times\psi^i+D\cdot\beta-C_b^i\varepsilon_a+\delta\ddot{\mathbf{x}}^i. \tag{6.14}$$

With maximum order of expansion n, the number of the unknown parameters are increase up to 3×(2n+1), so the size of the design matrix H, the state vector x and the dynamic matrix F should be properly expanded. The extended parameters, β, are modeled as random effects with initial variance of $(1\ \text{m/sec})^2$.

$$\underset{3\times(15+6n+3)}{H} = \left[-C_b^i \quad 0 \quad -[\tilde{\mathbf{a}}^i]C_b^i \quad 0 \quad [\tilde{\mathbf{a}}\times] \quad D\right], \tag{6.15}$$

$$\underset{(15+6n+3)\times 1}{\mathbf{x}} := \left[\mathbf{b}_a^T \quad \mathbf{b}_g^T \quad \mathbf{k}_a^T \quad \mathbf{k}_g^T \quad \psi^T \quad \beta_1^T \quad \beta_2^T \quad \beta_3^T\right]^T, \tag{6.16}$$

$$\underset{(15+6n+3)\times(15+6n+3)}{F} = \begin{bmatrix} F_{11} & 0 \\ 0 & \underset{(6n+3)\times(6n+3)}{0} \end{bmatrix}; \quad F_{11} = \begin{bmatrix} 0 & 0 & 0 & 0 & 0 \\ 0 & 0 & 0 & 0 & 0 \\ 0 & 0 & 0 & 0 & 0 \\ 0 & 0 & 0 & 0 & 0 \\ 0 & -C_b^i & 0 & -C_b^i[\omega_{ib}^b] & 0 \end{bmatrix} \tag{6.17}$$

Clearly, one has to decide the maximum order n of the trigonometric expansion. Higher order would generate a more detailed signature of the gravity, but would require much more calculation time. To verify the maximum order for the expansion, a simple least-square fit on the residuals could be performed. In this study, it was shown that n should be at least 20 to obtain ±2 mGal accuracy of fit to the residuals. The actual estimation was done with $n = 10$ because of the limitations in computational time.

Figure 6.2 shows the estimates of gravity disturbances for all three legs. The estimates appear much smoother than the residuals with no gravity modeling. Furthermore, high frequency undulations appearing in the residuals for the north component have disappeared in this case because of the low frequency modeling. As the maximum order n increases, the estimates of the gravity disturbance would include some higher frequency components.

The main differences of the above result compared to the case of the un-modeled gravity disturbances include a reduction in the high frequency oscillations and a greater distortion in the low frequencies, especially in the east and down components (compare with Figures 5.14~16). This low frequency distortion led to poorer standard deviations with respect to the control data (Table 6.2). The results, however, show much better consistencies among lines and better stabilization than in the case of the Gauss-Markov process.

The maximum standard deviation appears in the east component of the leg 3 (±29.9 mGal) and the minimum is in the down component of the same profile (±9 mGal). It is interesting that the maximum and minimum differences appear in the same components (east and down in leg 3) for all three cases: no gravity model, Gauss-Markov model, and trigonometric series model.

It is expected that better estimates could be obtained with higher order expansions as well as careful selection of the frequency band in this approach. Since the purpose of this test is not to design a gravity model but to show a modification of

the mathematical model for better theoretical justification, further refinement for improved results was not carried out.

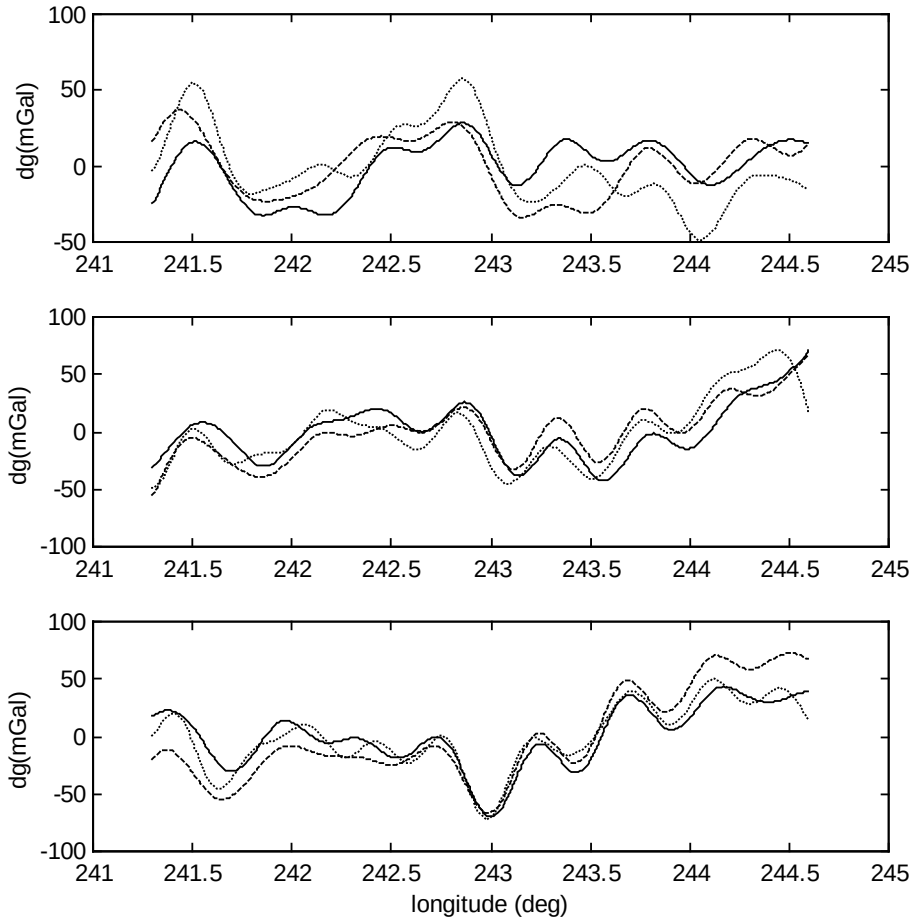

Figure 6.2 Estimated Gravity Disturbances using a trigonometric expansion of order 10 model for leg 1 (solid), 2 (dashed) and 3 (dotted); North (top), East (middle), Down(bottom).

(mGal)

	Leg 1	Leg 2	Leg 3
North	14.0	14.6	17.8
East	22.5	22.5	29.9
Down	12.4	10.3	9.0

Table 6.2 Standard deviations of the difference between the estimates of the gravity disturbance and the control data.

The advantage of this approach compared to the Gauss-Markov process case is the reduced dependency on a-priori information. One does not need any covariance model but only a simple analysis of the residuals may be sufficient. The disadvantage is the tremendous cost of calculation. Using IBM 400MHz PC, it took 35 hrs to process one leg with the expansion of order 10.

CHAPTER 7

CONCLUSIONS AND RECOMMENDATIONS

This research addressed a new efficient algorithm for recovery of the vector gravity field with airborne gravimetry using GPS and INS. The new algorithm has three distinct features compared to the traditional algorithm. First, accelerations from GPS are used as updates in a Kalman filter while positions are used in the traditional approach. Second, the gravity disturbance vector is not explicitly modeled as a stochastic process in the new approach. In other words, the gravity disturbance is intentionally included in the total observation error budget so that the corresponding effects in acceleration appear in the residuals from the Kalman filter. Third, the frame selected for all calculations is the inertial frame, while the navigation frame is selected in the traditional approach.

From the new approach with these differences, the following is achieved:

1. The concept of the algorithm is much easier because the new approach is based on the fundamental equations expressed in terms of acceleration.
2. The formulas and the calculations are much simpler and more efficient than in the traditional method. The main reasons for these are the selection of the acceleration update scheme as well as the calculations in the inertial frame.
3. The new algorithm can be applied to any set of gravity data without modeling the gravity disturbance stochastically because the algorithm does not require such a model as long as it dominates the "real" observation error. Under appropriate circumstances, it leads to a much more efficient way of recovering the gravity disturbance vector.

The disadvantage of this new approach is that the standard deviations of the calculated gravity disturbances cannot be obtained directly because of the way they are estimated. Note that the gravity is not modeled explicitly and the residual vector from the Kalman filter is defined to be essentially the estimated gravity disturbance vector.

The effect of each error parameter on the INS acceleration as well as the validity of the algorithm has been investigated through an intensive simulation. It shows that including scale factor errors of gyros and accelerometers as state variables does not improve the results of the gravity estimates. In addition, the most important of the error parameters turned out to be the orientation error which is very difficult to be separated from gravity. By including the effect of all system errors, such as biases, scale factor errors and initial orientation errors, the simulated observations were corrupted up to the standard deviation of ±(17-21 mGal) for the horizontal, and ±2.5

mGal for the down component with respect to the true simulated gravity disturbance data. The results from the Kalman filter showed that the gravity disturbance was recovered with an accuracy of ±(5-8 mGal) for horizontal and better than ±1 mGal for the down component.

Real flight data sets, obtained over the Rocky Mountains, for three overlapping flight trajectories are processed using the developed new algorithm. The results, however, showed that the residuals from the Kalman filter do not completely separate the orientation error from the gravity. In addition, the residuals also contain the effect of system white noise. Therefore, further data processing consisting of endmatching and a wave correlation filter was applied to the residuals to extract a more refined gravity signal. The final results from all processing showed that an accuracy of ±(6-8 mGal) and ±(3-5 mGal) can be achieved for the horizontal and vertical component, respectively. The resolution corresponding to the 60-second smoothing is about 3.5 km although the final results (Figure 5.20-22) do not show a resolution better than 10 km for this area. For the down component, these results are comparable to the previous studies in this area (Wei and Schwarz, 1998). Furthermore, this is the first successful attempt to extract the horizontal gravity field using GPS/INS to the author's best knowledge.

There are several lessons learned through this study. First, aircraft angular (rotational) dynamics greatly influence horizontal gravity component estimation as seen in the north component of the INS acceleration. Second, endpoint data are important to eliminate residual trends and biases. Third, multiple traverses over the same gravity signal help to eliminate some of the system errors. Specifically, waveform correlation can be used to eliminate direction dependent errors when applied to lines with opposite flight directions.

An iteration scheme was tested to obtain better estimates of the system errors with the Kalman filter, as well as to assess the standard deviations of the estimates of the gravity disturbances. This procedure failed because the system was updated by wrong estimates of gravitation. In other words, the residuals from the Kalman filter contain the effect of the gravitational acceleration as well as uncompensated system errors. These uncompensated system errors are imposed on the system during the update and consequently, no improvement in the estimates of the INS system errors is shown.

There could be good arguments against the total observation error approach adopted in this study. By omitting the gravity terms in the parametric model, the mathematical model for the adjustment is unbalanced. Furthermore, the residual vector out of the Kalman filter is further processed by WCF to extract better gravity signals. In this case, a general theory of the adjustment is not followed. In other words, we are adjusting the gravity disturbances using the residuals from the first adjustment. Generally, the result is not same as for the estimates from a one-step adjustment in which all the parameters are modeled.

For theoretical satisfaction, therefore, two gravity models, a Gauss-Markov stochastic process and a deterministic trigonometric expansion are included in the

model and tested. In both cases, the estimates of the gravity disturbance were not better than the processed residuals of the non-model approach with respect to the control data. This reaffirms the difficulty in constructing a reasonable mathematical model for the gravity disturbance. The approach with the trigonometric expansion showed less dependency on the a-priori information, of the model and better estimates are expected if higher-order terms could be included based on carefully selecting the frequency band. The corresponding calculations, however, are extremely extensive may require a better numerical algorithm or computing system to make the approach feasible.

A couple of ideas could be tested and implemented in future studies. First, the combination of airborne vector gravity data with a global gravity model could be investigated in order to improve the global model at high frequencies. Second, since the most difficult part in airborne vector gravimetry is the separation of the orientation error from the gravity signal, the integration of other extend systems providing more precise orientation information could be tested. For example, Dwaik (1998) showed the orientation information from the photogrammetry helps to estimate the vector gravity in the GPS/INS airborne gravimetry. Third, an intensive study of the iteration procedure would be necessary. One can try to update the observations using the final results out of WCF. In this case, a theoretical justification should be developed more fully. Fourth, the dynamics of the airplane could be investigated with specific deterministic models in the system equations rather than through stochastic system states of the filter. In this way, the dynamics model may be more rigorous and lead to better results. Fifth, the approach of the trigonometric functions model could be investigated in more detail to improve the numerical efficiency. Finally, a recent study on wave estimator in GPS/GLONASS-INS positioning showed that the wave estimator performs better than the Kalman filter when the input disturbances are of low frequency (Ray *et al.*). Since the characteristics of the orientation error appear in the low frequency, this method could be implemented in extracting the gravity signal in the GPS/INS airborne vector gravimetry.

APPENDIX A

INTEGRATION OF IMU DATA

To obtain the positions as well as velocities from the IMU raw data, the data should be integrated through the navigation equation. Basically, this can be done using a numerical integration algorithm. Here, an algorithm using 3rd order Runge-Kutta integration via quaternion approach is presented.

1. Consider the raw data from IMU, that is the accelerometer and gyro pulses as:
$$\delta \underline{v}_l ,\ \delta \underline{\theta}_l . \tag{A.1}$$
$\delta \underline{v}_l$ is a vector of increments in velocity generated by the three accelerometers and $\delta \underline{\theta}_l$ is a vector of increments in angle generated by the three gyros:
$$\delta \underline{v}_l = \int \underline{a}^b(t)dt ,\ \delta \underline{\theta}_l = \int \underline{\omega}_{ib}^b(t)dt , \tag{A.2}$$
where $\underline{a}^b$ is acceleration in b-frame, $\underline{\omega}_{ib}^b$ is angular vector in b-frame.
2. In order to integrate the navigation equation (n-frame), the transformation matrix C_b^n must be determined and this can be done using the angular vector $\underline{\omega}_{nb}^b$ as explained in chapter 2.
3. Now, consider the basic integration interval $\Delta t = K\delta t$, where K is even integer, and δt is the IMU pulse interval, e.g. $\delta t = \frac{1}{250}s$ for 250 Hz pulse rate. Also, e.g. K=2, 4 or 8 etc., so that $\Delta t = \frac{1}{128}s$ or $\frac{1}{64}s$ or $\frac{1}{32}s$ etc.
The indexes of the time epochs are defined as $t_k = k\Delta t$.
4. Note that the angular vector $\underline{\omega}_{nb}^b = \underline{\omega}_{ib}^b - C_n^b \underline{\omega}_{in}^n$,
where $\underline{\omega}_{in}^n = \begin{pmatrix} (\dot{\lambda} + \omega_e)\cos\varphi \\ -\dot{\varphi} \\ -(\dot{\lambda} + \omega_e)\sin\varphi \end{pmatrix}$ has components generally smaller in magnitude than $\underline{\omega}_{ib}^b$ for a strapdown system. Assume that a good approximation to $\int C_n^b \underline{\omega}_{in}^n(t)dt$ is given by the assumption that $C_n^b \underline{\omega}_{in}^n$ is constant over the integration interval. Then let

$$\Delta\underline{\theta}(t_k) = \int_{t_{k-1}}^{t_k} \left(\underline{\omega}_{ib}^b - C_n^b \underline{\omega}_{in}^n\right) dt \approx \sum_{j=0}^{K-1} \delta\underline{\theta}_{Kk+j} - C_n^b(t_{k-1})\underline{\omega}_{in}^n(t_{k-1})\Delta t\,. \tag{A.3}$$

5. In order to use a 3rd-order Runge-Kutta numerical integration algorithm, the basic integration interval must be derived into two parts. Therefore, define

$$\Delta\underline{\theta}_1(t_k) = \sum_{j=0}^{K/2-1} \delta\underline{\theta}_{Kk+j} - C_n^b(t_{k-1})\underline{\omega}_{in}^n(t_{k-1})\frac{\Delta t}{2} \tag{A.4}$$

$$\Delta\underline{\theta}_2(t_k) = \sum_{j=K/2}^{K-1} \delta\underline{\theta}_{Kk+j} - C_n^b(t_{k-1})\underline{\omega}_{in}^n(t_{k-1})\frac{\Delta t}{2} \tag{A.5}$$

6. The numerical integration is done using quaternion, $\underline{q} = \begin{pmatrix} a \\ b \\ c \\ d \end{pmatrix}$. The transformation from body to navigation frame using quaternion is given by (2.36).

$$C_b^n = \begin{pmatrix} a^2+b^2-c^2-d^2 & 2(bc+ad) & 2(bd-ac) \\ 2(bc-ad) & a^2+c^2-b^2-d^2 & 2(cd+ab) \\ 2(bd+ac) & 2(cd-ab) & a^2+d^2-c^2-b^2 \end{pmatrix}, \tag{A.6}$$

where $\underline{q}$ satisfies the differential equation:

$$\dot{\underline{q}} = \frac{1}{2}A\underline{q} \tag{A.7}$$

with

$$A = \begin{pmatrix} 0 & \omega_1 & \omega_2 & \omega_3 \\ -\omega_1 & 0 & \omega_3 & -\omega_2 \\ -\omega_2 & -\omega_3 & 0 & \omega_1 \\ -\omega_3 & \omega_2 & -\omega_1 & 0 \end{pmatrix} \quad \text{and} \quad \underline{\omega}_{nb}^b = \begin{pmatrix} \omega_1 \\ \omega_2 \\ \omega_3 \end{pmatrix}. \tag{A.8}$$

7. The integration algorithm is given by

$$\underline{q}(t_k) = \left[\left(1 - \frac{7}{24}\left[\Delta\underline{\theta}(t_k)\right]^2\right)I + \left(\frac{1}{2} - \frac{1}{16}\left[\Delta\underline{\theta}(t_k)\right]^2\right)A_\theta \right.$$
$$\left. -\frac{1}{2}A_{\theta_1}A_{\theta_2} - \frac{1}{6}A_{\theta_2}A_{\theta_1} - \frac{1}{3}\left[\Delta\underline{\theta}_1(t_k)\right]^2 A_{\theta_2} - \frac{1}{3}\left[\Delta\underline{\theta}_2(t_k)\right]^2 A_{\theta_1}\right]\underline{q}(t_{k-1})\,, \tag{A.9}$$

$k = 1,2,\ldots$

where $\left[\Delta\underline{\theta}(t_k)\right]^2$ means $\left[\Delta\underline{\theta}(t_k)\right]^T \cdot \Delta\underline{\theta}(t_k)$ (sum of squares of elements),

$$A_\theta = \begin{pmatrix} 0 & \Delta\theta_1 & \Delta\theta_2 & \Delta\theta_3 \\ -\Delta\theta_1 & 0 & \Delta\theta_3 & -\Delta\theta_2 \\ -\Delta\theta_2 & -\Delta\theta_3 & 0 & \Delta\theta_1 \\ -\Delta\theta_3 & \Delta\theta_2 & -\Delta\theta_1 & 0 \end{pmatrix} \quad , \quad \Delta\underline{\theta}(t_k) = \begin{pmatrix} \Delta\theta_1 \\ \Delta\theta_2 \\ \Delta\theta_3 \end{pmatrix}, \tag{A.10}$$

$$A_{\theta_1} = \begin{pmatrix} 0 & \Delta\theta_{11} & \Delta\theta_{21} & \Delta\theta_{31} \\ -\Delta\theta_{11} & 0 & \Delta\theta_{31} & -\Delta\theta_{21} \\ -\Delta\theta_{21} & -\Delta\theta_{31} & 0 & \Delta\theta_{11} \\ -\Delta\theta_{31} & \Delta\theta_{21} & -\Delta\theta_{11} & 0 \end{pmatrix} \quad , \quad \Delta\underline{\theta}_1(t_k) = \begin{pmatrix} \Delta\theta_{11} \\ \Delta\theta_{21} \\ \Delta\theta_{31} \end{pmatrix}, \tag{A.11}$$

$$A_{\theta_2} = \begin{pmatrix} 0 & \Delta\theta_{12} & \Delta\theta_{22} & \Delta\theta_{32} \\ -\Delta\theta_{12} & 0 & \Delta\theta_{32} & -\Delta\theta_{22} \\ -\Delta\theta_{22} & -\Delta\theta_{32} & 0 & \Delta\theta_{12} \\ -\Delta\theta_{32} & \Delta\theta_{22} & -\Delta\theta_{12} & 0 \end{pmatrix} \quad , \quad \Delta\underline{\theta}_2(t_k) = \begin{pmatrix} \Delta\theta_{12} \\ \Delta\theta_{22} \\ \Delta\theta_{32} \end{pmatrix}. \tag{A.12}$$

Note that the initial quaternion may be obtained from the inverse relation between the transformation and the quaternion.

$$a = \frac{1}{2}\left[1 + (C_b^n)_{11} + (C_b^n)_{22} + (C_b^n)_{33}\right]^{1/2} \tag{A.13}$$

$$b = \frac{1}{4a}\left[(C_b^n)_{23} - (C_b^n)_{32}\right] \tag{A.14}$$

$$c = \frac{1}{4a}\left[(C_b^n)_{31} - (C_b^n)_{13}\right] \tag{A.15}$$

$$d = \frac{1}{4a}\left[(C_b^n)_{12} - (C_b^n)_{21}\right] \tag{A.16}$$

It should be noted that the reorthogonalization is necessary at each step by replacing $\underline{q}$ by $\frac{1}{\sqrt{\underline{q}^T\underline{q}}}\underline{q}$.

8. The accelerations from the accelerometers are integrated based on 3-point Simpson's rule, which is accurate to third order in Δt.

$$\Delta\underline{v}(t_k) = \int_{t_{k-2}}^{t_k} C_b^n(t)\underline{a}^b(t)dt \tag{A.17}$$

Note that the integration interval spans two basic intervals of length Δt. The algorithm accurate to third order is given by:

$$\begin{aligned} \Delta\underline{v}(t_k) = \frac{1}{6}\Big[& C_b^n(t_{k-2})\left(3\Delta\underline{v}^b(t_{k-1}) - \Delta\underline{v}^b(t_k)\right) \\ & + 4C_b^n(t_{k-1})\left(\Delta\underline{v}^b(t_{k-1}) + \Delta\underline{v}^b(t_k)\right) \\ & + C_b^n(t_k)\left(3\Delta\underline{v}^b(t_k) - \Delta\underline{v}^b(t_{k-1})\right)\Big] \end{aligned} \quad , \tag{A.18}$$

where $\Delta\underline{v}^b(t_k) = \sum_{j=0}^{K-1} \delta\underline{v}_{Kk+j}$, $\Delta\underline{v}^b(t_{k-1}) = \sum_{j=0}^{K-1} \delta\underline{v}_{K(k-1)+j}$.

9. Now, recall the Navigation (3.4.4) equations written as:

$$\begin{aligned} \dot{v}_N &= a_N + f_N(\underline{v}, h, \varphi) \\ \dot{v}_E &= a_E + f_E(\underline{v}, h, \varphi) \end{aligned} \tag{A.19}$$

This is integrated using a first-order algorithm:

$$v_N(t_{k+2}) = v_N(t_k) + \Delta v_N(t_{k+2}) + f_N(\underline{v}(t_{k+1}), h(t_{k+1}), \varphi(t_{k+1})) \cdot 2\Delta t \tag{A.20}$$

Note that each integration step spans two basic intervals, Δt .

10. To compute $\underline{f}(\underline{v}(t_{k+1}), h(t_{k+1}), \varphi(t_{k+1}))$, the previous values of the integrated navigation equations are needed. So once $\underline{v}(t_{k+2})$ is determined, compute

$$\varphi(t_{k+2}) = \varphi(t_k) + \frac{v_N(t_{k+1})}{M(t_{k+1}) + h(t_{k+1})} \cdot 2\Delta t \tag{A.21}$$

$$N(t_{k+2}) = \frac{a}{\sqrt{1 - e^2 \sin^2 \varphi(t_{k+1})}} \tag{A.22}$$

$$M(t_{k+2}) = \frac{a(1-e^2)}{\left[1 - e^2 \sin^2 \varphi(t_{k+2})\right]^{3/2}} \tag{A.23}$$

$$\lambda(t_{k+2}) = \lambda(t_k) + \frac{v_E(t_{k+1})}{\left(N(t_{k+1}) + h(t_{k+1})\right)\cos\varphi(t_{k+1})} \cdot 2\Delta t \tag{A.24}$$

$$\dot{\varphi}(t_{k+2}) = \frac{v_N(t_{k+2})}{M(t_{k+2}) + h(t_{k+2})} \tag{A.25}$$

$$\dot{\lambda}(t_{k+2}) = \frac{v_E(t_{k+2})}{\left(N(t_{k+2}) + h(t_{k+2})\right)\cos\varphi(t_{k+2})} \tag{A.26}$$

$$\underline{\omega}_{in}^{n}(t_{k+2}) = \begin{pmatrix} (\dot{\lambda}(t_{k+2}) + \omega_e)\cos\varphi(t_{k+2}) \\ -\dot{\varphi}(t_{k+2}) \\ -(\dot{\lambda}(t_{k+2}) + \omega_e)\sin\varphi(t_{k+2}) \end{pmatrix} \tag{A.27}$$

11. The total algorithm is shown at Figure A.1.

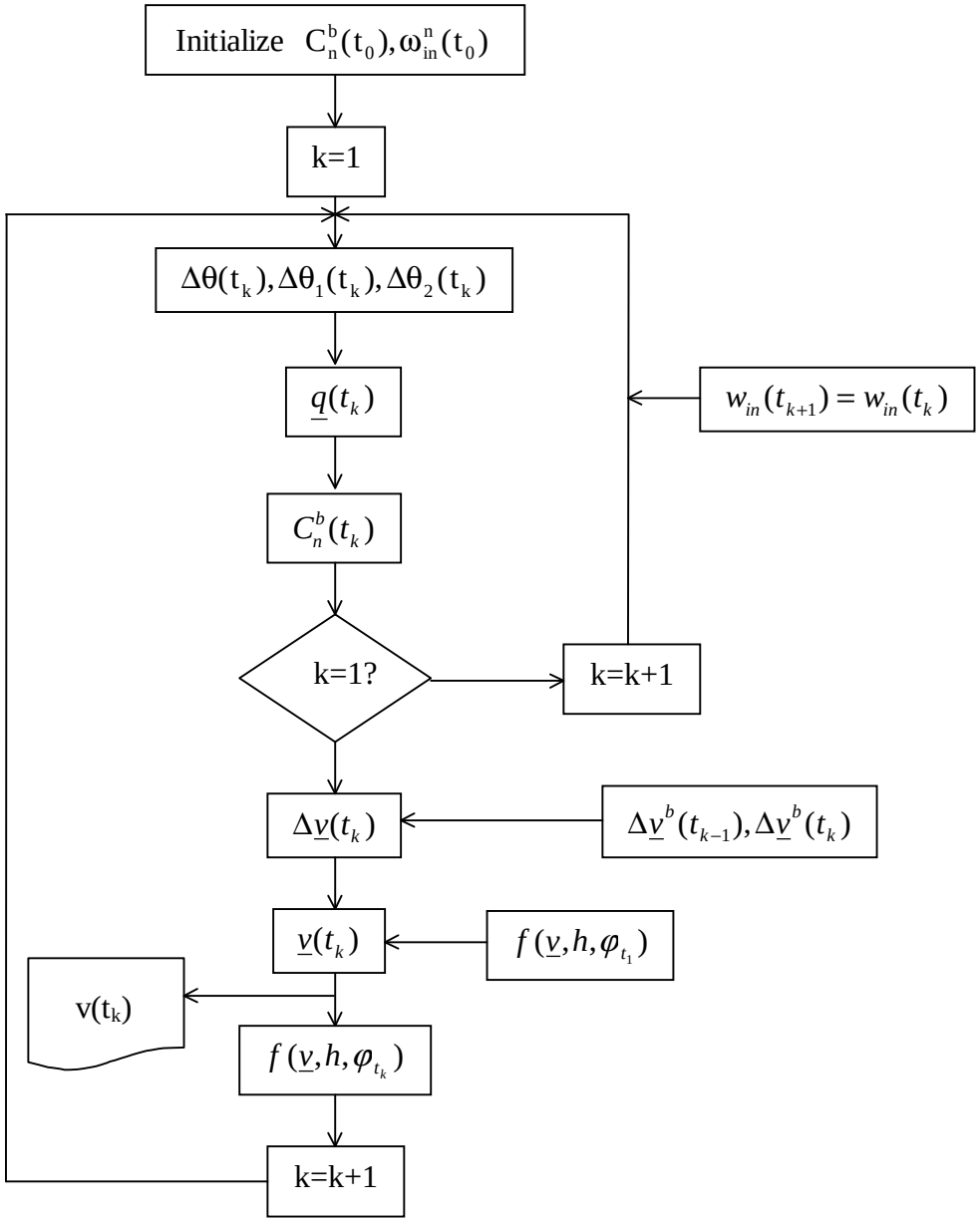

Figure A.1 Flow chart for IMU data integration.

BIBLIOGRAPHY

Arfken, G., (1985): *Mathematical Methods for Physicists* (3rd edition), Academic Press, Inc., Orlando, Florida.

Arshal, G., (1987): Error Equations of Inertial Navigation, *J. Guidance, Navigation and Dynamics*, Vol. 10, No. 4, pp. 351-358.

Boedecker, G., Neumayer, H., (1995): An Efficient Way to Airborne Gravimetry: Integration of Strapdown Accelerometer and GPS-System Performance in Selected Frequency Bands in a Dynamic Environment, Proc. IAG Symposium on Airborne Gravity Field Determination, IUGG XXI General Assembly, Boulder, Colorado, July 2-14, pp. 23-28.

Brown, R.G., Hwang, P.Y.C., (1997): *Introduction to Random Signals and Applied Kalman Fitering* (3rd edition), John Wiley, New York, etc.

Broxmeyer, C., (1964): *Inertial Navigation Systems*, McGraw-Hill, New York San Francisco Toronto London.

Brozena, J.M., (1991): GPS and Airborne Gravimetry: Recent Progress and Future Plans, *Bulletin Géodésique*, Vol. 65, pp. 116-121.

Brozena, J.M., Mader, G.L., Peters, M.F., (1989): Interferometric Global Positioning System: Three-Dimensional Positioning Source for Airborne Gravimetry, *Journal of Geophysical Research*, Vol. 94, No. B9, pp.12153-12162.

Brozena, J.M., Peters, M.F., (1988): An Airborne Gravity Study of Eastern North Carolina, *Geophysics*, Vol. 53, No. 2, pp. 245-253.

Brozena, J.M., Peters, M.F., (1994): Airborne Gravity Measurement at NRL, Proc. of the Intern. Symp. on Kinematic Systems in Geodesy, Geomatics and Navigation, Banff, Canada, Aug. 30-Sept. 2, The University of Calgary, pp. 495-506.

Brozena, J.M., Peters, M.F., (1995): Methods to Improve Existing Shipboard Gravimeters for Airborne Gravimetry, IAG Symposium on Airborne Gravity

Field Determination, IUGG XXI General Assembly Boulder, Colorado, USA, July 2-14, pp. 39-45.

Cannon, M.E., (1991): Airborne GPS/INS with an Application to Aeriotriangulation, UCSE Reports, No. 20040, Dept. of Geomatics Engineering, The University of Calgary, Alberta, Canada.

Cheney, W., Kincaid, D., (1996): *Numerical Mathematics and Computing*, Brooks/Cole Publishing Company, Pacific Grove, California.

Coco, R., (1991): GPS-satellite of Opportunity for Ionospheric Monitoring, *GPS World*, Vol. 2, No.9, pp. 47-50.

Da, R., (1997): Investigation of a Low-Cost and High-Accuracy GPS/IMU System, ION National Technical Meeting, Santa Monica, CA, Jan. 14-16, pp. 1-5.

de Boor, C., (1978): *A Practical Guide to Splines*, Springer-Verlag, New York.

Dwaik, F.Y., (1998): INS,GPS, and photogrametry integration for vector gravimetry estimation, Doctoral Dissertation, Geodetic Science and Surveying Program, The Ohio State University

Eissfeller, B., Spietz, P., (1989): Shaping Filter Design for the Anomalous Gravity Field by Means of Spectral Factorization, *manuscripta geodaetica*, Vol.14, pp. 183-192.

Forsberg, R., (1987): A New Covariance Model, for Inertial Gravimetry and Gradiometry, *J. Geophy. Res.*, Vol. 92, No. B2, pp. 1305-1310.

Forsberg, R., Kenyon, S., (1994): Evaluation and Downward Continuation of Airborne Gravity Data – the Greenland Example, Proc. Int. Symp. Kinematic Systems in Geodesy, Geomatics, and Navigation, Banff, Canada, Aug. 30-Sept. 2, The University of Calgary, pp. 531-538.

Gelb, A., (1994): *Applied Optimal Estimation*, The M.I.T. Press, Cambridge Massachusetts, London.

Glennie, C., Schwarz, K.P., (1999): A Comparison and Analysis of Airborne Gravimetry Results from Two Strapdown Inertial/DGPS Systems, *Journal of Geodesy*, Vol. 73, pp. 311-321.

Glennie, C., Schwarz, K.P., Bruton, A.M., (1999): A Comparison of Stable Platform and Strapdown Airborne Gravity, *Journal of Geodesy*, summitted.

Goad, C.C., Goodman, L., (1974): A Modified Hopfield Tropospheric Refraction Correction Model. Presented at the Fall Meeting of the American Geophysical Union, San Francisco, December, 1974.

Goad, C.C., Yang, M., (1995): A New Approach to Precision Airborn GPS Positioning for Photogrammetry. *Photogrammetric Engineering and Remote Sensing*, Vol. 63, No. 9, pp. 1067-1077.

Goshen-Meskin, D., Bar-Itzhack, I.Y., (1992): Unified Approach to Inertial Navigation System Error Modeling, AIAA *J. of Guidance, Control and Dynamics*, Vol. 15, No. 3, pp. 648-653.

Grejner-Brzezinska, D.A., (1995): Analysis of GPS Data Processing Techniques: In Search of Optimized Strategy of Orbit and Earth Rotation Parameter Recovery, Report No. 432, Dept. of Geodetic Science and Surveying, The Ohio State University, Columbus, Ohio, USA.

Grejner-Brzezinska, D.A., Wang, J., (1999): Gravity Modeling for High-Accuracy GPS/INS Integration, *Journal of Geodesy*, submitted.

Hammada, Y., (1996): A Comparison of Filtering Techniques for Airborne Gravimetry, UCGE Reports, No. 20089, Dept. of Geomatics Engineering, The University of Calgary, Alberta, Canada.

Han, S., Rizos, C., (1996): Improving the Computational Efficiency of the Ambiguity Function Algorithm, Journal of Geodesy, Vol. 70, No. 6, pp. 330-341.

Hehl, K., (1994): Fundamentals and Applications of Digital Filtering in Airborne Gravimetry, International Association of Geodesy Symposia No. 113, Springer-Verlag, Berlin, New York, pp. 161-170.

Hein, G.W., (1995): Progress in Airborne Gravimetry: Solved, Open and Critical Problems, Proc. of the IAG Symposium on Airborne Gravity Field Determination, IUGG XXI General Assembly Boulder, Colorado, USA, July 2-14, pp. 3-11.

Hieskanen, W.A., Moritz, H., (1987): *Physical Geodesy*, reprint, Institute of Physical Geodesy, Technical University, Graz, Austria.

Heller, W.G., Jordan, S.K., (1976): Error Analysis of Two New Gradiometer-aided

Inertial Navigation Systems, *J. Spacecraft*, Vol. 13, No. 6, pp. 340-347.

Heroux, P., Kouba, J., (1995): GPS Precise Point Positioning with a Difference, Presented at Geomatics '95, Ottawa, Ontario, Canada, June 13-15.

Hofmann-Wellenhof, B., Lichtenegger, H., Collins, J., (1997): *GPS Theory and Practice* (3rd edition), Springer, New York.

Honeywell, (1991): *H-423 System Description*, Military Avionics Division, Honeywell, Florida, USA.

Huddle, J.R., (1977): The Theoretical Principles for Design of the Inertial Surveyor for Position and Gravity Determinations, Proc. of the 1st Int. Symp. on Inertial Technology for Surveying and Geodesy, Ottawa, 1977, pp. 45-59.

Huddle, J.R., (1988): The Rapid Geodetic Survey System (RGS), Proc. Chapman Conference on Progress in the Determination of the Earth's Gravity Field, (IN): Report No. 397, Dept. of Geodetic Science and Surveying, The Ohio State University, Columbus Ohio, USA.

Hwang, P.Y.C., (1991): Kinematic GPS for Differential Positioning: Resolving Integer Ambiguities on the Fly, *Navigation: Journal of the Institute of Navigation*, Vol. 38, No. 1, pp.205-219.

Jekeli, C., (1992): Vector Gravimetry Using GPS in Free-fall And in an Earth-fixed Frame, *Bulletin Géodésique*, Vol. 66, pp. 54-61.

Jekeli, C., (1995): Airborne Vector Gravimetry Using Precise, Position-Aided Inertial Measurement Units, *Bulletin Géodésique*, Vol. 69, pp. 1-11.

Jekeli, C., (1995a): *Inertial Geodesy*, Lecture Notes, The Ohio State University.

Jekeli, C., (1995b): GPS/INS Positioning And the Earth's Gravitational Field, Proc. 1995 Mobile Mapping Symp., American Society for Photogrammetry and Remote Sensing, Bethesda, Maryland, pp. 163-172.

Jekeli, C., (1999): An analysis of vertical deflections derived from high-degree spherical harmonic models, *Journal of Geodesy*, Vol. 73, No. 1, pp. 10-22.

Jekeli, C., Kwon, J.H., (1999): Results of Airborne Vector (3-D) Gravimetry, *Geophysical Research Letters*, Vol. 26, No. 23, pp. 3533-3536.

Jordan, S.K., (1972): Self-consistent Statistical Models for the Gravity Anomaly,

Vertical Deflections, and Undulation of the Geoid, *J. Geophy. Res.*, Vol. 77, No. 20, pp. 3660-3670.

Kim, J., (1995): Improved Recovery of Gravity Anomalies from Dense Altimeter Data, Doctoral Dissertation, Dept. of Geodetic Science and Surveying, The Ohio State University, Columbus Ohio, USA.

Kincaid, D., Cheney, W., (1996): *Numerical Analysis*, Brooks/Cole Publishing Company, Pacific Grove, etc.

Knickmeyer, E.T., (1990): Vector Gravimetry by Combination of Inertial and GPS Satellite measurements, Report No. 20035, Department of Surveying Engineering, The University of Calgary, Alberta, Canada.

Kwon, J.H., Jekeli, C., Han, S., (1999): Absolute Kinematic GPS Positioning Using Satellite Clock Estimation Every 1 Second, Presented at IUGG General Ass., Birmingham UK.

LaCoste, L., Ford, J., Bowles, R., Archer, K., (1982): Gravity Measurements in an Airplane Using State-of-the Art Navigation and Altimetry, *Geophysics*, Vol. 47, No. 5, pp. 832-838.

Leick, A., (1995): *GPS Satellite Surveying*, Wiley-Interscience, New York, etc.

Lemoine, F.G., Kenyon, S.C., Factor, J.K., Trimmer, R.G., Palvis, N.K., Chinn, D.S., Cox, C.M., Klosko, S.M., Luthcke, S.B., Torrence, M.H., Wang, Y.M., Williamson, R.G., Palvis, E.C., Rapp, R.H., Olson, T.R., (1998): *The Development of the Joint NASA GSFC and the National Imagery and Mapping Agency (NIMA) Geopotential Model EGM96*, NASA/TP, 1998-206861, Goddard Space Flight Center, Greenbelt, Maryland.

Marion, B.J., Thornton, S., (1995): *Classical dynamics of particles and systems*, Saunders College Publishing, San Diego, New York.

McCarthy, D.D., (1996): IERS Conventions, IERS Technical note 21, Central Bureau of IERS – Observatoire de Paris, Paris France.

Moritz, H., (1969): Kinematical Geodesy, Report No. 92, Dept. of Geodetic Science, The Ohio State University, Columbus Ohio, USA.

Moritz, H., (1980): *Advanced Physical Geodesy*, Abacus Press, Tunbridge Wells, Kent, UK.

Moritz, H., (1992): Geodetic Reference System 1980, *Bulletin Géodésique*, Vol. 66, No. 2, pp. 187-197.

Moritz, H., Mueller, I., (1988): *Earth rotation – Theory and Observation*, The Ungar Publishing Company, Ungar/New York.

Nash, R.A., (1968): Effect of Vertical Deflections and Ocean Currents on a Maneuvering Ship, *IEEE Trans. Aerospace and Electronic Systems*, Vol. 4, No. 5, pp. 719-727.

Rapp, R., (1994): *Geometric Geodesy*, Lecture Note, Dept. of Geodetic Science and Surveying, The Ohio State University, Columbus Ohio, USA.

Rapp, R.H., Pavlis, N.K., (1990): The Development and Analysis of Geopotential Coefficient Models to Spherical Harmonic Degree 360, *J. Geophys. Res*. Vol. B95, pp. 21885-21911.

Ray, J.K., Salychev, O.S., Cannon, M.E., (1999): The Modified Wave Estimator as an Alternative to a Kalman Filter for Real-time GPS/GLONASS-INS Integration, *Journal of Geodesy*, Vol. 73, No. 10, pp. 568-576.

Reigber, C., King, Z., Konig, R., Schwintzer, P., (1997): CHAMP, a minisatellite mission for geopotential and atmospheric research, Spring AGU Meeting, Baltimore, MD.

Remondi, B.W., (1991): Kinematic GPS Results without Static Initialization, National Information Center, Rockville, Maryland, NOAA Technical Memorandum NOS NGS-55.

Rose, R.C., Nash, R.A., (1972): Direct Recovery of Deflection of the Vertical Using an Inertial Navigator, *IEEE Trans. Geoscience Electronics* Vol. 10, No. 2, pp. 85-92.

Rummel, R., (1999). Gravity Field and Steady-State Ocean Circulation Mission, Earth Explorer Mission Selection Workshop, ESA, Granada, Spain, October 12-15, 1999.

Salychev, O.S., Bykovsky, A.V., Voronov, V.V., Schwarz, K.P., Liu, Z., Wei, M., Panenka, J., (1994): Determination of Gravity and Deflections of the Vertical for Geophysical Applications Using the ITC-2 Platform, Proc. of Intern. Symp. on Kinematic Sys. in Geodesy, Geomatics and Navigation, Banff, Canada Aug. 30–Sept. 2, The University of Calgary, pp. 521-529.

Schaffrin, B., Grafarend, E., (1986): Generating Classes of Equivalent Linear Models by Nuisance Parameter Elimination, *Manuscripta Geodaetica*, Vol. 11, pp. 262-271.

Schwarz, K.P., (1987): Approaches to Kinematic Geodesy, In: Geodetic Theory and Methodology, Publ. No. 60006, Dept. of Surveying Eng., University of Calgary, Alberta Canada.

Schwarz, K.P., Li, Y., Wei, M., (1994): The Spectral Window for Airborne Gravity and Geoid Determination. Proc. of Intern. Symp. on the Kinematic Systems in Geodesy, Geomatics and Navigation, Banff, Canada, Aug. 30-Sept. 2, The University of Calgary, pp. 445-456.

Seeber, G., (1993): *Satellite Geodesy*, Walter de Gruyter, Berlin New York.

Tapley, B., Reigber, C., Melbourne, W., (1997): Gravity Recovery And Climate Experiment (GRACE) mission, Spring AGU Meeting, Baltimore.

Torge, W., (1989): *Gravimetry*, Walter deGruyter, Berlin.

VonFrese, R.B., Jones, M.B., Kim, J.W., Kim, J.H., (1997): Analysis of Anomaly Correlations, *Geophysics*, Vol. 62, No. 1, pp. 342-351.

Wang, J., (1997): Gravity Recovery by LN-93 Strapdown Airborne Gravity System – A Comparison of Different Vector Gravimetry Approaches Based on Simulations, Report No. 439, Dept. of Geodetic Science and Surveying, The ohio state university, Columbus Ohio, USA.

Wang, J., Jekeli, C., (1998): Stochastic Model Versus Deterministic Model in INS/GPS Positioning, ISPRS, Commission III Symposium, Columbus Ohio, USA.

Wang, J., Gao, Z., (1996): Real Time Estimation of Position and the Gravity Vector with an Inertial Survey System, *Journal of Geodesy*, Vol. 71, pp. 16-20.

Wei, M., Schwarz, K.P., (1994): An Error Analysis of Airborne Vector Gravimetry, Proc. Of the International Symposium on Kinematic Systems in Geodesy, Geomatics and Navigation, Banff, Canada, Aug. 30-Sept. 2, The University of Calgary, pp. 509-520.

Wei, M., Schwarz, K.P., (1995): Analysis of GPS-Derived Acceleration from Airborne Tests. Proc. of the IAG Symp. on Airborne Gravity Field Determination, IUGG XXI General Assembly, Boulder Colorado, USA, July 2-14, pp. 175-188.

Wei, M., Schwarz, K.P., (1998): Flight Test Results from a Strapdown Airborne Gravity System, *Journal of Geodesy*, Vol. 72, No. 6, pp. 323-332.

Yang, M., (1995): New GPS Measurement Modeling Techniques of Orbit Determination and Precise Kinematic Positioning, Report No. 431, Dept. of Geodetic Science and Surveying, The Ohio State University, Columbus Ohio, USA.